

UNIVERSITÀ DEGLI STUDI DI PADOVA

Dipartimento di Fisica e Astronomia “Galileo Galilei”

Master Degree in Physics

Final Dissertation

Laser-Based Resolution Studies for Improved Track Reconstruction in a Time Projection Chamber

Thesis supervisor

Gianmaria Collazuol

Thesis co-supervisor

Stefano Levorato

Candidate

Davide Marchesini

Academic Year 2024/2025

Contents

| | |
|--|-----------|
| Abstract | 3 |
| 1 Introduction to neutrino oscillation | 4 |
| 1.1 Neutrino oscillation | 4 |
| 1.2 The neutrino mass problem | 8 |
| 1.3 State of the art | 9 |
| 2 The T2K experiment | 11 |
| 2.1 J-PARC | 11 |
| 2.2 ND280 | 13 |
| 2.3 Super-Kamiokande | 16 |
| 3 The HATPC and the experimental setup | 19 |
| 3.1 Structure of the HATPC | 20 |
| 3.2 Structure of the mTPC | 21 |
| 3.3 The ERAM readout | 24 |
| 4 Laser setup | 28 |
| 4.1 Laser description | 28 |
| 4.2 Double photon ionization | 31 |
| 4.3 Experimental setup and laser tests | 31 |
| 4.4 Laser simulation | 33 |
| 4.5 Gas absorption length and divergence | 36 |
| 4.6 α source activity | 38 |
| 4.7 Waveform analysis | 38 |
| 4.8 Preliminary analysis and configuration tests | 39 |
| 4.9 Drift velocity parameterization | 41 |
| 4.10 Final configuration and data taking | 41 |
| 5 Laser studies | 47 |
| 5.1 Laser tracks and mirror reflections | 47 |
| 5.2 Drift velocity measurements for horizontal and vertical scan | 48 |
| 5.3 Drift velocity near the mirror | 49 |
| 5.4 Effects of added resistance | 51 |
| 5.5 Laser pointing to the ERAM | 52 |
| 6 A New Track Reconstruction Algorithm | 57 |
| 6.1 Pad Response and Gaussian Diffusion Model | 57 |
| 6.2 LogQ method | 58 |
| 6.3 Waveform Fit Based on the Gaussian Diffusion Model | 61 |

| | | |
|----------|--|-----------|
| 6.4 | Multiple pad fit | 63 |
| 6.5 | Empirical Waveform Fit and Feature extraction | 63 |
| 6.6 | Extraction of Signal Areas | 68 |
| 6.7 | Incorporating the effect of ions | 71 |
| 6.8 | Parameter Distributions and Relative Errors | 71 |
| 6.9 | Pad simulation | 73 |
| 6.10 | Reconstruction Algorithm | 75 |
| 6.11 | Example of fit | 77 |
| 6.12 | Final considerations about this part of my work | 79 |
| 7 | Scintillation light by the T2K gas mixture | 81 |
| 7.1 | CF_4 scintillation | 81 |
| 7.2 | Experimental setup | 82 |
| 7.3 | Analysis of the Quartz Window Data Set | 84 |
| 7.4 | α tracking | 85 |
| 7.5 | Monte Carlo Simulation of Muon Tracks and Photon Detection | 87 |
| 7.6 | PMT Installation into the Active Volume | 89 |
| 7.7 | Analysis of Data with the PMT facing the Active Volume | 91 |
| | Conclusions | 93 |
| | Bibliography | 94 |

Abstract

Two large gaseous Time Projection Chambers (TPCs) were assembled at CERN (Geneva, Switzerland) and installed at the J-PARC laboratory (Tokai, Japan). These detectors were developed for the T2K Near Detector (ND280) Upgrade project, featuring a state-of-the-art design with lightweight composite materials. Each TPC has a precise geometry with a 1.7×0.8 m² instrumented anode surface, a $1m + 1m$ drift length, and a central cathode. They operate with a fast-drift "T2K" gas mixture ($Ar : CF_4 : isoC_4H_{10} = 95 : 3 : 2$), while maintaining minimal contamination. A sophisticated electrode structure ensures a uniform electric field, guiding ionization electrons toward the anode, where their position and charge are measured using Resistive MicroMegas sensor modules (ERAM). From Winter 2023 to Spring 2024, the installation of both TPCs was completed, their volumes were purged, and commissioning was performed using cosmic rays at J-PARC, with and without a magnetic field. The first neutrino beam data were collected in June 2024 for physics studies. A third full-scale TPC was produced and is currently operated at CERN, where it will be exposed to low-energy electron and hadron test beams at the CERN PS facility, along with intense pulsed UV laser beams, to evaluate its performance in track measurement and particle identification.

This thesis presents the following research activities:

- Studies performed at LNL utilized a small-scale TPC prototype with an intense pulsed UV laser beam to investigate track formation, detection, and measurement. These studies achieved a high-precision assessment of spatial resolution and energy loss resolution, developing a strategy for future laser calibration campaigns with the full-scale FC0 detector (Chapters 4 and 5).
- Development of an improved tracking algorithm that connects physical track parameters to signal formation. Leveraging laser tracks with reduced systematic uncertainties, this new method enhances the current HATPC tracking reconstruction (Chapter 6).
- Investigation of scintillation light production in the T2K gas mixture. Although not observed at the beginning of this activity, such light could provide a direct trigger for primary scintillation. The analysis used data from the prototype TPC with a coincident PMT signal; however, no visible scintillation light was detected from cosmic muons (Chapter 7).

Chapter 1

Introduction to neutrino oscillation

The main physics goals for the creation of the T2K collaboration in 1999 were:

- The search for CP violation in the neutrino sector.
- The discovery of oscillation from ν_μ to ν_e .
- Precise measurements of the oscillation parameters in ν_μ disappearance.
- The search for sterile components in ν_μ disappearance by observing neutral-current events.
- To produce the world-leading cross-section measurements for the neutrino-nucleus interaction.

To understand the physics behind this, I will concentrate on the explanation of the main aspects, which are the determination of the oscillation parameters and the phase that gives rise to CP violation in the neutrino sector [16].

1.1 Neutrino oscillation

The neutrinos are 3 types of particles in the modern Standard Model. Each neutrino corresponds to a flavour: electron, muon, tau. Similarly to the CKM matrix of the quarks, historically developed before, it is possible to suppose that the 3 states of flavour do not correspond to the eigenstates of mass, in the supposed case neutrinos have mass. Nowadays it is known that this is the case and it has been experimentally demonstrated indirectly, thanks to the neutrino oscillation (and directly by measuring the electron energy spectrum in β decays, as of today there are only constraints regarding the maximum mass for the anti electron neutrino $m_{\bar{\nu}_e} < 0.8 \frac{eV}{c^2}$ at 90% CL [5]).

By starting from the unitary transformation

$$\begin{pmatrix} \nu_e \\ \nu_\mu \\ \nu_\tau \end{pmatrix} = \begin{pmatrix} U_{e1} & U_{e2} & U_{e3} \\ U_{\mu1} & U_{\mu2} & U_{\mu3} \\ U_{\tau1} & U_{\tau2} & U_{\tau3} \end{pmatrix} \cdot \begin{pmatrix} \nu_1 \\ \nu_2 \\ \nu_3 \end{pmatrix}$$

that determines the composition of each flavour on the mass eigenstates (so U is the transformation matrix from the mass eigenstates ν_i to the flavour eigenstate ν_α), we can use the same Wolfstein parametrization similarly to the CKM matrix. The CKM must satisfy the unitarity property and, because it is a 3 x 3 matrix, it must have 3 angles and 1 phase. Consequentially also the PMNS (Pontecorvo-Maki-Nakagawa-Sakata, from the names of the physicist who worked together on this model), which is the matrix U , must satisfy similar conditions, and thus have

4 parameters. During the course of the last two decades multiple collaborations were formed to determine all the 4 parameters necessary to describe the neutrino oscillation phenomena.

Now it is possible to write the PMNS matrix using the angles as

$$\begin{pmatrix} \nu_e \\ \nu_\mu \\ \nu_\tau \end{pmatrix} = \begin{pmatrix} 1 & 0 & 0 \\ 0 & +c_{23} & +s_{23} \\ 0 & -s_{23} & +c_{23} \end{pmatrix} \cdot \begin{pmatrix} +c_{13} & 0 & +s_{13}e^{-i\delta_{CP}} \\ 0 & 1 & 0 \\ -s_{13}e^{+i\delta_{CP}} & 0 & +c_{13} \end{pmatrix} \cdot \begin{pmatrix} +c_{12} & +s_{12} & 0 \\ -s_{12} & +c_{12} & 0 \\ 0 & 0 & 1 \end{pmatrix} \cdot \begin{pmatrix} \nu_1 \\ \nu_2 \\ \nu_3 \end{pmatrix}$$

with c_{ij} and s_{ij} the cosine and sine of the angle θ_{ij} , while δ_{CP} the complex phase. As stated before, the neutrino oscillation demonstrates the massive nature of neutrinos. Mathematically this means that the PMNS matrix is not the matrix identity, so the flavour states and the mass state do not coincide.

Oscillation parameters are measured via flux consideration and so, considering a neutrino state in flavour space as ν_α , the probability that the neutrino is of the same type after a period t is

$$P_{\alpha\beta}(t) = |\langle \nu_\alpha(0) | \nu_\beta(t) \rangle|^2$$

This is called survival probability in the state α . The first model for neutrino oscillation considers only two species, electron and muon. This effect has been discovered before the discovery of the tau neutrino and so it is not considered in the calculations (ν_τ 2000, neutrino oscillation 1998). This model was tested by the Kamiokande collaboration in the now famous electron neutrino disappearance phenomena of atmospheric neutrinos [26]. In this specific case the PMNS can be written only as a function of an angle as

$$U = \begin{pmatrix} \cos \theta & -\sin \theta \\ \sin \theta & \cos \theta \end{pmatrix}$$

thus the evolution over time of the α state is given by

$$|\nu_\alpha(t)\rangle = U_{\alpha 1} e^{-iE_1 t} |\nu_1\rangle + U_{\alpha 2} e^{-iE_2 t} |\nu_2\rangle$$

with the assumption that

$$E_i = \sqrt{p^2 + m_i^2} \approx p + \frac{m_i^2}{2p} \approx E + \frac{m_i^2}{2E}$$

considering that the neutrino mass is present but it is known to be nearly zero, and with $t = 0$, which is considered the creation time of the neutrino from the source. The next step is the calculation of the survival probability, assuming that neutrinos are relativistic particles, so they travel a distance $L = ct$:

$$P_{\alpha\alpha}(L) = |\langle \nu_\alpha(0) | \nu_\alpha(L) \rangle|^2 = 1 - 4|U_{\alpha 1}|^2 |U_{\alpha 2}|^2 \sin^2 \left(\frac{(m_2^2 - m_1^2)L}{4E} \right)$$

And now using the angle θ of the PMNS matrix it is possible to obtain

$$P_{\alpha\alpha}(L) = 1 - \sin^2 2\theta \sin^2 \left(\frac{\Delta m_{12}^2 L}{4E} \right)$$

with $\Delta m_{12}^2 = m_2^2 - m_1^2$. It is now fairly easy to notice that in the limit of massless neutrinos the oscillation phenomena is not present. For a neutrino with energy E the probability of being a ν_α depends on the distance observation-source, so by virtually observing the probability of a neutrino for different positions we could observe this modulation.

It is experimentally relevant to estimate the parentheses term in the sine function. The common order of magnitude is given by

$$\frac{\Delta m^2 L}{4E} \approx 1.27 \times \left(\frac{\Delta m^2}{\text{eV}^2} \right) \left(\frac{L}{\text{km}} \right) \left(\frac{E}{\text{GeV}} \right)$$

Experimentally we want to maximize this value: that is the the reason why there are experiments dedicated to each of the 3 mass parameters.

The experimental method used to determined the mass difference consists in using the difference in fluxes, from one point of reference to another one, neglecting interactions in the path, the flux Φ of neutrinos α follows the equation $\Phi(L) = P_{\alpha\alpha}(L) \cdot \Phi(0)$. The Kamiokande Collaboration used atmospheric neutrinos as the source, generated by the cosmic rays interaction with the atmosphere and mainly coming from the pions/kaons decayed. The difference in up-going or down-going events is caused by a difference in the experienced distance, because in one case the neutrino crosses only the atmosphere while in the other it must travel through all Earth. So it was possible to plot the fraction of the events observed as a function of the angle and observe a modulation. The modulation is given by the difference of the squared values of the masses.

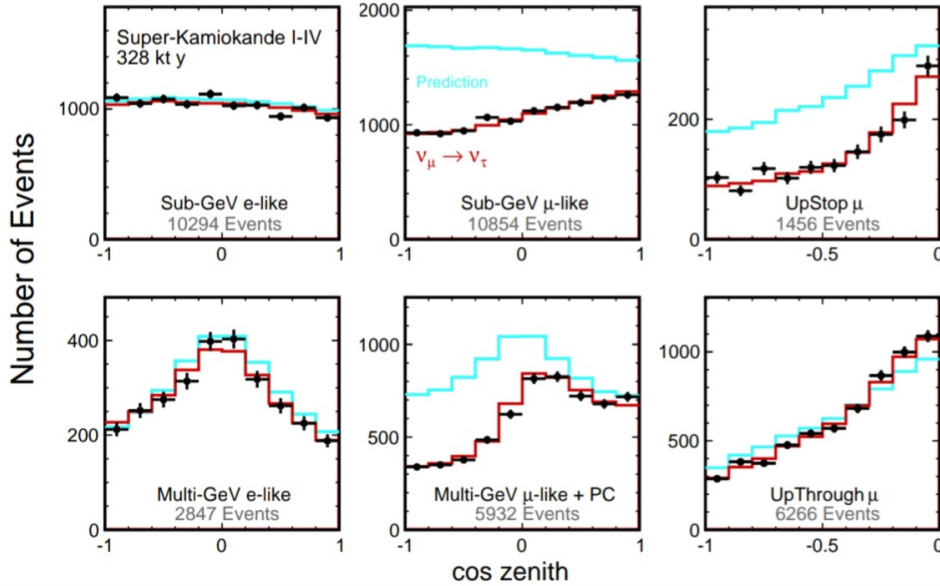


Figure 1.1: Example of the plots of the number of events as a function of the zenith angle from the upgraded Super-Kamiokande experiment. The blue histograms show the non-oscillated Monte Carlo events, and the red histograms show the best-fit expectations for neutrino oscillations [16].

A more advanced model has been developed over the years and the transition probability from one flavour state to the other is:

$$P(\nu_\alpha \rightarrow \nu_\beta) = \left| \sum_{i=1}^3 U_{\beta i}^* e^{-iE_i t} U_{\alpha i} \right|^2 = \delta_{\alpha\beta} - 2\Re \left[\sum_{i>j} U_{\alpha i}^* U_{\beta i} U_{\alpha j} U_{\beta j}^* \left(1 - \cos \frac{\Delta m_{ji}^2 L}{2E} \right) \right] + 2\Im \left[\sum_{i>j} U_{\alpha i}^* U_{\beta i} U_{\alpha j} U_{\beta j}^* \sin \left(\frac{\Delta m_{ji}^2 L}{2E} \right) \right]$$

where $\Delta m_{ji}^2 = m_i^2 - m_j^2$ and $\delta_{\alpha\beta} = \sum_i U_{\beta i}^* U_{\alpha i}$.

It is important to note that even this model is simplified because neutrinos develop an enhancement in the probability transition, they travel through materials with variable density.

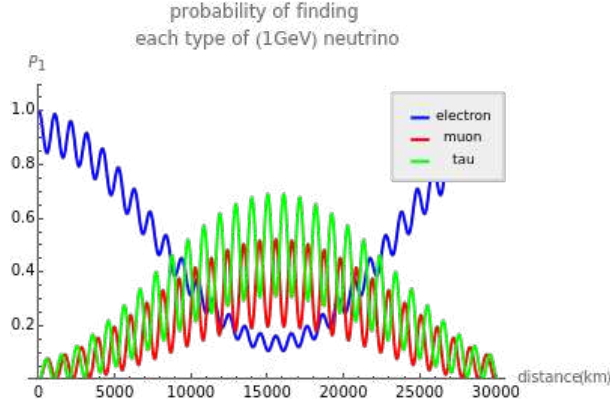


Figure 1.2: Simple plot of the probability of finding an electron, muon or tau neutrino starting from an electron one, as a function of the distance. Interactively it is possible to change the mass difference and obtain different plots using the Wolfram program at [31].

An analogy can be drawn with light waves in matter, where the speed of light differs from that in vacuum, leading to a refractive index $n \neq 1$. This means that photons in a medium acquire an effective mass different from zero due to their interaction with matter through coherent forward scattering. Similarly, neutrinos in matter also have $n \neq 1$, implying that their effective masses differ from those in vacuum. All types of neutrinos interact with matter via neutral currents, but only electron neutrinos interact with electrons in the medium through charged currents. This results in a difference in the interaction probability at a given location r , which affects the refractive index of ν_e . Consequently, ν_e acquires an effective mass that depends on the local electron density. This results in a significant effect on neutrino propagation and it is called Mikheev-Smirnov-Wolfenstein effect, or MSW effect. This phenomena is much more relevant in the case of solar neutrinos calculations, as the electron density is higher than in the Earth or atmosphere.

As of now the missing component not present in the neutrino oscillation probability calculations is the CP phase. A charge-parity transformation exchanges particles with antiparticles, thus the presence of an imaginary part on the PMNS matrix causes a change from $U_{\alpha i}$ to $U_{\alpha i}^*$. This is reflected on the transition probability by a change in sign of the imaginary part. It is possible to define an asymmetry parameter that allows to easily determine numerically from data the CP phase (because it reduces systematic effects). The asymmetry between two flavour states oscillation is defined as

$$A_{\alpha\beta}^{CP} = P(\nu_\alpha \rightarrow \nu_\beta) - P(\bar{\nu}_\alpha \rightarrow \bar{\nu}_\beta) = +4\Im \sum_{i>j} U_{\alpha i}^* U_{\beta i} U_{\alpha j} U_{\beta j}^* \sin\left(\frac{\Delta m_{ji}^2 L}{2E}\right)$$

this can be rewritten, in the case of muon-electron oscillation, as it is for the T2K experiment, in the form

$$A^{CP} = 16J \sin\left(\frac{\Delta m_{12}^2 L}{4E}\right) \sin\left(\frac{\Delta m_{23}^2 L}{4E}\right) \sin\left(\frac{\Delta m_{13}^2 L}{4E}\right)$$

with the Jarlskog invariant

$$J = c_{12}c_{23}c_{13}^2 s_{12}s_{23}s_{13} \sin \delta_{CP}$$

The Jarlskog invariant is proportional to the area of the unitary triangle, as it is for the CKM matrix in the Wolfstein parametrization, and so it defines directly the presence or not of the CP violation. If it is different from zero there is a CP violation.

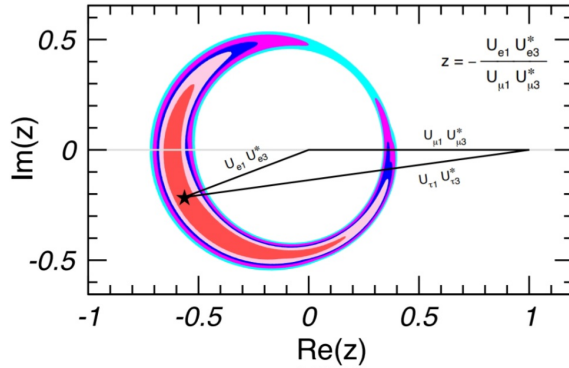


Figure 1.3: The unitary neutrino triangle, with the two fixed vertices at $(0, 0)$ and $(1, 1)$, and the contour plot for the significance level for the third point. Up to date plot of 2024 [16].

Before the shutdown for the upgrade of 2021, T2K confirmed the possibility of a non zero CP violation in the leptonic sector, specifically $\delta_{\text{CP}} = -1.89^{+0.70}_{-0.58}$ for the normal ordering and $\delta_{\text{CP}} = -1.38^{+0.48}_{-0.54}$ for the inverted ordering [32]. The next upgrade and following data taking will allow for more precise measurements on this important parameter, important not only for the Standard Model but also for cosmological theories on the asymmetry matter-antimatter.

1.2 The neutrino mass problem

It is now clear theoretically and experimentally that the phenomena of oscillation allows to determine the terms Δm_{ji}^2 . Unfortunately there is no indication on what should be the absolute mass of each neutrino and in what order the neutrino mass should be. Specifically this problem is called "the neutrino mass ordering problem".

For the ordering, mathematically we can have the two possible configurations

$$m_3 > m_1 \Rightarrow \Delta m_{13}^2 = \Delta m_{21}^2 + \Delta m_{23}^2$$

$$m_1 > m_3 \Rightarrow \Delta m_{13}^2 = \Delta m_{21}^2 - \Delta m_{23}^2$$

with $m_2 > m_1$ known from solar neutrino data regarding the oscillation electron-muon neutrinos. The first case is called "Normal Ordering" while the second "Inverted Ordering".

Regarding the absolute mass value of the neutrinos there are different and experimentally interesting processes that are involved. One example is the Katrin experiment in Germany, that tries to measure at an excellent level of precision, using a magnetic spectrometer, the energy spectrum of the electrons emitted via β decay from a trizium source [5]. It is then possible to determine from nuclear models the expected end-point energy, the maximum available energy of the electron if the neutrino is massless, and compare it with the experimental one. Future methods will use the time of flight of the neutrinos from supernovas or could use the neutrinoless double β decay.

The neutrinoless double β decay is an especially interesting phenomena for the CP violation. The theory of the Standard Model defines that the mass term of the fermions is given by the coupling of a left and right-handed spinor bilinear. Experimentally, the right-handed neutrino has not been observed (it is inert under the electroweak and QCD interaction), so it is possible that this process is not behind the mass acquisition.

A different model has been proposed by Ettore Majorana that allows spinors to acquire mass without its right-handed component only if the particle is its own antiparticle. In this case, the

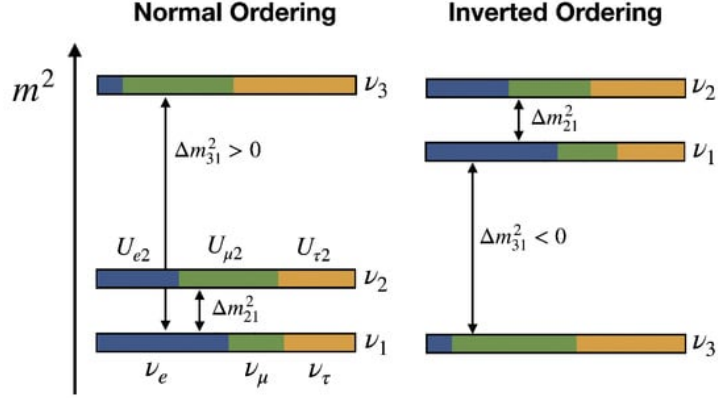


Figure 1.4: The two possible configuration in normal or inverted ordering, with the color indicating the probability of finding each neutrino flavor in the mass eigenstate.

neutrino would not be a Dirac particle but a Majorana one. Concerning the neutrino oscillation, the PMNS matrix of the Majorana fermions would acquire two new complex phases $\mu_{1,2}$ in addition to the CP one. Unfortunately, the transition probability from one state to another is not sensible to these new phases, thus specific experiments must be carried out for their determination. An example of that could be to observe the possible neutrinoless double β decay, in which two protons/neutrons decay to two neutrons/protons emitting two electrons/positrons but no neutrinos. In the Feynman diagram, the neutrino acts as a propagator due to its particle-antiparticle nature, but only if it is a Majorana particle. In the energy spectrum, the sum of the electrons would generate a peak at the exact energy of the Q-value, showing that there is no other particle involved in the process [21].

1.3 State of the art

As it has been said, the experimental evaluation of the PMNS matrix elements is improved by maximizing $\frac{\Delta m^2 L}{4E}$. This differentiation can be achieved by using different sources, changing the distance and the energy spectrum. The current experiments are classified in

- **Solar**, which use only electron neutrino, by flux difference with the expected rate from astronuclear models it is possible to measure its disappearance enhanced by the MSW effect.
- **Accelerators**, that produce electron and muon neutrinos, and so from the appearance or disappearance of each species it is possible to determine the two tau neutrino angles (the tau neutrino is not produced in a sufficient rate to talk about any specific tau neutrino source).
- **Nuclear reactors**, that produce mainly $\bar{\nu}_e$ and can be used to determine more precisely the angles for the appearance and disappearance of the electron neutrino, thanks to the control and check of the flux.

Another difference is from MBL (Medium BaseLine) and LBL (Long BaseLine) experiments, with "BaseLine" defined as the distance traveled by neutrinos. In this case the flux is controlled by a detector near the source, this helps alleviate systematic uncertainties.

Table 1.1 shows a summary of the possible configuration and which is the best parameter to determine.

| Experiment | Dominant | Important |
|---|-------------------------------------|-------------------------------------|
| Solar Experiments | θ_{12} | $\Delta m_{21}^2, \theta_{13}$ |
| Reactor LBL (KamLAND) | Δm_{21}^2 | θ_{12}, θ_{13} |
| Reactor MBL (Daya-Bay, Reno, D-Chooz) | $\theta_{13}, \Delta m_{31,32}^2 $ | $\theta_{13}, \Delta m_{31,32}^2 $ |
| Atmospheric Experiments (SK, IC-DC) | $\theta_{23}, \Delta m_{31,32}^2 $ | θ_{13}, δ_{CP} |
| Accel LBL $\nu_\mu, \bar{\nu}_\mu$, Disapp (K2K, MINOS, T2K, NO ν A) | $ \Delta m_{31,32}^2 , \theta_{23}$ | θ_{13}, δ_{CP} |
| Accel LBL $\nu_e, \bar{\nu}_e$ App (MINOS, T2K, NO ν A) | δ_{CP} | θ_{13}, θ_{23} |

Table 1.1: Oscillation parameter measurements and different experiments that will determine them with higher precision [16].

It is important to note two experiments JUNO (Jiangmen Underground Neutrino Observatory) and DUNE (Deep Underground Neutrino Experiment), that will give promising results. JUNO is expected to determine the mass ordering at $3 - 4\sigma$ significance by detecting reactor $\bar{\nu}_e$ and using the energy spectrum, which depends on the correct ordering. It is composed of an acrylic sphere filled with liquid scintillator observed by around 38000 PMTs and an energy resolution of 3% at $1MeV$. The neutrino source is provided by the Yangjiang and Taishan nuclear power plants. It is estimated to start taking data in 2025 [33]. DUNE will instead test, apart from the CP violation, the mass ordering, will importantly study supernovae neutrinos, and conduct searches for the proton decay and the sterile neutrino (the right-handed neutrino) [4]. DUNE will use neutrinos generated at Fermilab and a far detector at the Sanford Underground Research Facility in the United States. Data taking will start in 2032 for more than 20 years. The far detector is the Liquid Argon Time Projection Chamber (LArTPC), with a total volume of $70ktons$.

The up to date values of the 4 parameters are listed in table 1.2.

| | Normal Ordering | Inverted Ordering |
|---------------------------------------|---------------------------------|---------------------------------|
| $\sin^2 \theta_{12}$ | $0.307^{+0.012}_{-0.011}$ | $0.308^{+0.012}_{-0.011}$ |
| $\theta_{12}/^\circ$ | $33.68^{+0.73}_{-0.70}$ | $33.68^{+0.73}_{-0.70}$ |
| $\sin^2 \theta_{23}$ | $0.561^{+0.012}_{-0.011}$ | $0.562^{+0.011}_{-0.010}$ |
| $\theta_{23}/^\circ$ | $48.5^{+0.7}_{-0.9}$ | $48.6^{+0.7}_{-0.9}$ |
| $\sin^2 \theta_{13}$ | $0.02195^{+0.00054}_{-0.00058}$ | $0.02224^{+0.00056}_{-0.00057}$ |
| $\theta_{13}/^\circ$ | $8.52^{+0.11}_{-0.11}$ | $8.58^{+0.11}_{-0.11}$ |
| $\delta_{CP}/^\circ$ | 194^{+24}_{-22} | 284^{+26}_{-28} |
| $\Delta m_{21}^2 \times 10^{-5} eV^2$ | $7.49^{+0.19}_{-0.19}$ | $7.49^{+0.19}_{-0.19}$ |
| $\Delta m_{32}^2 \times 10^{-3} eV^2$ | $+2.534^{+0.025}_{-0.025}$ | $-2.510^{+0.024}_{-0.025}$ |

Table 1.2: Up to date values on the neutrino oscillation parameters [16].

Chapter 2

The T2K experiment

The T2K experiment is one of the leading collaborations in neutrino physics and especially in the long baseline accelerator method. The term T2K stands for "from Tokai to Kamioka" which are the two locations in Japan where are located, respectively, the accelerator-near detector and the far detector. The accelerator is the Japan Proton Accelerator Research Complex (J-PARC), the near detector is called ND280, and located at around $280m$ from the neutrino beamline, while the far detector is SuperKamiokande, in the Kamioka mines at $295km$ from Tokai. Since 2021 the first two structures underwent an upgrade phase that lasted until the end of 2024.

Now I will describe the new and updated setup. This experimental new phase is called T2K-II and will last from 2023 to 2026. In 2027 the new upgraded HyperKamiokande is estimated to begin data taking. HyperKamiokande will be located in a cavern near SuperKamiokande, so this last will continuously collect data even during the upgrade. During the upgrade the modifications have been applied to the J-PARC neutrino beamline accelerator and only to the front part of the ND280 detector.



Figure 2.1: Location of the 3 structures of the T2K experiment.

It is useful to describe the neutrino beam's path from the source to the far detector to understand all the components and what are the problems and their solutions. I will start by describing J-PARC.

2.1 J-PARC

The T2K collaboration aims to accumulate a total of $2 \cdot 10^{22}$ protons-on-target events in the next decade, aiming at observing CP violation with 3σ or higher significance in the case of maximal

CP violation. Thus the J-PARC accelerator must maintain a high rate of events and a purity of the beam in the energy spectrum of interest.

J-PARC is a proton synchrotron with a dedicated neutrino beamline. To obtain a neutrino beam experimentally, the method used is exploiting the different decay products from charged particles (like pions and kaons) produced in proton-target collisions. The produced elements of this collision can be controlled and focused into a tight beam, which, after decaying, generates particles forward in direction, one of which can be a neutrino. This method was first developed by Pontecorvo and, during the decades, underwent improvements concerning the focusing of the charged particles and their production mechanism. In proton-target collisions, the main elements produced are pions; the branching ratio of pions to decay into a muon-neutrino pair is 99.9%. This is the reason why the neutrino beam is composed mainly of ν_μ . Kaons also decay toward the same states, producing ν_μ with a branching ratio of 63%. The presence of muons, of course, enhances both the electron and muon neutrino components due to their decay. The purity in muon neutrinos is assessed by ND280, and as we are specifically observing muon neutrino transition, the presence of electron neutrinos in the beam creates a systematic error.

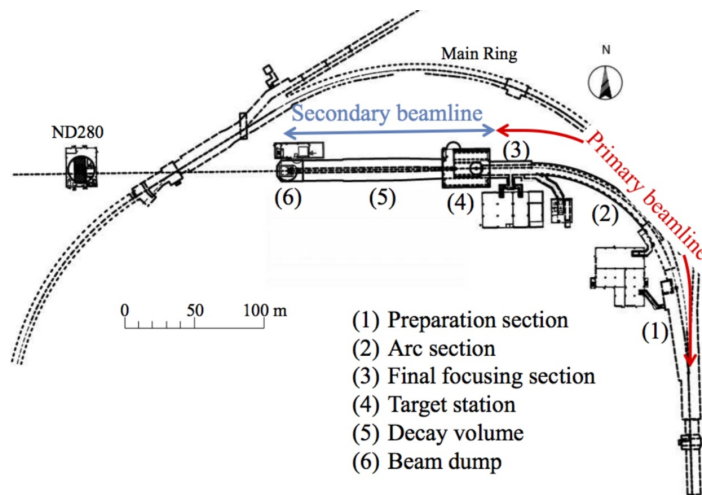


Figure 2.2: Technical drawing of the neutrino beamline at J-PARC.

Returning on the case of J-PARC, the proton synchrotron beam is at an energy around 30GeV , so it is necessary to move it to the dedicated neutrino beamline and then to be sent to the target. First, a preparation section extracts the beam, assuring that it is tuned in position and width with normal-conducting magnets in order to match the beam optics at the arc section. The beam is then bent by 80.7° toward the direction of Kamioka. A final focusing sector is used to improve the proton beam dispersion. Next is included a target station that contains a graphite collimator (called Baffle), the target, and the three magnetic horns. The target consists of a graphite rod of 2.6cm in diameter, which is contained in a titanium container with high-purity helium gas. The remnant of the proton beam, meaning those protons that did not interact and thus proceed linearly, is deposited in the beam dump at the end of the decay volume. The beam dump dissipates approximately one third of the total beam power.

The main sources of error present in this process are in the proton-target interaction calculation (which produces systematic errors dependent on the QCD model applied) and in the beam dynamics. These two induce effects on the flux determination for the calculation of neutrino survival/disappearance probability.

Regarding the flux control, the future of possible long baseline experiments is also limited by the determination of the neutrino cross section in the near detector as a function of the energy.

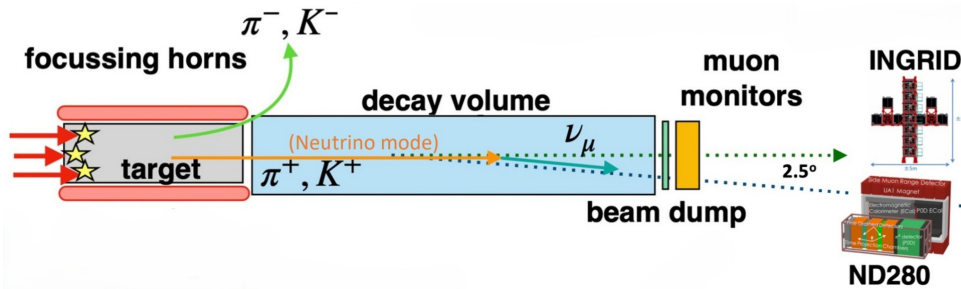


Figure 2.3: Drawing of the neutrino beamline, selecting neutrinos. By changing the current flowing in the magnetic coils it is possible to select neutrinos or anti neutrinos.

A simple flux calculation for the cross section is limited in resolution and is dependent on the QCD and the beam. Concerning this matter, an example of future innovation here in Padova is the ENUBET (Enhanced NeUtrino BEams from kaon Tagging) [34] project that is working toward the most stable neutrino beam aimed at measuring this cross section. In this case, the ENUBET project will help develop more precise measurements on the neutrino cross section, up to one tenth of the up-to-date error. As stated before, the reason for the creation of the T2K was also to estimate the neutrino interaction cross section, but because more precise tests on the standard model are needed, this technique has reached a technological endpoint. ENUBET will use an instrumented decay tunnel and, by observing the kaons and pions decay, it will be able to precisely determine the flux directed to a neutrino detector.

In T2K, in order to increase the resolution, it is then important to generate a beam in energy that maximizes the oscillation. Calculations using the known angles of the PMNS matrix and simulating the J-PARC neutrino beamline (while using the modeling of hadronic interactions from NA61/SHINE data) have been extensively conducted. The most sensible energy range and off-axis band angle (defined as the angle between the proton beam direction and the accelerator-far detector direction, so the angle between the neutrino beam and the far detector) has been determined so that the sensibility to the CP phase and to the survival probability is maximized. The best energy range is around 0.6GeV with an off-band axis orientation of 2.5° , this means that the decay tunnel is slightly tilted downward compared to the Tokai-Kamioka direction.

2.2 ND280

The second component of the experiment is the ND280 detector. This thesis particularly involves this apparatus, thus it is well described to understand the physical motivations behind some restraints imposed on the development of the TPCs.

ND280 [3] is composed of different detectors. The first three described (super-FGD, HATPC and TOF) are the new components developed during the upgrade.

The ND280 tracker is optimized to study Charged Current Quasi Elastic (CCQE) neutrino interactions. The neutrino energy can be determined by observing only the muon or electron generated in CCQE by measuring its momentum. It is possible, using a simple equation, to obtain

$$E_\nu^{\text{rec}} = \frac{2(m_n - V)E_\ell + m_p^2 - (m_n - V)^2 - m_\ell^2}{2(m_n - V - E_\ell + p_\ell \cos \theta_\ell)}$$

with $V \approx 27\text{MeV}$ the bounding energy neutron energy.

The components of the detector are located inside a basket structure surrounded by the UA1 magnet, thus the intensive use of SiliconPhotoMultiplier (SiPM), insensitive to the magnetic field

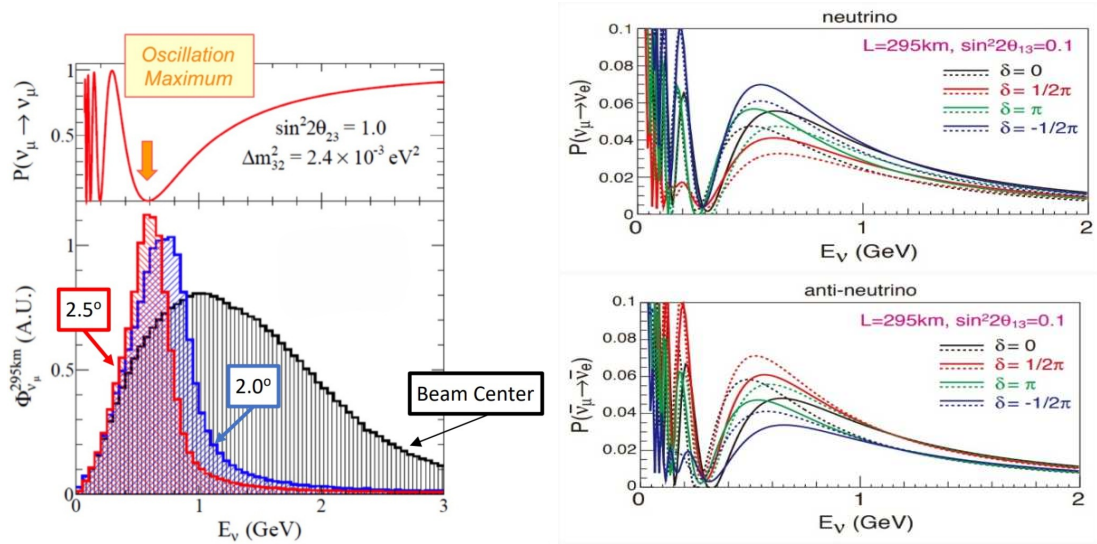


Figure 2.4: On the left it is possible to visualize the spectrum for the three angular configuration and the best one is the one with the peak at the probability minimum. On the right it is possible to see that, in the maximum of the transition probability there is a better discrimination for different CP phases.

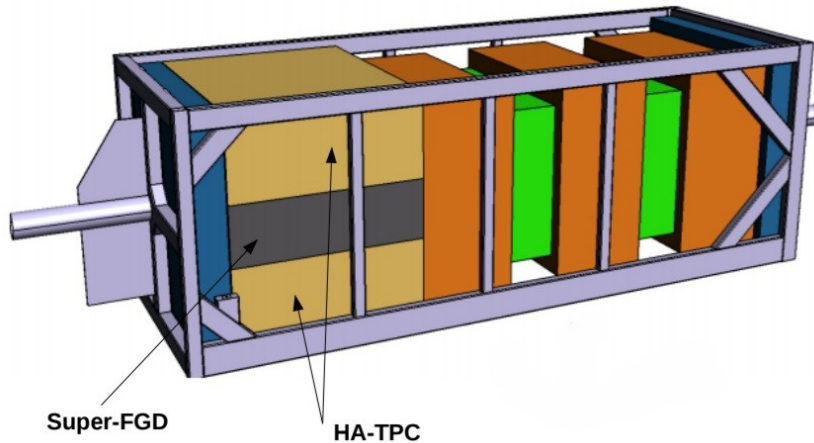


Figure 2.5: Technical drawing of the ND280 detector. In green the FGDs, in gray the super-FGDs, in blue the ECAL that surrounds all the system and is divided in two sections, in orange the tracking TPC, in yellow the HATPC. Around the front part surrounding the HATPC and the super-FGDs there is the Time-Of-Flight detector. The neutrino beam comes from the left in the image.

(compared to PMTs). The detector is composed of

- **Super-FGD** (Super Fine Grained Detector). It is composed of cubes of plastic scintillators readout by three wavelength shifter optic fibers, each instrumented with a SiPM. The three wavelength shifters allow to determine the event in the three spatial directions. The SuperFGD is composed of $192 \times 192 \times 56$ cubes, with the size of each cube being $1 \times 1 \times 1 \text{ cm}^3$. Compared to the previous version, which was called POD, the dark noise rate and the crosstalk probability have been reduced by an order of magnitude. The Super-FGD provides the target mass for the neutrino interaction inside of ND280, with a total

mass of approximately 2 tons , therefore allowing a precise vertex interaction determination. Additionally it is possible to precisely reconstruct the events at low energy that don't enter in the TPC. It is used to reconstruct the tracks around the interaction vertex, for any energy event.

- **Time-of-Flight Detectors.** They are used to determine the time to cross the two TPCs for the track reconstruction, with a time resolution on the order of 100ps and they are used to provide additional information on the particle identification with the TPCs. Six planes of plastic scintillator bars fully cover the target and the two High-Angle Time Projection Chambers (HATPCs). Each bar is equipped with a $6 \times 6\text{mm}^2$ SiPM. The time information helps in the vertex interaction determination. It also acts as veto detector.
- **High-Angle Time Projection Chambers.** They will be described in the next chapter in full details.
- **Electromagnetic calorimeter.** It is a lead-scintillator sampling calorimeter divided in three regions: the P0D-ECal, (which surrounded the P0D and now surrounds the Time-Of-Flight detector), the barrel-ECal (which surrounds the inner tracking detectors), and the Ds-ECal (which is located downstream of the inner detectors and occupies the last 50 cm of the basket). The barrel-ECal and Ds-ECal together are referred to as the tracker-ECal. Each module consists of layers of scintillating polystyrene bars with cross-section $40\text{mm} \times 10\text{mm}$ bonded to lead sheets that are 1.75mm thick. Scintillator bar widths and lead thickness and the number of layers per module were optimized for particle identification and tracking information. The light produced in the scintillator bars is transported via WLS fibers to the SiPMs.
- **ν TPCs.** They are used to perform two important functions for the near detector: imaging for the number of particles, PID and tracking which form the basis for event selection and purity. Each TPC contains an argon-based drift gas, precisely the T2K composition $Ar : CF_4 : isoC_4H_{10}(95 : 3 : 2)$, chosen for its high speed, low diffusion, and good performance with MICROME GAS. It is contained within an outer box that holds CO_2 as an insulating gas. The inner walls are made from composite panels G10 layers, a dielectric material. The strip pitch is 11.5mm and using a central cathode panel an uniform electric field in the perpendicular direction of the beam is produced. The readout electronic for the drifting electrons is a bulk MICROME GAS anode pad. In general, a MICROME GAS, is a mesh with holes of the order of $50 - 100\mu\text{m}$, thus there is a strong field allowing for multiplication, generating a stronger signal. The developed avalanche induces a signal only in the hit pad and the readout signal is read by an ASICs called "AFTER", which is used also for the HATPCs.
- **FDGs.** Two FDGs are present. The one upstream with respect to the beam is constructed from bars of extruded polystyrene scintillator, which are perpendicular to the beam direction. Each scintillator bar is covered in reflective coating of TiO_2 and a WLS fiber is inserted at the center, attached only on one side to a SiPM and associated electronics. The FDG consists of 30 layers of 192 bars each, with each layer oriented alternatively in the x and y directions perpendicular to the neutrino beam. The second FDG is a water-rich detector consisting of seven XY modules of plastic scintillator alternating with six 2.5cm thick layers of water. These layers are made from sheets of thin-walled hollow corrugated polycarbonate which is 2.5cm thick, whose ends have been sealed. The modules are then filled with water to provide a layer of water target. The water is maintained under sub-atmospheric pressure by a vacuum pump system so that if a leak develops the system will

suck air into the modules rather than spilling water inside the FGD. Comparing the interaction rates in the two FGDs allows separate determination of cross sections on carbon and on water. Both FGDs were built with the same geometry, mounting, and readout for interoperability.

- **UA1 magnet.** It is recycled from the UA1 CERN experiment, it generates a uniform $0.2T$ magnetic field, and surrounds the entire basket. The magnet consists of two halves which are mirror symmetric to a vertical plane containing the beam axis. Each half consists of 8 C-shaped flux return yokes. The magnet is instrumented with scintillator planes intersected into the gaps called Side Muon Range Detector (SMRD). The SMRD is implemented to detect muons escaping from the detector at large angles (compared to the beam direction, relevant for CCQE in the T2K energy range). It acts as veto for cosmic ray muons that penetrate the ND280 detector. It also helps determine the event interactions with the iron on the magnet and walls environment.

Additional detectors for further neutrino studies are located in the same building as the ND280 detector. **INGRID** is located under the ND280 detector so that it is on-axis to J-PARC, the beam width is $\sigma = 5m$ at $280m$ and INGRID is designed to sample the beam in a transverse section of $10m \times 10m$ thanks to a cross shape structure.

INGRID is composed of 14 identical modules. Each module consists of a sampling layers of iron and tracking plastic scintillator planes and it is surrounded by veto scintillator planes. The length of the scintillator bars is around $120cm$ and a hole of about 3 mm at the center of the scintillator bar allows the insertion of a wavelength shifting fiber, one side is connected to a SiPM.

WAGASCI-BabyMIND is located next to the INGRID and ND280 detectors. It is the WAtEr Grid And SCIntillator Magnetized Iron Neutrino Detector. The project aims to improve measurements of the ratio of neutrino cross sections on water and carbon, using charge identification and momentum measurements for muons. WAGASCI is composed of a segmented target of water and scintillator cells, where the cross section can be measured in both media simultaneously. Baby MIND is equipped with 18 scintillator modules using two MRD instrumented with WLS and SiPMs.

The upgrade succeeded in its main goals, which were to increase the resolution on the reconstruction of the kinematics [3].

- Full coverage is achieved by the construction of the HATPC in the top and bottom and especially by the TOF detector.
- Vertex reconstruction is improved because the highly segmented super-FGD has been added, whereas before the main components for vertexing calculations were only the two TPCs and the three FGD.
- Allows reconstruction of the scattered nucleon kinematics thanks to the granularity and the lowered threshold of the super-FGD. It has been especially improved the neutron detection, thus reducing the nuclear model dependence in the neutrino energy reconstruction.

2.3 Super-Kamiokande

The Super-Kamiokande detector [14] is located 2700 m water equivalent under the Mt. Ikeno in the Kamioka mines. The detector consists of an inner and an outer detector divided by a cylindrical stainless steel structure. The Super-Kamiokande detector started data taking in 1997

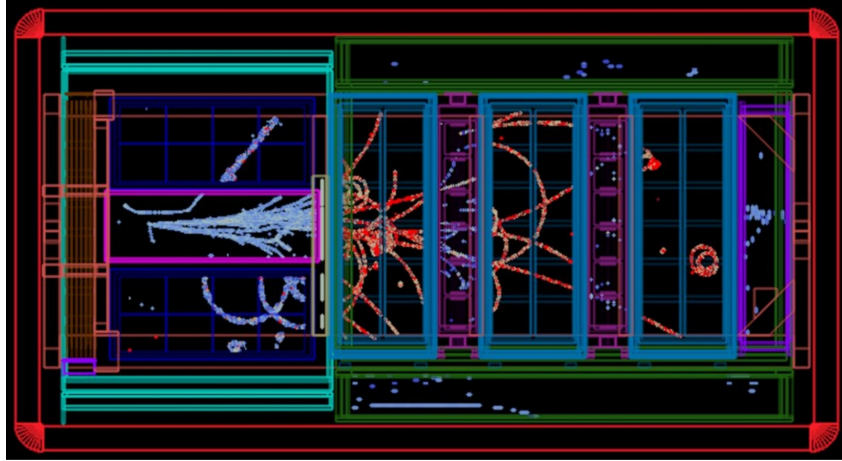


Figure 2.6: Event display for the upgraded detector during the 2024 neutrino beam test.

and it is still operative. It has discovered the first evidence of neutrino oscillation in atmospheric neutrinos, confirmed the solar neutrino oscillation, defined the most accurate upper limit for the proton decay and worked with T2K to observe neutrino's appearance and disappearance. The electronics, after an upgrade in 2008, is also capable of implementing a coincidence trigger with a beam arrival time. In 2020, another upgrade was done with an addition of gadolinium, which is expected to increase the sensitivity to observe neutrinos. In particular, the first supernova relic neutrinos (SRNs) are expected to be observed [29].

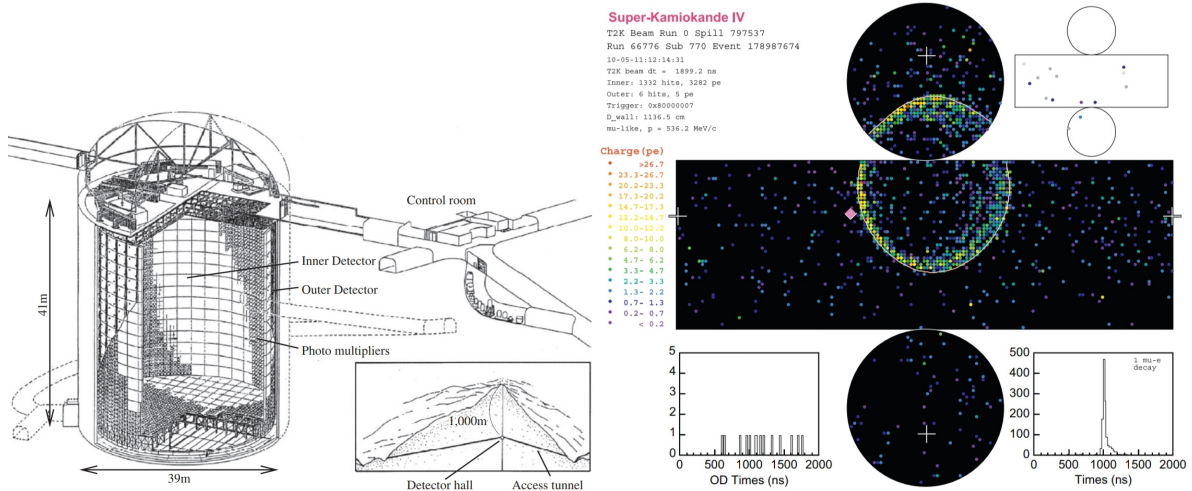


Figure 2.7: On the left a drawing of the Super-Kamiokande experiment, while on the right an event display of a muon ring image as visualized by the PMTs.

The inner detector is a cylindrical vessel with a diameter of $33.8m$ and a height of $36.2m$ in which around 11000 PMTs of $50cm$ in diameter are attached. The outer detector is a cylindrical container about $2m$ larger. In the walls 1900 outward-facing PMTs ($20cm$ long in diameter) are inserted. Both are filled with ultrapure water. The two detectors are optically isolated from each other. The inner vessel is covered in a black sheet to block light while the walls of the outer detector are covered with reflective material due to the lower number of PMTs. The outer vessel PMTs is capable of an almost 100% rejection efficiency of cosmic muons.

The PMTs observe the Cherenkov cone light emitted from the lepton in CCQE events: this

allows for an easier particle identification between muon or electron neutrino. In particular, electrons have fuzzier rings due to the electromagnetic shower in water. The Super-Kamiokande software uses this difference to determine the neutrinos' flavour. In addition, the Cherenkov cone allows the reconstruction of the vertex position using the time difference in the PMTs' signals arrival time. For the determination of the lepton's charge, the recoiled nucleus is identified.

Chapter 3

The HATPC and the experimental setup

In this section I describe three elements:

- The **HATPCs**, already installed at the near detector at Tokai. I did not work directly with them but it is important to mark the similarities and differences with the experimental setups I directly used.
- The **Short Cathode Prototype** or **mTPC**. This is a smaller version of the T2K TPC created as a first model. During previous internship activities, I started from a semi-scratch prototype and ended up detecting cosmic muons (a detailed report is present at [24]). In the end I was able to create a fully functional TPC which I use in my thesis work to test some characteristic that will be studied in the T2K field cage.
- The **Encapsulated Resistive Anode MICROMEGAS (ERAM)** is the detector with the electronics readout developed during the upgrade for the HATPC.

The prerequisites for the HATPCs detectors are fundamental in the ND280 detector for: track reconstruction, charge measurement, momentum measurement, particle identification (combining the measurement of momentum and $\frac{dE}{dx}$). Another important parameter is the resolution in separation between muons and electrons, crucial to estimate the contamination of electron neutrino on the beam, which is $\approx 1\%$. The resolution depends on the spatial resolution and the track length, and with the HATPC it has been achieved a separation of 4σ . From this consideration some constraint on the HATPC have been chosen, especially

- low-density and low-Z materials for the TPCs' walls, so that they do not exceed 4% of radiation length
- structural integrity to gas pressure, thermal loads and weight
- high electric field uniformity, with distortions of primary electrons of maximum $0.2mm$, less than the required position resolution
- low permeability to gases from the outside such as O_2 , N_2 and H_2O , lower than 10ppm, which are electron attractive gases and so reduce the signal of primary electrons
- high superficial resistivity, larger than $100\frac{T\Omega}{m^2}$

The HATPCs operate with the same gas mixture as the ν TPCs, the so-called T2K-gas mixture $Ar - CF_4 - isoC_4H_{10}$ with ratio 95:3:2, in an electric field of $275 \frac{V}{cm}$ and electron drift velocity $7.8 \frac{cm}{\mu s}$ at this specific electric field.

The electron drift velocity presents a plateau in the region of interest for T2K. This helps in the presence of disuniformity: if the electric field is stronger or weaker the drift velocity does not change rapidly and so the track is not deformed. This mixture has a high speed, low diffusion, and good performance with MICROMEAS detectors. When particles cross the gas, the CF_4 breaks down and so it is necessary to flux the gas to maintain constant the pressure of $\approx 1 atm$, while recycling around $\approx 90\%$ of the gas in the gas system (GHS). The GHS allows for a 3 to 5 volume changes per day in each TPC, with a rate of $3 \frac{m^3}{h}$.

3.1 Structure of the HATPC

At the end of June 2024 the two High Angle TPCs were assembled and commissioned with cosmic muons at CERN (so properly tested and approved based on a protocol that will be explained later) and later installed in ND280. The last HATPC was commissioned with the neutrino beam in June 2024.

| Parameter | Value |
|--|-----------------------------|
| Overall $x \times y \times z$ (m) | $2.0 \times 0.8 \times 1.8$ |
| Drift distance (cm) | 90 |
| Magnetic Field (T) | 0.2 |
| Electric field (V/cm) | 275 |
| Gas $Ar-CF_4-iC_4H_{10}$ (%) | 95 - 3 - 2 |
| Drift Velocity (cm/ μs) | 7.8 |
| Transverse diffusion ($\mu m/\sqrt{cm}$) | 265 |

Table 3.1: Experimental parameters of the HATPC.

The two TPCs, labeled bottom or top based on the position on the basket at ND280, are each composed of 2 Field Cages (FCs), with, within the middle, a central cathode at HV.

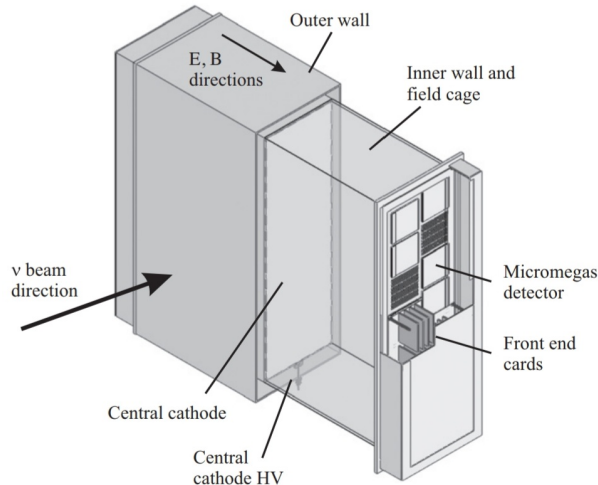


Figure 3.1: Layout of the HATPC.

The FCs construction was charged to the INFN sections of Padova and Bari. A FC has walls

composed of layers of different materials. The Aramid Fiber Fabric (Twaron) and the Aramide HoneyComb panel allow for low deformation on the FC under stress from the gas but also mechanical resistance, and compose the main structure in a sandwich of $35mm$ of honey comb and $2mm$ of twaron. These materials satisfy the constraint on the mechanical deformations allowed but are also light materials with low interaction length. On the outside a kapton foil of $125\mu m$ is placed for the final insulation and a layer of aluminum foil of $50\mu m$ is grounded. On the inside, from the twaron to the strips, there is a spaced out structure of kapton foils and resin layers to achieve maximum electrical insulation. Then there are the electrical strips, first a "mirror" strip layer and then a "field" strip layer, so that the electric field is more uniform compared to the case in which there is only one layer with the same strip pitch (in the case of the mTPC). To separate the two layers there is a final kapton foil. The corners of the FCs are reinforced with G10 fiberglass, due to the intense electric field in these regions. The strip layers were produced by the CERN laboratory of the Experimental Physics Detector Technology (EP-DT) and then attached on the twaron-honeycomb structure.

Between the two FCs, to form a single TPC there are 2 oblate o-rings, one teflon sheet (inserted in deep groves to avoid discharges), and the cathode that is fixed in position by four pins and connected to the HV via a feedthrough, at a potential of $27kV$. The cathode consists on two $1mm$ copper-clad attached to a G10 panel of $10mm$. On both sides of the TPC the frame is equipped with ERAM sensors.

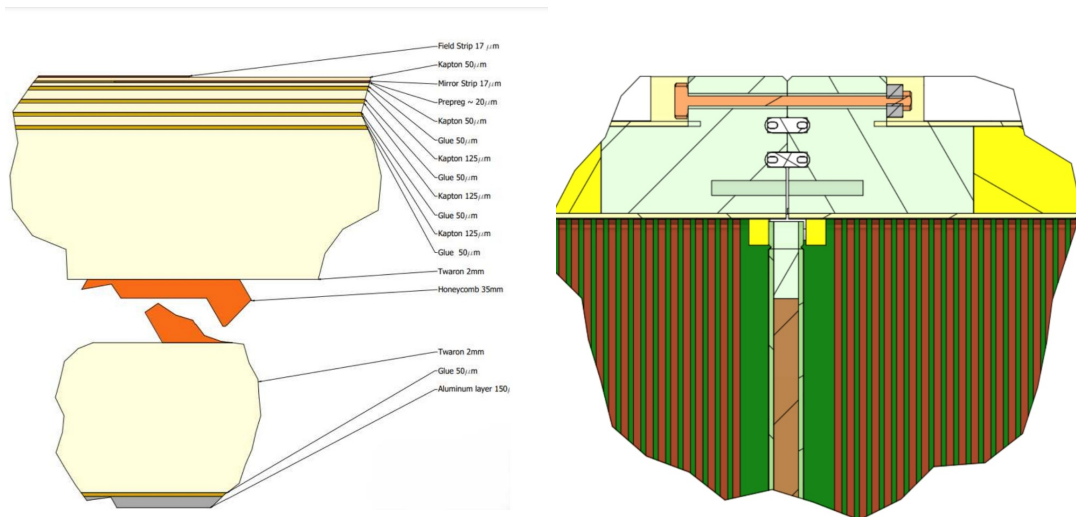


Figure 3.2: On the left the lateral section of the TPC layers, with the inside being the strip side and the outside being the aluminum foil, and on the right the section in the junction of the two FCs.

The strip pitch is $5mm$, with a strip width of $3mm$ and the resistive bridge is as shown in figure 3.4, created on the inside of the TPC with 391×2 in two parallel chains per cage, of Surface Mounted Resistances of $5.1M\Omega$, and a total of $1G\Omega$ resistance. These are specific flat resistances made so that their presence reduce disuniformity on the electric field. The electric field has a central uniformity in the fiducial volume that is better than 10^{-3} .

3.2 Structure of the mTPC

The mTPC presents a structure that is much different from that of the HATPC. The main differences are the absence of the mirror strips and the much smaller dimensions, thus this

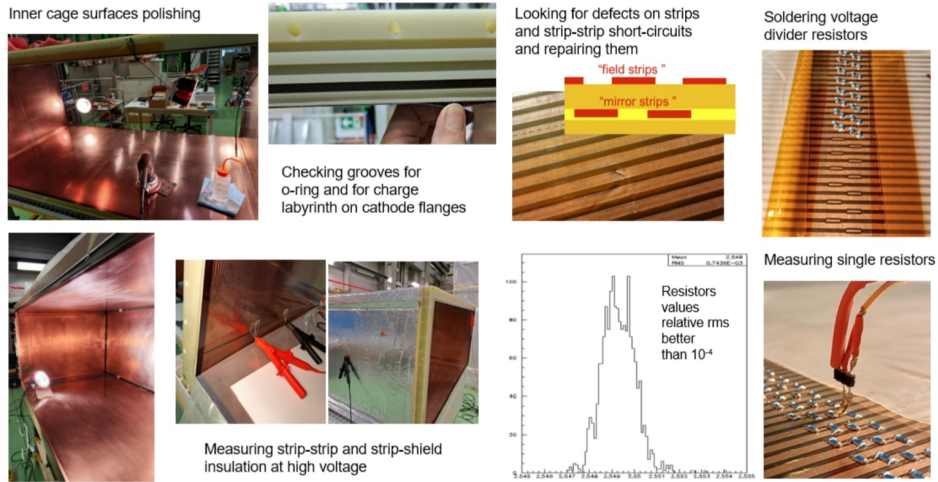


Figure 3.3: Recap of the check steps when the FC was delivered at CERN. The first step is a field cage polishing, the second is checking the flanges between the two FCs (as dust can induce a leakage), the third is the measurements of the insulation, strip by strip, and then the voltage divider is formed and checked at the HV value.

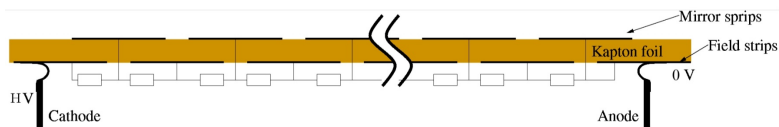


Figure 3.4: Voltage divider scheme for the field and mirror strips, as it is possible to see in figure 3.3 the mirror strips have a protuberance coming upward between two field strips, this are the square $2 \times 2\text{mm}$ pads, in this way it is possible to solder the resistance.

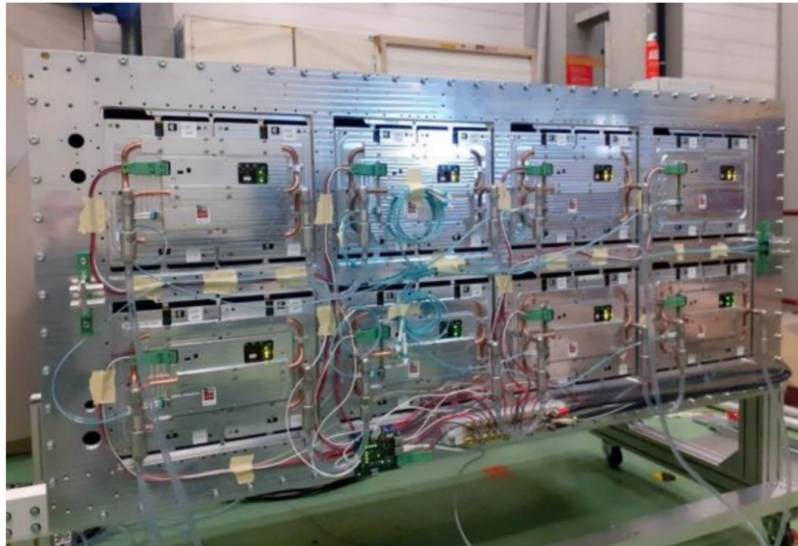


Figure 3.5: The ERAM modules mounted on the TPC. There are 8 ERAM modules for side.

generates a highly irregular electric field. The mTPC is composed of two FCs, the dimensions are $50.6\text{cm} \times 50.6\text{cm} \times 23.4\text{cm}$ with a wall thickness of 3.5cm composed of G10 material, an insulator glass resin with a relative dielectric constant of 5.0. In the G10 walls, 20 strips are present, and they were created by attaching a PCB layer and by excavating material from the PCB; thus, the four sides were soldered at the corners to electrically connect the four strips. The strips have a pitch of 10mm and a width of 6mm .

The two FCs are closed using G10 screws. In the middle of the two sections are present two oblate-shaped o-rings and a teflon sheet. The central cathode is composed of a G10 panel whose dimensions are $40.3\text{cm} \times 40.3\text{cm} \times 1.4\text{cm}$, with 2 PCB copper layers $50\mu\text{m}$ thick attached. The cathode is at the same potential as the first strip and the resistive bridge is composed of 19 mounted surface device resistors of $\approx 5\text{M}\Omega$. The missing resistance between the cathode and the first strip creates a region of constant potential and thus a low electric field, and it is the same for the HATPC. The last strip is grounded as the outside aluminum tape layer surrounding both FCs.

Two holes have been created, one for a laser source and the other for an x-ray source, the first one is between the sixth and the seventh strip, while the second is between the cathode and the first strip, with the aim of investigating this region of constant potential.

- **Quartz window** Between the sixth and seventh strip I drilled a hole in the G10 wall to point a laser inside the chamber, which will create straight tracks to determine the deformation on the electric field. It has a peculiar structure: it has the same diameter as the pitch between two strips (4mm) reaching the internal part of the TPC, but it is much larger on the outside of the chamber, with the same diameter as the quartz window (26mm) and a plane surface to accommodate it. The junction between the two parts has a small conical surface to increase the effective TPC volume where the laser can be pointed. The quartz window was glued to the G10 with epoxy resin so that the glue leveled the surface where the window sits, in order to avoid refraction and reflection of the laser light.

Only one FC is equipped with the ERAM detector while the other is closed with a grounded potential aluminum flat frame.

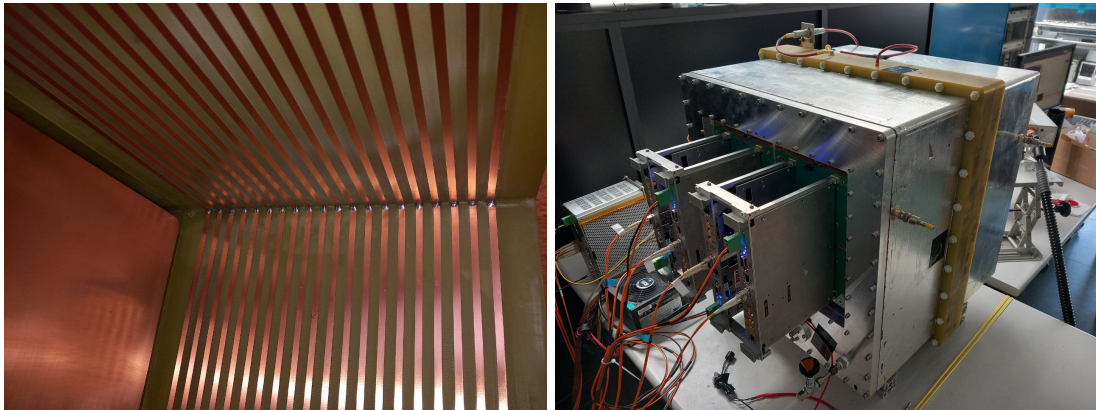


Figure 3.6: The interior of the mTPC on the left and with the electronics mounted on the right.

A scheme of the gas system is shown in figure 3.7: from the left I have the gas tank, which is connected to the fluxmeter. The gas bottle is connected via an 8mm Risan tube to a manual Vögtlin fluxmeter that regulates the flux entering the TPC. Next, a 8mm tube is connected to a particulate filter to clean the possible residues present in the bottle. Then the gas enters the chamber via a 6mm tube, using the connectors on the lower part of the ERAM frame, where a fine grained rotary valve is installed. In the output exhaust a safety bubbler is present.

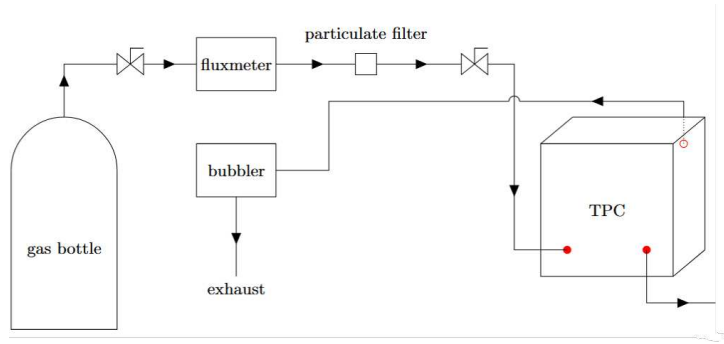


Figure 3.7: The gas system scheme.

The MICROMEAS is physically positioned near the last strip, which is grounded, and is mounted inside an aluminum frame with a hole; the pins are outside the TPC in order to be able to connect the electronics. The ERAM is attached to the frame on the side inside the chamber, so it is slightly closer to the cathode compared to the edge of the TPC. This configuration can generate a slight deformation of the electric field, as the frame and mesh, which are grounded, do not belong to the same plane and have a distance of a few millimeters.

3.3 The ERAM readout

Both for the HATPC and the mTPC the ERAM is the instrumented anode.

The ERAM technology was invented by a collaboration between the CERN/EP-DT-EF PCB workshop and CEA-IRFU. It works using a bulk-MICROMEAS (MICRO MESH Gaseous Structures), so a mesh on the μm size generates an increased amplification on the field and thus generates an avalanche for the incoming electrons, which is readout by metallic pads. As it is, the position resolution is limited by the pads' dimension; therefore, to increase it, a layer of insulator is attached in front of the pads. As the charge enters the insulator/resistive layer, it propagates radially slowly, slow enough to be detected by the underlying neighboring pads. As shown in figure 3.8 the signal is present in multiple pads, and thus it is possible to add the temporal information on the position of the initial electron cluster. In the T2K HATPC case, the MICROMEAS is composed of filaments $18\mu m$ long in diameter, with a pitch of $63\mu m$ in both perpendicular directions, so the squared gap has a size of $45\mu m$.

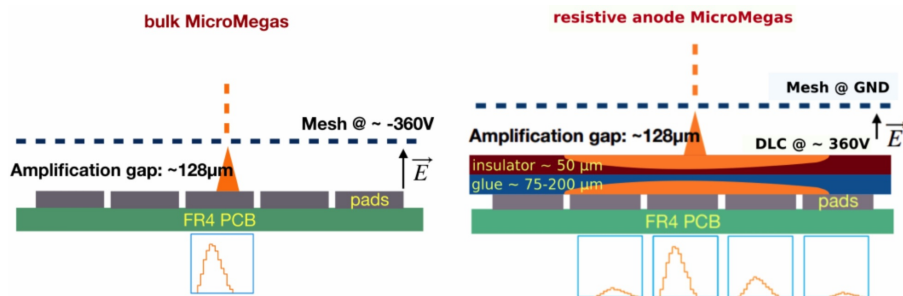


Figure 3.8: Difference in the signal between bulk and resistive MICROMEAS

The ERAM system is specifically composed of a mesh gap of $128\mu m$ sustained by pillars of stainless steel at grounded voltage. At top of the ERAM a less than $1\mu m$ thick layer of Diamond Like Carbon (DLC), produced by deposition by electron beam sputtering, is at a potential of

+380V. This allows for a gain of ≈ 1000 . Below a layer of $50\mu\text{m}$ APICAL, with a resistivity of $0.5\frac{M\Omega}{\text{m}^2}$, is attached to the PCB with $150\mu\text{m}$ of glue. The pads in the PCB are $11.18 \times 10.09\text{mm}^2$ of gold coated copper. In total the ERAM has a size of $42 \times 34\text{cm}^2$ with a total of 1152 pads, disposed in a matrix 36×32 . The presence of a resistive layer protects better, compared to bulk MICROMEAS, the electronic from potential spark. At the same time if dust is present between the mesh and the DLC it generates a bridge, while for bulk MICROMEAS it is possible to burn this impurities by increasing the voltage of the DLC, for the ERAM it is not possible.

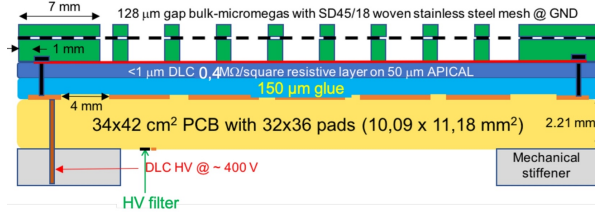


Figure 3.9: Drawing of the ERAM layout.

Mathematically the superficial charge distribution follows the law

$$\frac{\partial \rho(r, t)}{\partial t} = \frac{1}{RC} \Delta \rho(r, t)$$

with Δf the Laplace operator. The radial solution, considering an initial avalanche with Gaussian distribution with width ω and charge Q , is

$$\rho(r, t) = Q \frac{1}{2\pi\sigma^2} \exp\left(-\frac{r^2}{2\sigma^2}\right)$$

with

$$\sigma(t) = \sqrt{\frac{2t}{RC} + \omega^2}$$

the width evolution of the superficial charge as a function of the factor RC . The time evolution of the charge in each pads as a function of the initial position of the avalanche (x_0, y_0) is given by

$$Q_{\text{pad}}(t) = \frac{Q}{4} \left[\text{erf}\left(\frac{x^{\text{high}} - x_0}{\sqrt{2}\sigma(t)}\right) \text{erf}\left(\frac{x^{\text{low}} - x_0}{\sqrt{2}\sigma(t)}\right) + \text{erf}\left(\frac{y^{\text{high}} - y_0}{\sqrt{2}\sigma(t)}\right) \text{erf}\left(\frac{y^{\text{low}} - y_0}{\sqrt{2}\sigma(t)}\right) \right]$$

An example of signal is given in figure 3.10. It is possible to notice that the maximum for different pads is at different times, and in the analysis it is used the triplet $(x_{\text{pad}}, y_{\text{pad}}, t_{\text{max}})$ as an estimator for the position. Also, the kick around $x \approx 270\text{bins}$ is given by the ions' signal. In fact when the avalanche is created there is an initial fast electron signal, too fast to be detected. The ions' signal induced is observed, they go toward the cathode, and so crossing the mesh they get shielded, causing the kick. Another important step in the implementation of the signal readout is the elimination of the pedestal, given by the current between the mesh and the DLC.

An important parameter to understand the analysis of data is the RC pad-glue-resistive foil network in each region. Its determination was done by using a test bench at CERN to validate each ERAM with an x-ray ^{55}Fe source and by observing the convoluted signal [6]. For each ERAM the results show a mean RC value of $100\frac{\text{ns}}{\text{mm}^2}$.

The readout chip is based on the AFTER chip, an ASIC chip with 4096ADC and a pulse current of 120fC with peaking time of 200ns or 412ns . Each AFTER reads 72 channels in an array of 9×8 pads. The AFTER chip is composed of a Charge Sensitive Amplifier, a pole zero cancellation, a Sallen and Key Filter, a gain 2 amplifier and an analog memory of 511-cell

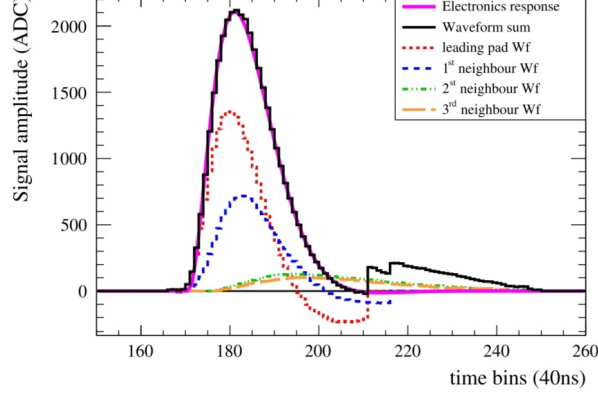


Figure 3.10: Example of the signals for the different pads as a function of the time.

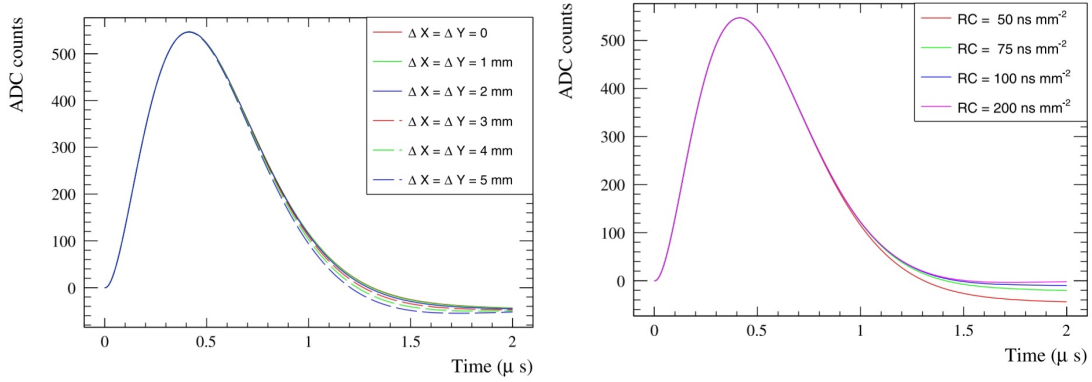


Figure 3.11: Signal formation from the simulation of the pads for different RC values and positions of the initial cluster.

switched capacitor array (SCA). When the electronics is triggered, the SCA is frozen and all cells are digitized by an Analog-Digital converter (ADC). Each ERAM module is composed of 16 AFTER that are located in the two Front End Cards (FECs). The FECs are read by a Front End Mezzanine (FEM) that synchronizes the signal digitization with a master clock and contains an internal buffer and a Pedestal Equalization Zero-suppression, the purpose of which is to remove the DLC current. Then via optic fibers the signal is sent to a custom board called Trigger and Data Concentrator Module (TDCM).

To effectively measure the position it is not sufficient to parametrize the charge distribution but also the response of the chip. The convolution necessary is $S(t) = Q_{\text{pad}}(t) * \frac{dADC_D(t)}{dt}$, where $\frac{dADC_D(t)}{dt}$ is the derivative of the electronic response function. The chip response for a Dirac current pulse is

$$f(t; \omega_s, Q) = e^{-\omega_s t} + e^{-\frac{\omega_s t}{2Q}} \left[\sqrt{\frac{2Q-1}{2Q+1}} \sin\left(\frac{\omega_s t}{2} \sqrt{4 - \frac{1}{Q^2}}\right) - \cos\left(\frac{\omega_s t}{2} \sqrt{4 - \frac{1}{Q^2}}\right) \right]$$

with ω_s the natural frequency and Q the quality factor. The ADC conversion is then $ADC_D(t; \omega_s, Q) = \frac{4096 ADC}{120 f C} \cdot \frac{f(t; \omega_s, Q)}{f(t; \omega_s, Q)_{MAX}}$.

In the mTPC electronics the FEM and FEC are merged, the AFTER chips are mounted directly in the FEM. This specific configuration is called "ARC readout".

The DAQ system is controlled by a perl script. Three scripts must be run: the initial "cold start" script, the "pedestal" and the "run" launcher. The first connects the pc to the FEMs and initializes them. To run the second script, the DLC voltage has to be set to 100 V to eliminate any avalanche and thus any physical signal; in this way, all we see is the baseline signal, which is mainly due to the DLC current. This script acquires data for less than a minute and saves the average value of the pedestal in every FEM, which will subtract it from the signal. The last script launches an acquisition; data is saved into an .aq5 file which contains the waveform from every pad, and can be converted to a .root file by registering the real position of each pad on the ERAM. I had such a converter and this file is composed of a 3D array of size $32 \times 36 \times 511$, which corresponds to the pad number on z , pad number on y and waveform sampling bin. The data acquisition can be launched in time mode, where I can select how long the acquisition will run, or in data size mode, which sets a maximum size for the output file.

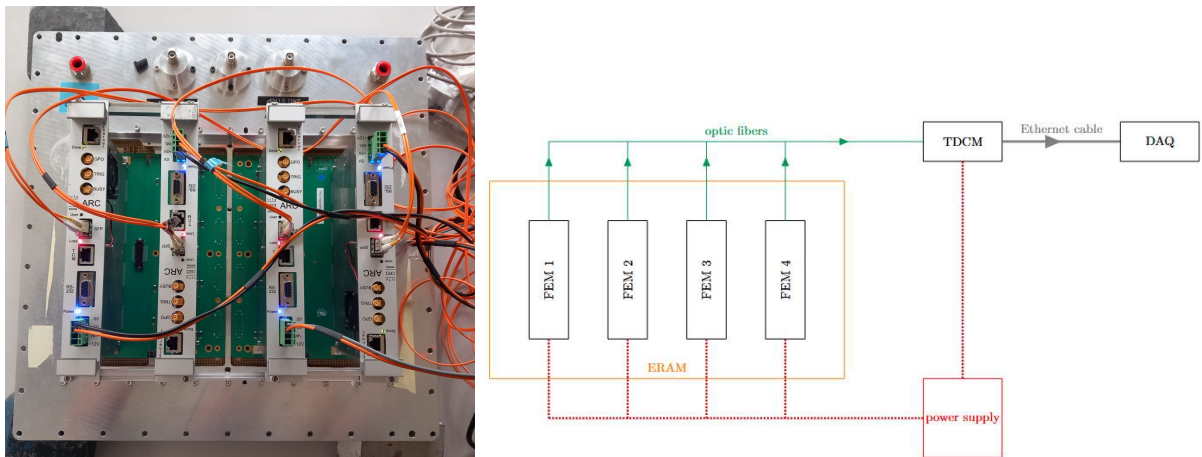


Figure 3.12: On the left the electronics within the frame, while on the right the scheme of the electronics readout chain.

Chapter 4

Laser setup

I started working with the prototype on the creation of a laser system using the quartz window present on the side of the mTPC, checking for the resolution and the laser properties.

Previous laser studies have been performed with one HATPC with FC1 and FC2 [15]. The experimental configuration in that case was with the laser entering the TPC from a quartz window under the ERAM. The angular acceptance was limited to point the laser directly on the cathode; in this way, the main component of the track was the spot produced by the photoelectric effect. Only a limited analysis can be performed with this configuration, and the implementation of the lateral laser in one HATPC (as in my case) is limited by the damage that I would cause to the kapton layer between the strips, as UV lasers heat the kapton and evaporate it. In addition, it is not possible to drill a hole in the HATPC. Due to this, the prototype is the perfect option for these tests because it allows one to recreate real straight tracks and to modify the prototype with more flexibility.

4.1 Laser description

The laser I used was a Minilite Continuum Nd:YAG Class 4 [25]. The available wavelengths are 1064, 532, 355, 266nm from the infrared to the UV spectrum.

The laser is composed of a tower-style power supply and an optical harmonic generator head. The tower power regulates the laser beam frequency and trigger, whereas the laser head regulates and generates the beam.

The external and internal parts of the head are shown in figure 4.1. The dimensions of the head are $267 \times 172 \times 63mm$ and the weight is 3.6kg; considering these aspects, it required a proper movement system. An improvement that can be implemented in future laser runs is the use of an optical fiber: in my case, for example, the head is quite large; if one wants to perform smaller movements or insert it in small cavities, it is limited.

Specifically, the laser head is composed of the Nd:YAG rod, with an internal electrode to initialize the laser. Following the beam, a dichroic of 1064nm placed after the rod deviates the beam by 90°. After the first dichroic, a system of dichroics and crystals is used to change the wavelength from the original 1064nm to 532nm, 355nm, or 266nm, depending on which ones are inserted. The power output is highly dependent on the alignment of the two crystals, and so a fine tuning was necessary: I first used only the wavelength $\lambda = 266nm$.

In the head, an attenuator lever is present so that I could modify the power output from 4% to 100% of the original output. From the head to the power tower, there are 4 cables. One is the high-voltage BNC cable input (that is responsible for the system trigger, connected to the tower to the MARX TRIG output), the others are two water tubes, in which the water flows in opposite directions, and an HV power supply. From the tower controller, I could select two

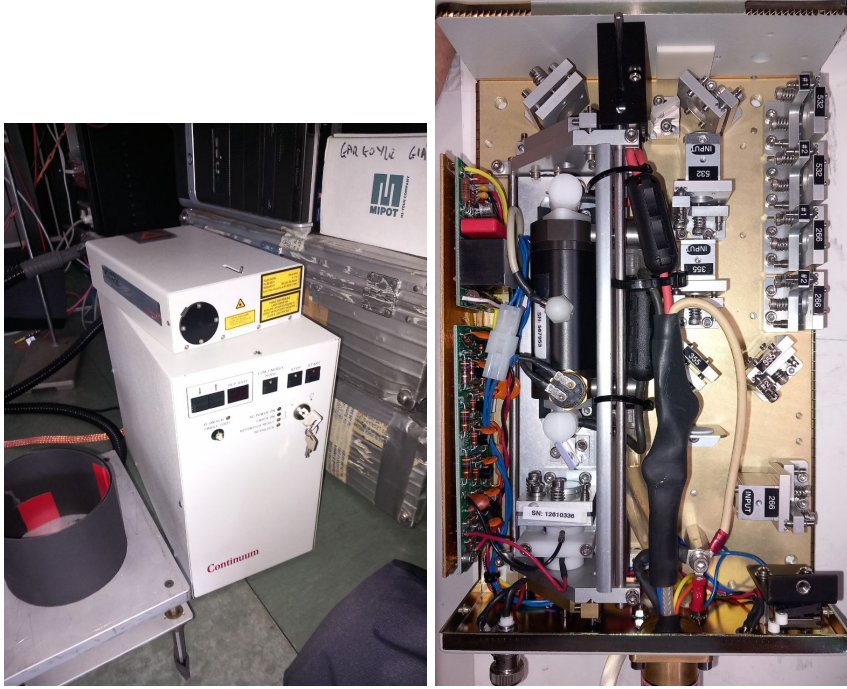


Figure 4.1: On the left the externs of the laser head and the tower, while on the right the interns of the laser head.

intensity options: "high energy mode" or "low energy mode". I used the first one to generate laser tracks, while operating the laser the second one for personal safety. A control frequency panel is present, in which the user can select the REP RATE from $1Hz$ to $15Hz$.

In the back of the tower power supply, I used the Q-switch BNC output for the trigger of the TDCM. This output provides a logical TTL signal. The Q-switch trigger is $15\mu s$ long, and its end is around $60ns$ before the laser peaking time, a period of build-up: such a delay generates a shifting time. There is a second trigger logic called "flashlamp trigger", which indicates the start when the flashlamp, or initializing electrodes, is starting the ND:YAG rod. Next it was necessary to convert the TTL signal to a proper NIM signal and reduce the width to around $50 - 100ns$. This was done using a TTL-NIM module converter level adapter model 688AL in complementary mode [22], and its output is connected to a CAEN dual timer model N93B [11] to generate the correct trigger window for the TDCM.

Specifically, the Q-switching is present because when electrically pulsed, the flashlamp emits light that excites the Nd:YAG gain medium. Just like a capacitor stores electrical energy, the Nd:YAG rod absorbs the optical energy of the flashlamp. Without Q-switching, lasing begins as soon as the gain in the cavity exceeds its losses, resulting in a spontaneous laser pulse that lasts nearly as long as the flashlamp pulse itself. A typical Q-switch setup includes a crystal, a quarter-wave plate, and a horizontal polarizer positioned within the laser cavity between its end mirrors. When the Q-switch is "closed" (meaning no voltage is applied to the crystal), it does not rotate the polarization of light. In this state, light exiting the gain medium is blocked from re-entering the cavity, preventing stimulated emission. This allows the Nd:YAG rod to store more energy before lasing is initiated.

The nominal beam output divergence is $\leq 3mrad$, defined as the full angle at 86% energy (so $\frac{1}{e^2}$ of energy), and the beam diameter is $3mm$. The laser beam has a time length of $5 \pm 2ns$, which is $\approx 1.5m$ in spatial length. The energy stability is reported in table 4.1, with the first value being the peak-to-peak value for 99.9% of pulses, while the second value represents the

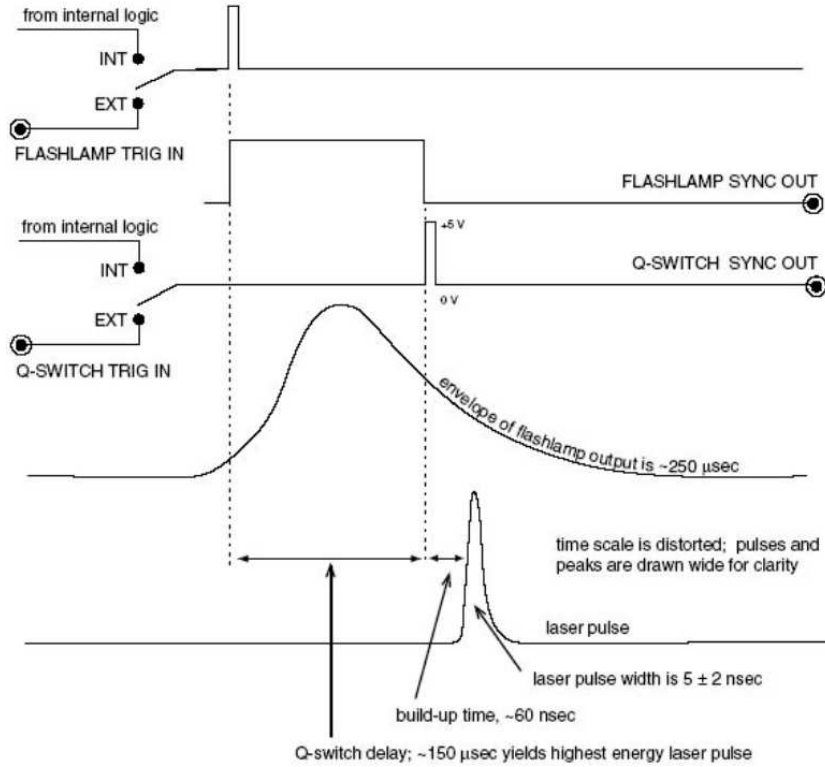


Figure 4.2: The trigger logic scheme from the laser manual. I am triggering in the Q-switch fall time.

RMS. So, for example, in the case of $1064nm$, it means that 99.9% of the peaks are within a 2% range of the energy and with an RMS of 0.5%. What is more important to note is that I selected the wavelength $266nm$ that would generate less divergence but is the most unstable in beam energy.

| Wavelength | Energy Stability ($\pm\%$) |
|------------|------------------------------|
| $1064nm$ | 2.0; 0.6 |
| $532nm$ | 3.0; 1.0 |
| $355nm$ | 4.0; 1.3 |
| $266nm$ | 8.0; 2.6 |

Table 4.1: Energy Stability at different wavelengths.

The nominal beam diameter is $3mm$, which is larger than the expected resolution I wanted to measure and the possible deviations caused by the electric field. To reduce the beam size, I had two collimators $150\mu m$ and $500\mu m$ large in diameter, and two beam squeezers of Edmund Optics $3\times$, for wavelength $266nm$, and $20\times$, for $355nm$ [13]. I first tested the beam squeezers with a class 3 smaller laser, so that it was easier to operate the system. By changing the distance between the squeezer-laser and the squeezer and a paper sheet, I established that the squeezer needed a backup simulation, as I will explain later.

Since the laser is highly dangerous, I first completed the required laser safety courses. The UV range can cause skin damage and burn the cornea, while the infrared range can cause retinal damage. Therefore, all operations with the laser were always performed in compliance with safety protocols, which included wearing personal protective equipment. As part of the setup

preparation, I covered the laser with multiple layers of cloth, especially the back of the laser head, where a reflection occurred due to the transparent water supply tubes

4.2 Double photon ionization

It is important to understand the laser-gas interaction mechanism. For the most energetic wavelength, 266nm , a single photon carries 4.8eV , while the minimum ionizing energy of argon is 15.76eV . The other two components can be considered, but the lowest ionization energy is, of course, for isobutane, which is 10.8eV .

What I observed next is in disagreement with what I expected, as I would have expected no tracks and the experiment to be unfeasible. This is not true because of the double-photon ionization mechanism of impurities. The nominal purity of the T2K gas is, for argon and CF_4 , around 99.999%, while for isobutane is lower, around 99.9%. Looking up at the kind of impurities that the buthane family production introduces in table 4.2, it is possible to notice that all of them are above 4.8eV , but below 9.6eV , which is the energy deposited by two photons. This is the Resonance-Enhanced Multi-Photon Ionization (REMPI), or in my case double-photon ionization, in which two photons hit the same molecule and ionize it [10]. The probability of such phenomena is proportional to the square of the intensity of the laser, and the intensity is proportional to the inverse squared of the beam width. This generated in my chamber an electron deposition that behaved along the track like $\sim 1/r^4$, with r the width of the beam.

| Additive | Ionization Potential (eV) | Ionization (e^-/cm) |
|---|---------------------------|--|
| | | 266 nm, $1 \frac{\mu\text{J}}{\text{mm}^2}$, 10^{-3} Torr |
| Benzene (C_6H_6) | 9.24 | 5×10^3 |
| Toluene (C_7H_8) | 8.82 | 5×10^4 |
| Cumene (C_9H_{12}) | 8.69 | 11×10^4 |
| n-Butylbenzene ($\text{C}_{10}\text{H}_{14}$) | 8.69 | 5×10^4 |
| m-Xylene (C_8H_{10}) | 8.56 | $\leq 4 \times 10^4$ |
| TMA ($(\text{CH}_3)_3\text{N}$) | 8.5 | 60–130 |
| 1,3,5 Mesitylene (C_9H_{12}) | 8.40 | 1.8×10^4 |
| Phenole ($\text{C}_6\text{H}_5\text{OH}$) | 8.3 | ≥ 250 |
| Naphthalene (C_{10}H_8) | 8.12 | 560 |
| TEA ($(\text{CH}_3\text{CH}_2)_3\text{N}$) | 7.5 | 200 |

Table 4.2: Ionization characteristics of various additives under 266nm laser excitation [20].

4.3 Experimental setup and laser tests

It was necessary to perform a data test taking to understand how to proceed. So, first, the laser head was properly covered, and I aligned the laser to the quartz window. I created a movement system to move the laser head by having two perpendicular mechanical micrometers and one mechanical goniometer. The micrometers and goniometer were fixed in position under the laser head as shown in figure 4.3.

Specifically, the possible configuration movements are the following:

- **Vertical:** the vertical movement was along a plane parallel to the ERAM. In this way, I could generate a track in front of the pad in different positions, generating a straight parallel track to the ERAM plane. The movement had a minimum step size resolution of $10\mu\text{m}$.

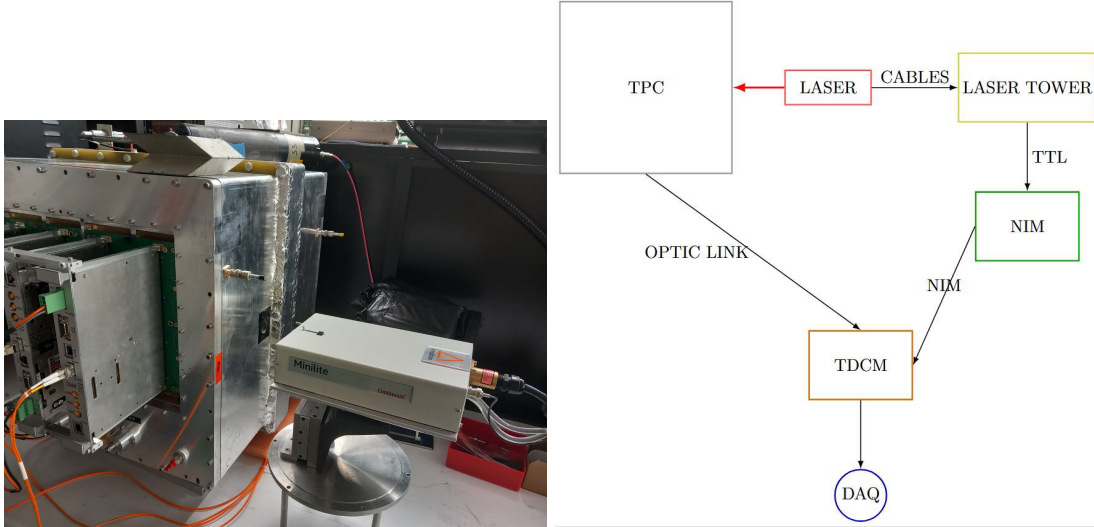


Figure 4.3: The experimental setup with the laser head pointed toward the quartz window on the left, while on the right a scheme of the setup and connections.

- **Horizontal:** the horizontal movement was along the anode-cathode direction. In this way I could perform time measurements. The movement had a minimum step size resolution of $10\mu m$.
- **Angular:** the angular movement was in the plane parallel to the ground. In this way, when fixing the head in position, I could perform an angular scan in the direction of the anode-cathode. The goniometer under the laser head had a step size of $1'$.

I decided to move the laser by steps of $\approx 0.5mm$, because the system was not sufficiently mechanically stable to be moved by steps of $10\mu m$, maintaining repeatability. In addition, initially, I considered that it was not physically relevant since the expected resolution is $300 - 500\mu m$. However, this kind of measurement could be relevant for pad RC and gain characterization under the $100\mu m$ spacing (since it has been carried out using only the ^{55}Fe radioactive source).

In terms of the setup, it is important to underline some problematic points. The first was the limited angular acceptance of the quartz window, where I was practically sending a laser beam in the horizontal direction equal to the segmentation direction. If by chance the laser track generated a signal too low, it could produce charge in only one transverse pad.

The second problem was the precise alignment of the laser. This was not important for the single data measurements, as it is for the resolution. In the case of multiple data taking for different positions of the system, the parallelism between horizontal movement and anode-cathode direction is fundamental. Specifically, if the anode-cathode direction is not parallel to the direction of the micrometer movement, by an angle θ , then reading on the micrometer the distance between two points X , it will in fact be $X \cdot \cos\theta$ from the point of view of the TPC. An estimation of this error can be done by calculating θ such that $490\mu m = 500\mu m \cdot \cos(\theta)$, so that there is an error equal to the resolution of the micrometer. This value is $\theta \approx 11.5^\circ$, and I was well below this value, so there is no need to worry about it. All other directions provide no such error, as measurements will be determined using different step measurements.

After this point, I aligned the system using security laser glasses and small disks of scintillating silicone (a special silicon mixture that allows the user to stick it to a surface and observe the dot generated by its scintillation without causing any eye problems). In this way, in the end, I could move the laser efficiently and easily.

I started testing the electronics and seeing if there was any track, using the $266nm$ wavelength. It has been found that the attenuator modifies visibly the charge deposited in the ERAM, passing from a nearly invisible track to complete saturation of multiple pads. Due to this, every time a measurement was done, I went on to perform a calibration based on the number of illuminated pads. I positioned the laser pulse lever in the region of intensity so that three transverse pads returned a signal. This is important because the clusterization and tracking analysis depend on the number of transverse pads.

With the first data taking, I first created a track plotting in order to visually see what the ERAM collected, which was used for calibration and control throughout all the data taking. The dataset was acquired with a DLC voltage of $340V$, a cathode voltage of $5.77kV$, therefore producing an electric field of $\approx 275V/cm$, with a simple $500\mu m$ collimator.

From the waveforms and via a simple parabolic fit, I could extrapolate its maximum, thus obtaining for each event a 32×36 matrix with its value and the time value that was used to determine the other direction. This is a good indicator for the position and charge deposited. I report such a plot in figure 4.4: the color bar is the **charge**, which I define as the maximum of the waveform. This is done to directly understand the correlation between it and the deposited total charge on the pad, and it will be used throughout this thesis.

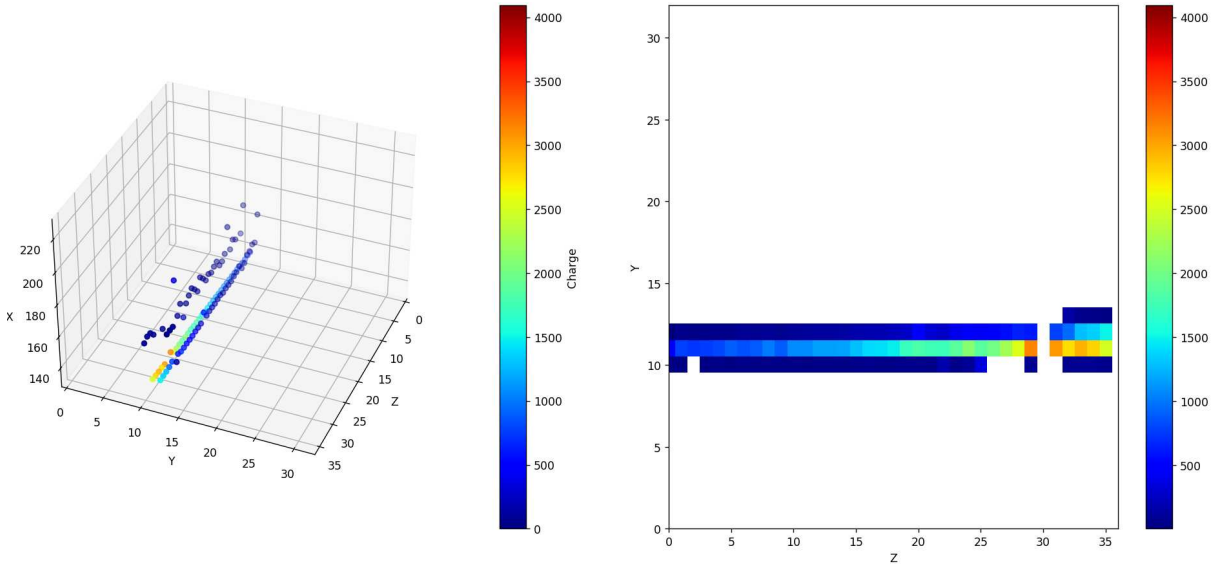


Figure 4.4: On the left a 3D reconstruction of the same event, on the right the laser track with the color of the maximum of the waveform for each pad in 2D (some pads are removed due to an α source noise presence). In Z there is the horizontal pad index, on Y the vertical pad index while on X the time bin ($1bin = 40ns$). On the right figure, the laser enters from right to left.

First of all, in the figure it is possible to notice that the track is not uniform along its path. This can be due to a double effect: the UV absorption by the impurities, and the beam divergence, which decreases the double photon ionization probability.

4.4 Laser simulation

To clearly understand the beam shape, it was necessary to perform a simulation. Using the beam squeezer and by optically coupling it to a collimator, it was not easy to understand how the beam shape and radius would be, and especially how it would change along the beam direction.

Specifically, I used LightPipes for Python [23], which is an open-source library for the simulation of coherent light. It is based on the scalar diffraction theory and uses numerical techniques to propagate optical fields through various components. The library simulates the electric field $E(x, y)$ of a laser beam as it propagates through space and interacts with optical elements. It operates primarily in the paraxial approximation, where the angular deviations from the optical axis are small, allowing simplifications of Maxwell's equations into the scalar form:

$$\nabla_T^2 E - 2ikE_z = 0$$

where ∇_{\perp}^2 is the transverse Laplacian and $k = 2\pi/\lambda$ is the wave number. LightPipes solves this equation numerically using Fresnel diffraction or the angular spectrum method. The only inefficiency present is the grid size, as is the case for all finite element programs.

What I was interested in was the beam spot at a certain distance, from which I could perform a Gaussian fit. This was an approximation of what the beam shape could be like as there could be different interferences, but it was used to understand the width. I had at my disposal the collimators ($150\mu m$, $500\mu m$) in diameter and the Edmund optics beam squeezer $1/3\times$ or inverted $3\times$. It is clear from the known equation $\theta \approx 1.22\frac{\lambda}{d}$ that the divergence is lower for the $266nm$ wavelength. I also performed the calculation with the inverted beam squeezer, because perhaps a $3\times$ on a collimator of $150\mu m$ could produce a smaller spot due to a smaller divergence, since the divergence and magnifying effect are related through a simple equation, *divergence · magnification = constant*, as provided by the producer.

The collimator was simulated using the *CircAperture* function, which was used to simulate a perfect circular aperture. The beam expander was simulated as a two-lenses system with a nominal focal length of $75mm$ and $25mm$, using the Galilean telescope method. By varying the distance between the two lenses, I could obtain different magnifications; this distance is in the range $[95 : 105]mm$.

This initial measurement could be slightly different from that of the real apparatus. I contacted Edmund Optics for more information, but due to copyright limitations, they could not provide precise data about the system.

In figure 4.5 there are all the combinations of the beam spot at $50cm$ from the last optical element (considered the distance at which the mTPC other wall is, opposite to the quartz window). It is easy to see that the smallest spots are in the cases of the $500\mu m$ collimator and the $150\mu m$ collimator with the squeezer $3\times$ (that now is in an expander configuration). Only for these two cases further analysis has been performed.

For these two cases I performed the calculation on the beam width at different distances from the last optical element. As I was near the last optics, the beam could present an interference pattern, as can be seen in figure 4.6.

The beam width parameter is calculated by Gaussian fit of the beam profile to easily correlate it. For the two cases, the beam width as a function of the distance is shown in figure 4.7.

For the plot *distance – σ* I performed a linear fit to estimate the angular divergence. The results are reported in table 4.3. From the optical theory I expected a divergence value of $\theta \approx 1.22 \cdot \frac{\lambda}{D}$ so for $D = 500\mu m \rightarrow \theta \approx 0.65mrad$ and $D = 150\mu m \rightarrow \theta \approx 2.16mrad$, at the $\approx 1\sigma$ level.

| Parameter | $150\mu m + Squeezer$ | $500\mu m$ |
|----------------|-----------------------|-----------------------|
| $m[\mu m/m]$ | 239.02 ± 0.14 | 216.32 ± 0.10 |
| $c[\mu m]$ | -62.25 ± 0.10 | 7.91 ± 0.06 |
| $\theta[mrad]$ | 0.23902 ± 0.00014 | 0.21632 ± 0.00010 |

Table 4.3: Fit results.

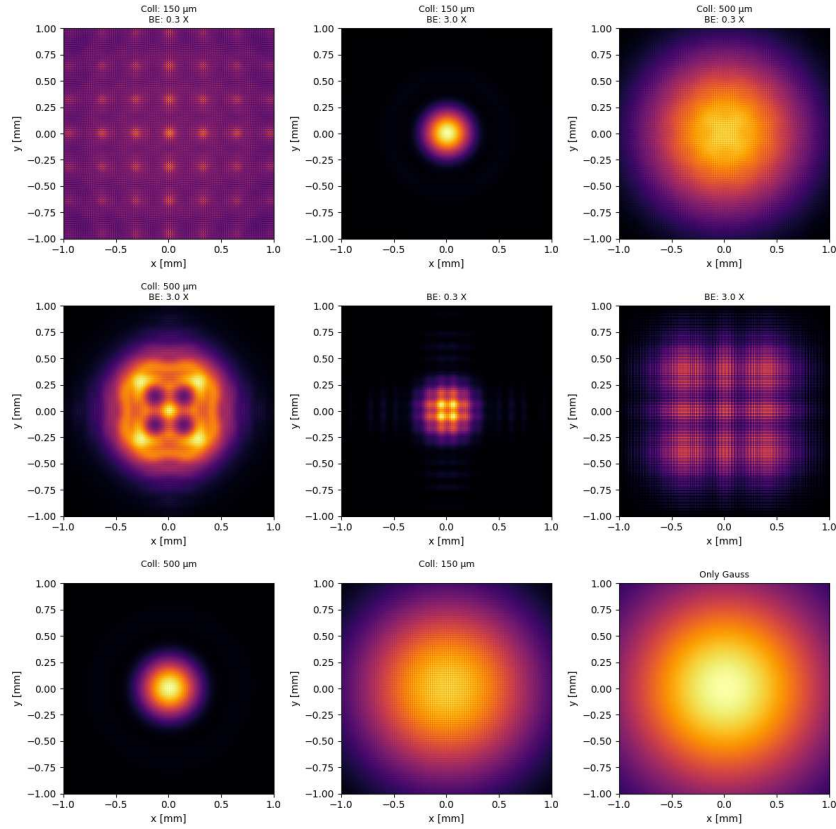


Figure 4.5: Beam spot width at a distance of 50cm from the last optic element using all 9 possible configurations.

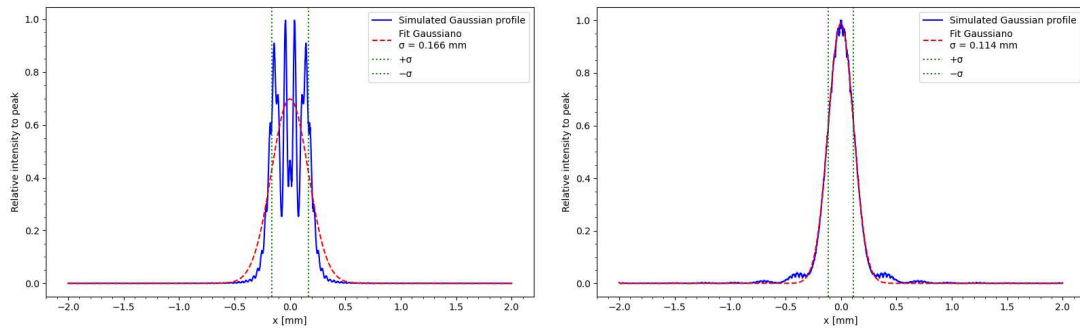


Figure 4.6: Section of the laser beam with the collimator of $500\mu\text{m}$ at 6cm on the left and 50cm on the right from the collimator.

To compare the spot map and determine which was the best, I switched on the laser, positioned a paper sheet at several meters from the laser, and tried all the configurations. Visually, a difference is observable between the case of the collimator $500\mu\text{m}$ and the collimator $150\mu\text{m}$ with the expander $3\times$, with the second having a much tighter spot. As will be seen, the divergence is lower than expected only in this case due to the approximation in the beam squeezer in my simulation. Nevertheless, this simulation was operationally important to determine the best configuration and to better understand the dynamics.

In the end, thanks to this simulation, I generated the best beam possible which has the

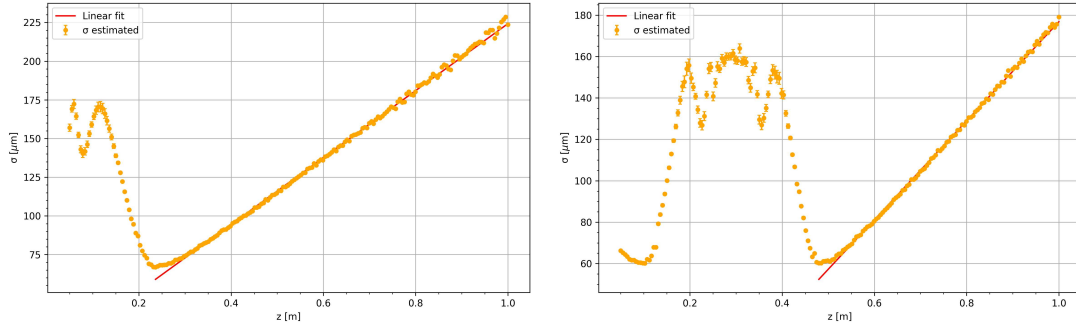


Figure 4.7: On the left, the beam width as a function of the distance with relative linear fit for the configuration with the collimator $500\mu m$, while on the right with the collimator $150\mu m$ and the beam expander $\times 3$.

following characteristics:

- collimator $D = 150\mu m$
- beam squeezer magnification $3\times$
- angular divergence expected $\approx 0.2mrad$ and minimum beam width of $\sigma \approx 60\mu m$

4.5 Gas absorption length and divergence

As mentioned before, the intensity along the track looked diminishing.

I assumed my track to be perfectly horizontal; in this way, I could reduce the analysis by two pieces. I summed over all events the maximum of the waveform for the central pad along the line: in this way, gain differences due to the gas properties effect variations over time were reduced. Only the primary pad was considered, because summing over all the cluster charge would introduce non-defined biases. In addition, I had the gain map for all the pads measured at the production level using a ^{55}Fe source. I normalized all values for the gain value.

These two calculations were the most important points because if I collected a data set and tried to perform an energy laser loss for each event, the gas gain would be modified and so the differences in charge between two pads. In addition, the beam intensity varied: as said before, at $266nm$ I had 99.9% of all beams inside an energy range of 8.0%. At this point, I had a scatter plot with the distance of the central pad considered along the beam direction (in the approximation of the horizontal beam) called z , and the sum of the maximum for all the waveforms.

The theoretical models to fit are the following:

- For the absorption the model is given by the exponential loss $I(z) = A \cdot \exp\left(-\frac{|z-z_0|}{\lambda}\right)$, where λ is the attenuation length and z_0 is the first gas-laser impact position. This value has been fixed to $z_0 = 40cm$.
- In the case where only divergence is responsible for the effect, the probability of interaction is proportional to the square of the intensity, mathematically I have to fit $f(z) = \frac{A}{(m|z-z_0|+q)^4}$ where q is the initial beam width at $40cm$ (in an unspecified unit of measurement, because I am not calculating the fit over the intensity but an ADC value) and m is related to the divergence by $m = \tan(\theta)$.

- In the case where both contribute in the same way, then the fit is simply $f(z) = \frac{A \cdot \exp\left(-\frac{|z-z_0|}{\lambda}\right)}{(m|z-z_0|+q)^4}$.

The fits are plotted in figure 4.8, while the fit results are in table 4.4. The data used were collected with the collimator with diameter $500\mu m$. The data collected, as can be seen, were not optimal for this analysis, because the TPC was not created to perform this kind of measurements. However, I could understand that the data are in agreement with the expected angular divergence $0.21632 \pm 0.00010 mrad$, because I was using the $500\mu m$ collimator, if I considered no absorption. In addition, it is unlikely that 0.01% impurities in 2% of isobutane were responsible for a beam reduction to $\approx 25\%$ of its initial value.

I concluded that in this way I could directly measure the beam divergence as the diminishing effect depends only on it, because the λ in fit 3 is of the order of kms .

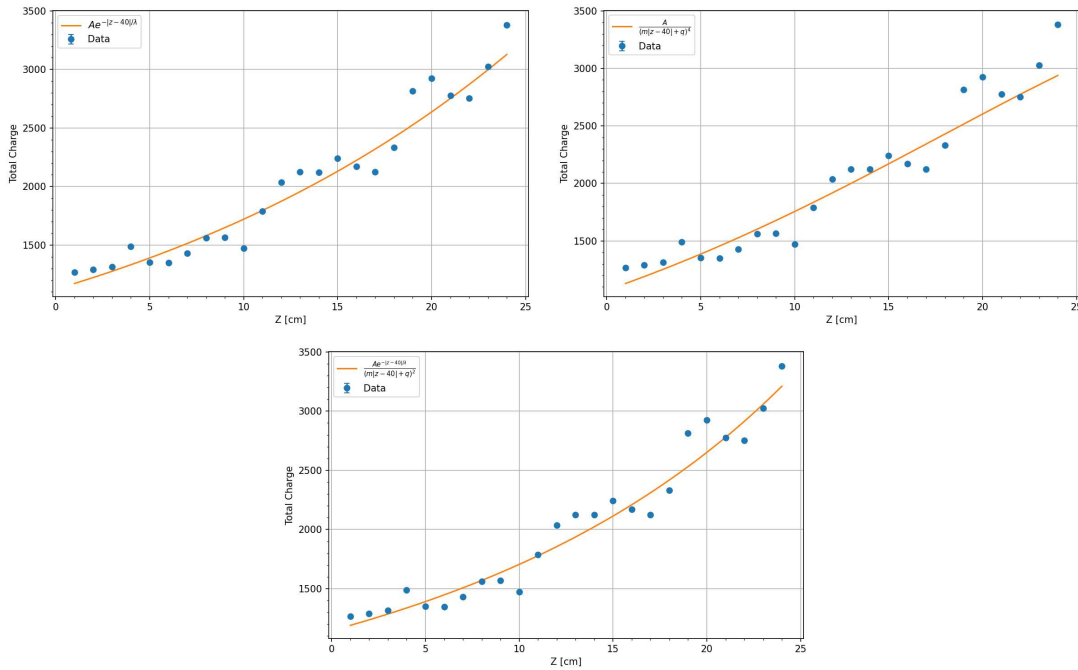


Figure 4.8: Gas absorption and divergence fit.

| Fit | $\lambda[cm]$ | m | χ^2 |
|---|-------------------------------|------------------------------------|----------|
| Fit 1: $Ae^{-\frac{ z-40 }{\lambda}}$ | 23.426 ± 0.052 | — | 538.46 |
| Fit 2: $\frac{A}{(m z-40 +q)^4}$ | — | $(2.214 \pm 64.73) \times 10^{-4}$ | 722.79 |
| Fit 3: $\frac{Ae^{-\frac{ z-40 }{\lambda}}}{(m z-40 +q)^4}$ | $(1.05 \pm 0.06) \times 10^8$ | $(1.44 \pm 261.0) \times 10^{-2}$ | 489.87 |

Table 4.4: Fit parameters λ , m , and χ^2 values for the three models.

I performed the same analysis with a data set using the $150\mu m$ collimator and the beam expander, which is my preferred and final configuration. The result yields a beam divergence of $0.12 mrad$, two times lower than expected from the simulation. The ratio between the qs in the case with only the $500\mu m$ collimator and the $150\mu m + expander$ is $R \approx 1.044$. This provided a more faithful characterization of the beam with the expander. The beam width, in the first case, was nearly exactly as in the case with only the collimator. Then I could assume that the initial width σ is around $60\mu m$ with a divergence of $0.12 mrad$. I got a beam spot at $50cm$ of $\approx 85\mu m$, better than expected.

4.6 α source activity

Attached to the cathode there was an ^{241}Am source that emits α particles with an energy of 5.486MeV , with an activity of 3.7kHz . Due to this I had persistent noise producing a spot-like source. The laser track passes nearly at the center of the source and generates a double effect

- deformations of the waveform due to high electron density in the DLC
- track deformations due to a charge accumulation effect
- pattern recognition noise, only if in temporal coincidence

I subsequently removed the source to increase the DLC voltage. This was necessary because, at 350V , the track using the $150\mu\text{m}$ collimator and the expander was only activating a single pad, with no secondary pad being detected.

4.7 Waveform analysis

The goal was to analyze the waveform data stored in ROOT files and extract physically meaningful features, such as signal amplitude, timing, and shape descriptors. This analysis was performed by fitting a skewed Gaussian model to each waveform from the 36×32 pad detector, which has 510 time samples per pad. This method was selected as the initial approach because it is currently used in the HATPC analysis framework. The objective was to use this method to determine the beam spot size.

The waveform from each pad was modeled using a skewed Gaussian function defined as

$$f(x) = A \cdot \exp\left(-\frac{(x - \mu)^2}{2\sigma^2}\right) \cdot \left(1 + \operatorname{erf}\left(\frac{\alpha(x - \mu)}{\sqrt{2}\sigma}\right)\right) + \text{shift}$$

where

- A is the Gaussian amplitude. Condition: $A > 50$.
- μ is the peak time. Condition: μ within the fitting window.
- σ is the standard deviation. Condition: $\sigma \in [0.5, 50]$.
- α controls the skewness. Condition: $\alpha > 0.001$.
- shift is the baseline offset. Condition: $\text{shift} \in [150, 350]$.

The most important parameters are the amplitude of the waveform above the pedestal and the peaking time. The maximum amplitude was calculated through numerical evaluation as it is different from A . For all parameters I determined the error, using error propagation. At the end I had a data set much more suitable to work with, that could be used for subsequent physics analysis or visualization. The main problem encountered in this initial filtering of the data was the presence of the α tracks that produced a random peak that could overlap totally or only partially with the laser waveform.

I also checked for all the 5 parameters and their errors, to see if there was any anomaly. First I plotted the histograms, and I found a correlation between the maximum amplitude and the peaking time error. This is due to the specific fit function that I was using; physics experiments do not use the peaking time but, for example, the constant fraction discrimination method.

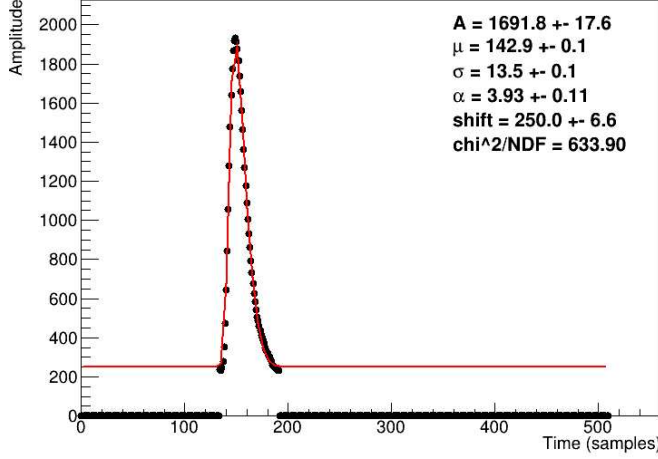


Figure 4.9: Example of waveform I collected with relative fit for a good laser signal.

To improve the time resolution, then, instead of performing a fit using the skewed Gaussian fit I used its derivative

$$\frac{df}{dx} = A \cdot \exp\left(-\frac{(x-\mu)^2}{2\sigma^2}\right) \left[-\frac{x-\mu}{\sigma^2} \left(1 + \operatorname{erf}\left(\alpha \frac{x-\mu}{\sqrt{2}\sigma}\right)\right) + \frac{2}{\sqrt{\pi}} \cdot \frac{\alpha}{\sqrt{2}\sigma} \cdot \exp\left(-\left(\alpha \frac{x-\mu}{\sqrt{2}\sigma}\right)^2\right) \right]$$

The curve was then fitted with the numerically calculated derivative as $D[i] = \text{Waveform}[i+1] - \text{Waveform}[i]$ (as the time steps are constant). All the points of the waveform that saturated the pad would return $D = 0$ and thus were removed. What I expected was a reduction in the time parameter error. This was not the case as the resolution stayed nearly the same.

4.8 Preliminary analysis and configuration tests

I analyzed the tracks of a single test with the collimator of $500\mu\text{m}$ and in a single position. The TPC's cathode voltage was 5.77kV corresponding to an electric field of 275V/cm , the DLC was set at 340V , lower than what the T2K experiment required. This was done because the current in the DLC would be too high; in any case, the resolution did not vary much with this voltage, but in the next step, removing the α was the better choice.

First of all, I implemented a tracking algorithm based on the initial center of charge method and clustering. It is important to understand that tracks are horizontal so the calculations can be simplified. In the ERAM 2D plane, the primary pad is defined for each column as the pad with the highest charge deposition, and was used for the time information of the track. Then the two or one neighboring vertical pads were weighted to determine the track vertical distance from the pad center $dy = \frac{Q_1 - Q_2}{Q_1 + Q_2} \cdot \text{height}$, while for the other direction the pad center position was considered, to generate my 2D points in the ERAM.

After the clusterization, two linear fits were performed to determine the 3D line, one in the ERAM plane and the other in the time plane (I chose one direction in the ERAM plane, the horizontal). For each fit I then got the two line parameters with their relative error and all the fitted points. The outliers were removed based on the 3σ level, as they were all due to the α noise.

The simple spot calculation can be performed by plotting a 2D histogram with the intercept

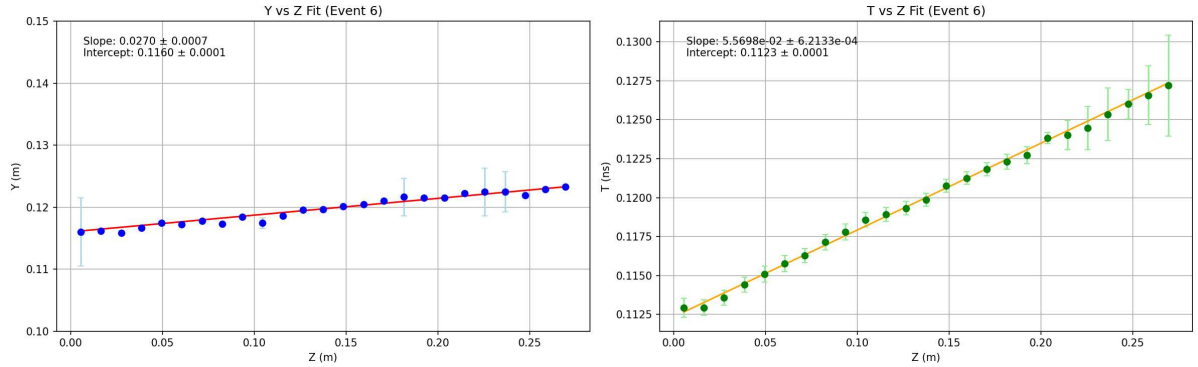


Figure 4.10: Example of linear fit in the ERAM plane (YZ) and the temporal plane seen from above the TPC (ZT), the distance in the temporal direction has been calculated assuming a drift velocity value of $7.8 \frac{cm}{\mu s}$.

values of the two fits. From a 2D Gaussian fit

$$f(x, y) = A \exp \left(- \left[\frac{(x - x_0)^2}{2\sigma_{YZ}^2} + \frac{(y - y_0)^2}{2\sigma_{ZT}^2} \right] \right)$$

I obtained σ_{ERAM} and σ_{Time} that are, at first approximation, the resolution on the ERAM plane and the resolution along the drift direction. The fact that it is an initial approximation is due to the fact that I needed, for the time resolution to align the laser; otherwise, the beam spot would be deformed. In the resolution there is in quadrature the physical beam spot size.

I report in table 4.5 the fit parameters for the plot in figure 4.11. The ERAM resolution in-quadrature with the maximum beam width is $357 \pm 4 \mu m$, while the resolution in the time direction is $0.952 \pm 0.010 mm$, which is $\approx 15 ns$, assuming $v_d = 7.8 \frac{cm}{\mu s}$.

| Parameter | Value |
|------------------------------------|-------------------------|
| Mean P_0 in yz [m] | 0.116096 ± 0.000004 |
| Mean P_0 in tz [m] | 0.113787 ± 0.000010 |
| Std. dev. P_0 in yz [m] | 0.000357 ± 0.000004 |
| Std. dev. P_0 in tz [m] | 0.000952 ± 0.000010 |
| Correlation coefficient (ρ) | -0.052 ± 0.015 |
| Amplitude (A) | 79.0 ± 0.8 |

Table 4.5: 2D Gaussian fit results.

This first test helped me understand that the resolution was around the expected value, with the center of charge method.

The residuals from the linear fit revealed deviations near the bordering pads, as well as near the α source, as expected. These deformations must be corrected to properly determine the resolution; currently, the track is not linear, making a linear fit inappropriate. In the next analysis, I will need to remove all edge points near the chamber walls.

During the analysis, I attempted to improve the time resolution by using parameters such as the initial time of the waveform, but this was not possible. The limitation comes from the intrinsic noise resolution of my laser setup, which is dominated by the triggering system, rather than the intrinsic ERAM time resolution. This overall resolution represents the quadrature sum of the time resolutions from each electronic component (NIM, TTL converter, TDCM, laser tower, and LEMO cables).

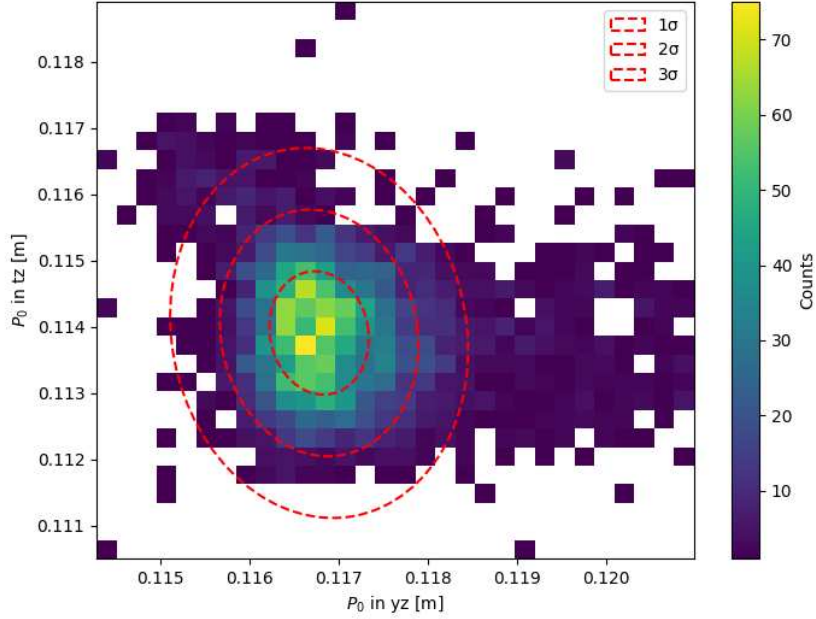


Figure 4.11: Beam spot in the plane $Z = 0$, which is the plane passing through the center of the first pad from the left (of the ERAM) and perpendicular to the ERAM plane. This is the beam spot at the other side of the wall from the quartz window.

4.9 Drift velocity parameterization

Using the Garfield++ simulation software [17], I could generate a comprehensive gas table that defined all the relevant gas parameters, which include the drift velocity as a function of the electric field. This was performed by the Magboltz subprogram [8] by simulating the microscopic transport of electrons in gas mixtures and solving the Boltzmann transport equation. It takes into account the electron collision cross-sections with the gas molecules to calculate electron transport properties under various electric and magnetic field conditions. The gas table was generated at 1 atm and 20° , with a range from $0 \frac{\text{V}}{\text{cm}}$ to $550 \frac{\text{V}}{\text{cm}}$ for a step size of $27.5 \frac{\text{V}}{\text{cm}}$, both for isobutane and nbutane; with the first, a finer range was used of $100 \frac{\text{V}}{\text{cm}}$ to $400 \frac{\text{V}}{\text{cm}}$, with steps $0.1 \frac{\text{V}}{\text{cm}}$.

For all the three sets, the drift velocity is fitted with the parametrized function [27]:

$$v_d(E) = (a + bE) e^{-cE} + d$$

obtaining the results in table 4.6. In this way I had a parametric formula for the drift velocity that was more precise and more efficient than only a point separation. In figure 4.12 I plotted the three datasets, and it is clear that the analytic function is a good approximation for the points around the peak, but worse for values lower or higher than it.

4.10 Final configuration and data taking

As previously mentioned, the α source had limitations that prevented the laser track from inducing sufficient charge to detect its spread in the resistive layer. To overcome this issue, I

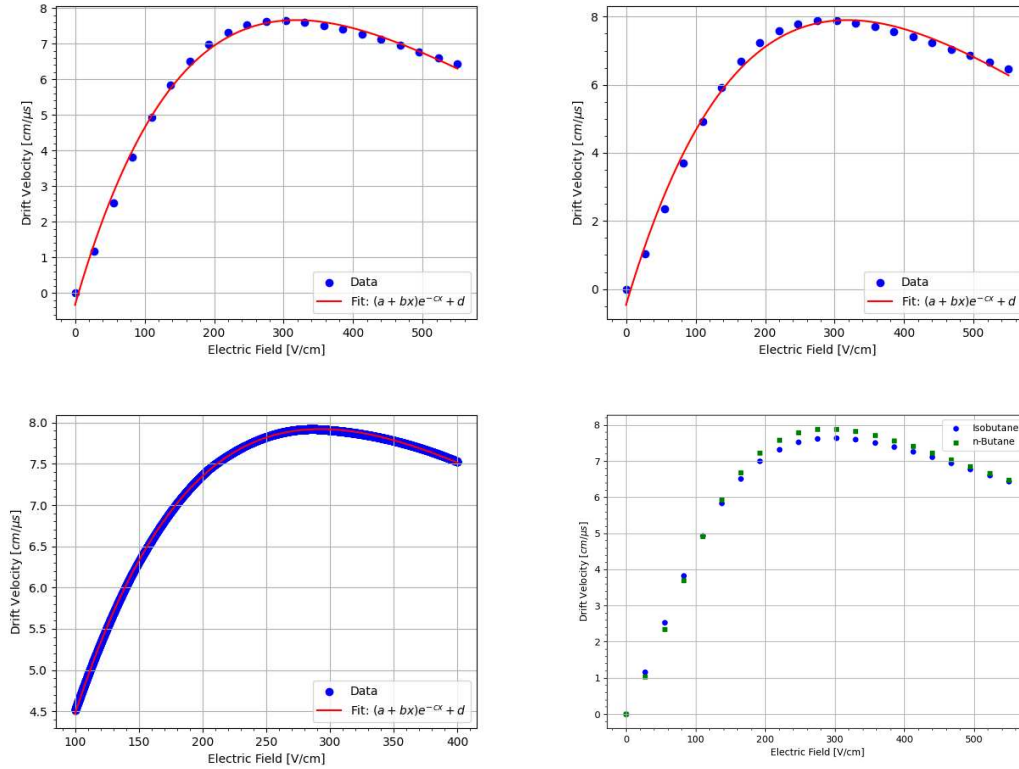


Figure 4.12: The drift velocity curves with their relative fit, the bottom right is the confrontation between n and isobutane.

| Gas | $a[\frac{cm}{\mu s}]$ | $b[\frac{cm^2}{V \cdot \mu s}]$ | $c[\frac{cm}{V}]$ | $d[\frac{cm}{\mu s}]$ |
|--------------------------------------|-----------------------|---------------------------------|-------------------------|-----------------------|
| Isobutane | 0.6 ± 2.2 | 0.070 ± 0.004 | 0.0031 ± 0.0003 | -0.9 ± 2.1 |
| n-Butane | 3.9 ± 4.3 | 0.079 ± 0.007 | 0.0027 ± 0.0004 | -4.3 ± 4.2 |
| Isobutane $[100 - 400] \frac{V}{cm}$ | -6.98 ± 0.03 | 0.08350 ± 0.00005 | 0.004792 ± 0.000009 | 3.62 ± 0.02 |

Table 4.6: Drift velocity fits and parametrization results.

needed to increase the DLC voltage. This procedure required opening the chamber to remove the α source. Once the chamber was open, I also took the opportunity to implement further modifications.

First of all, I opened the chamber by removing all the electronics, the frames, and screws. The aluminum tape at the intersection between the two chambers was removed and not re-taped later, because the effect should be minimal and, practically, it was time-consuming.

The most delicate part was removing the ERAM: it was exposed to the environment and the frame was removed from the TPC. In the T2K HATPCs this procedure was different, and the ERAM was installed after mounting the frame, but due to the small dimensions of the mTPC I had to mount the ERAM and the frame at the same time. This could cause some problems, as some dust could fall on the MICROMEAS while the frame was being screwed in or while it was being removed. In addition, during this operation, I noticed the presence of liquid between the ERAM frame and the ERAM stiffener: this was probably due to the condensation of isobutane.

The modifications performed to the TPC are listed below.

- **Mirror:** A movable mirror was mounted to the opposite side of the chamber, allowing

the laser to reflect off its surface and produce diagonal tracks without requiring additional holes or the repositioning of the laser head. As illustrated in figure 4.13, the system consists of three plastic arms screwed into the back of the mirror mounting, which is also made of plastic. These three arms could be extended inside the chamber and thus inclining the mirror, the maximum angle is around 45° from the normal. The three holes in the G10 wall were produced using a vertical drill press to make them as vertical as possible. It was time demanding and physically difficult because the walls are 4cm of G10, but it was an important step, otherwise the angular acceptance would be diminished. The G10 holes in the last centimeter before entering the chamber has a smaller diameter, so the strips were not damaged. The mirror has a conductive reflective surface, that will modify the electric field, later on I will try to quantify the effect. To preserve gas containment while enabling movement, a tightening screw was located externally: this mechanism allowed the mirror plane to be adjusted to various angles without the need for a motorized system (and especially with minimum gas contamination). All the screws were wrapped in a teflon layer. While moving the arms the gas was fluxed at maximum rate.

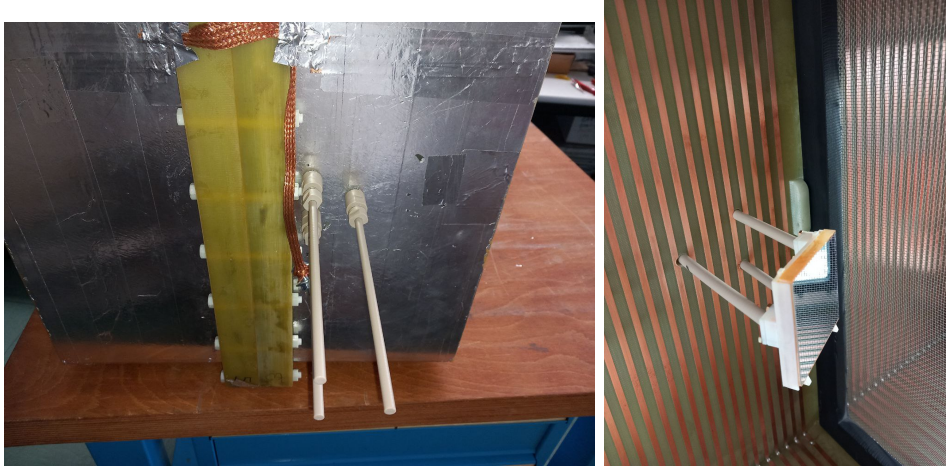


Figure 4.13: On the left from the outside, while on the right the support mechanism from the inside of the chamber.

- **Quartz window:** Only one side of the chamber was instrumented, so a quartz window of size $\approx 25\text{cm} \times 30\text{cm}$ was installed in the other frame. The mounting system is the same as the ERAM. The frame system is composed by the metallic frame, the rectangular quartz window and a plastic frame. There is an additional O-ring between the plastic that maintained in position the quartz window and the quartz window: in this way it can be removed or changed, but it stays in position. Using the quartz window I was be able to point the laser in a larger region. It was also tested by directly hitting the ERAM, with caution, considering that the laser can cause layer evaporation. In figure 4.14 it is possible to see the chamber from the outside with the window.
- **Grid cathode:** Now, if there is the window on the other frame it would be interesting to point the laser from it in the other section of the chamber. This is possible only if the cathode is not completely opaque. To maintain the rigidity of the cathode and the correct voltage, a grid of inox was attached to plastic holed frame with the same mounting screws of the cathode. The plastic frame was created by water-jet cutting; this required then to sandpaper all the angles (so that later the mesh would not be damaged by the angles) and to clean the frame (the mesh, in particular, was cleaned hole by hole, taking up much

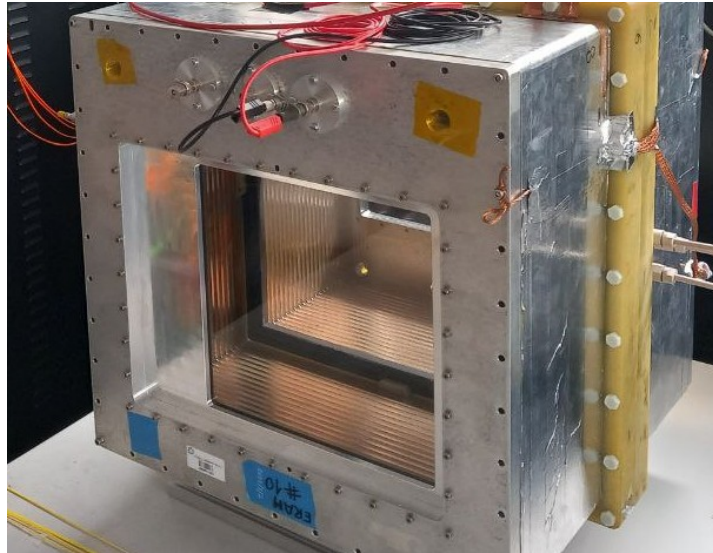


Figure 4.14: The installed frame with the quartz window and the strips inside visible.

time). It can be seen in figure 4.15 that the grid was glued directly to the plastic frame and corona effect points are leveled. The procedure was performed as follows: first the mesh was stretched and fixed in position using heavy blocks in a table with a mylar layer, so the glue could not stick. Then the frame was positioned on top with the glue on the bottom side. After a day the glue solidified, but the angles of the mesh were still present, because it was larger than the frame, due to how I stretched it. The angles were cut using a Dremel multiuse tool to cut the mesh and part of the glue, then on the edges another layer of glue closed the possible mesh exposed. The final result was a well produced mesh with all the edges covered by the epoxy glue to avoid corona effect and such that it was maximally stretched.



Figure 4.15: The transparent cathode inside the chamber.

- **Resistance:** An additional external resistive bridge was created to test the change in the electric field due to the missing resistance between the first strip and the cathode. The distance between the middle of the first strip and the new cathode surface is 2.3cm , while the strip pitch is 10mm , so the resistance must be $2.3\times$ the one between the two strips. This can be obtained by using two in series resistances and two in parallel, as the ones inside the chamber [36]. The resistive bridge was immersed in epoxy glue, as in figure 4.16. A cable was then soldered to the first strip and to the resistive bridge, so from the outside it was possible to change between using the resistive bridge and not using it. It was only necessary to solder the pink SHV cable (in the left in figure) if I wanted to use the bridge, or to the cathode feedthrough if I did not want it. The red cable in figure is the HV to the cathode feedthrough.

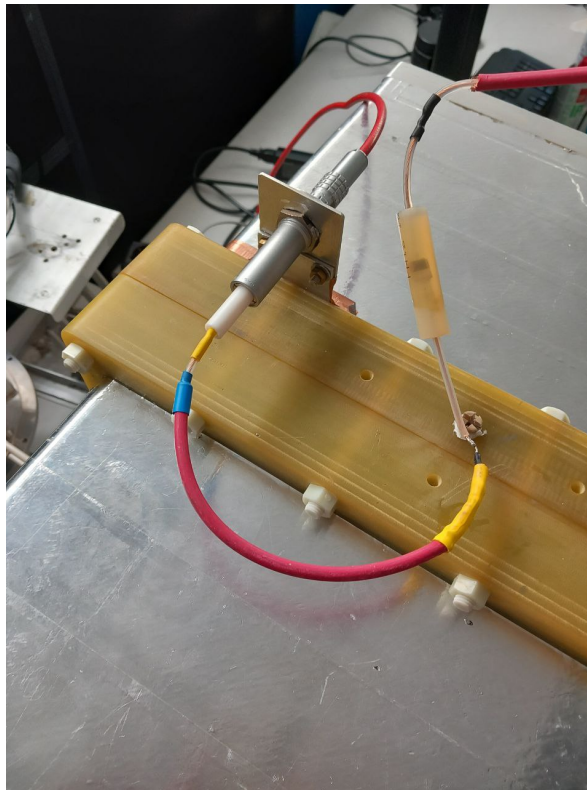


Figure 4.16: The external resistance connected from the cathode to the first strip.

- **Filament:** A filament of a housing lightbulb was attached near the cathode. As the filament gets hotter, it will release electrons in the chamber. Then using an analog current analyzer it is possible to determine some properties on the gas composition and behavior. The filament is connected to two flanges, one for the input and the other for the output current. From the outside an isolating transformer was used to make it work.

During all this procedure, and also at the end, the chamber was deeply cleaned to remove all the dust from the manufacturing process, but also from the environmental contamination.

In the end, I had the apparatus setup as shown in figure 4.18. From the right, the laser can enter the chamber and hit the mirror, but it can also enter from the quartz window and hit the mTPC walls, the ERAM directly, or the mirror.

At this point, some tests were necessary. First, I tested the mTPC electric system because, given all of the changes, something could be different. Then, the movements of the mirror and the



Figure 4.17: The filament attached to the mounting pin of the cathode.

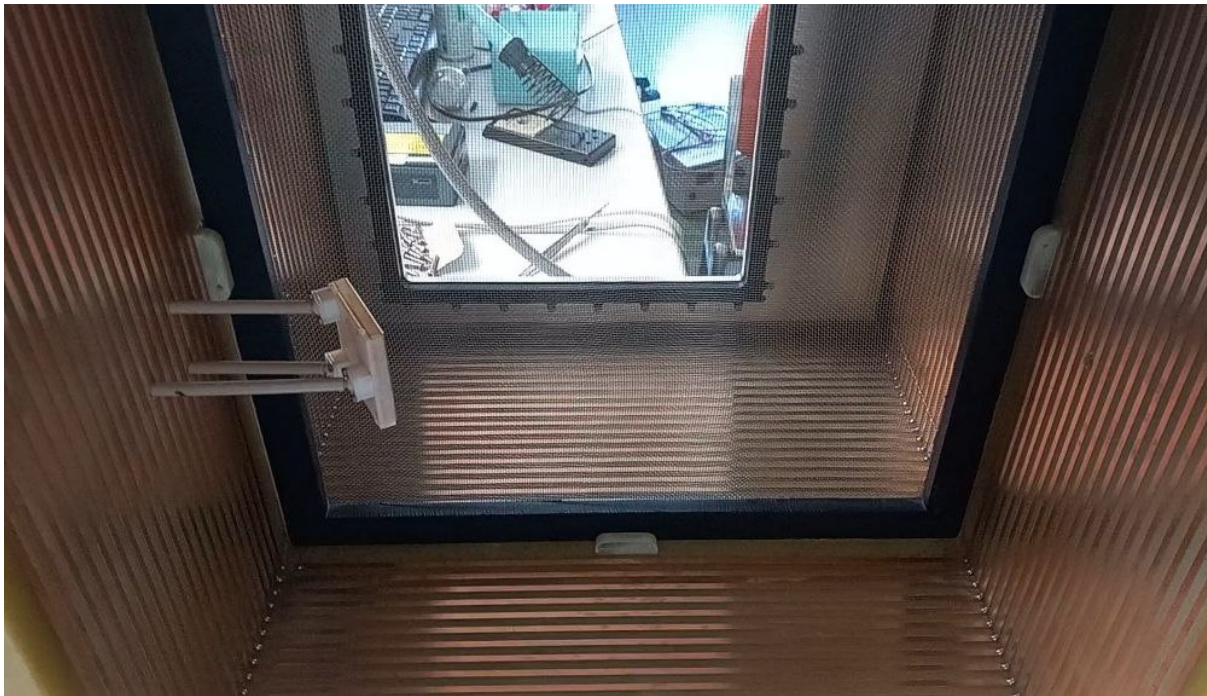


Figure 4.18: A photo of the inside of the chamber from the ERAM side of the TPC, with the mirror, the cathode and the quartz window.

laser positioning. Then, I fluxed argon to check for possible sparks, due to charge accumulation in the dielectric materials; no problem was present. At the end, I started taking data, as all was working properly.

Chapter 5

Laser studies

This chapter presents an analysis of the various data sets collected. The main objectives of these preliminary studies were threefold:

1. To characterize the electric field distortions caused by the mirror introduced near the fiducial volume.
2. To study the distortion effects on particle tracks resulting from modifications to the electric field, achieved by varying the potential difference between the cathode and the first strip.
3. To investigate the signal formation for tracks almost perpendicular to the anode plane, where long segments of the track pile up within the same pad, and photo ionization happen also in the multiplication gap on the ERAM.

5.1 Laser tracks and mirror reflections

An example of the tracks generated by the laser beam and its reflection is shown in figure 5.1.

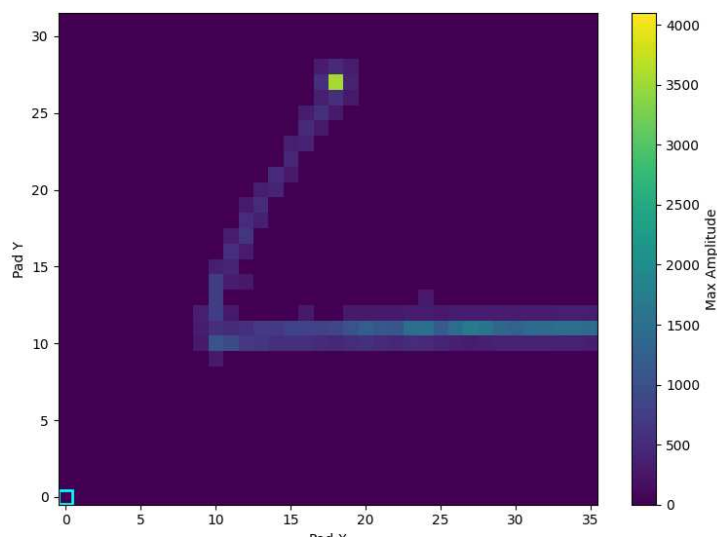


Figure 5.1: Example of an event, the laser enters from the right through the small quartz window, hit the mirror and then crosses the cathode to the other side of the chamber.

With the mirror I have vast possibilities of optical effects. The first one is internal refraction. As it is possible to see from figure 5.2, on the left I have the bottom track but also one slightly

above; this is the first refraction. The second one is present on the bottom pads; this event hits again the cathode. These events generate less charge but nonetheless are present if the laser hits the mirror nearly at the edges. In my case, it is simple to eliminate the pads and incline the laser to avoid the edges. In some cases the refraction was harder to remove, especially the cathode spot provided by this second track.

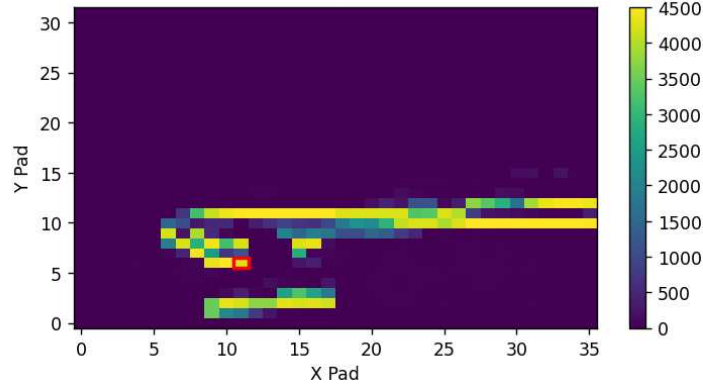


Figure 5.2: The number map with the active pad and events each one registers, for the pads hit by the refraction the charge deposited is much less and not visible in a colormap.

First I moved my laser by steps of $500\mu m$ along the anode-cathode direction.

5.2 Drift velocity measurements for horizontal and vertical scan

For the horizontal scan I used the time information to determine the drift velocity in this specific direction, and as supposed by the setup I would expect a value near $7.8 \frac{cm}{\mu s}$. The laser base was parallel to the TPC wall in which there was the quartz window, but the laser beam was not parallel to the ERAM plane. However, this is not relevant as the important part is to move in the anode-cathode direction with the same step size as the micrometer, otherwise an angular bias is present. To perform the analysis, the secondary pads are not important, only the primary ones. I collected data sets with the collimator $500\mu m$, at a cathode voltage of $5.77kV$.

Being my laser stationary for each data set, I determined the peaking time for each waveform t_{peak} . I created for each pad the histogram and via Gaussian fit I determined (μ, σ) for each pad, only these couple of values were used. For each pad a linear fit was performed with, on the x-axis, the μ value, and on the y-axis, the position on the micrometer. In this way I had the drift velocity (the slope) for each pad with its error, as shown in figure 5.3.

In figure 5.3 it is possible to see the velocity for the horizontal pads in the vertical position $pad_{vertical} = 11$ (that are the primary pad, my laser was horizontal). It is possible to notice how the drift velocity increases slightly near the edges. Unfortunately the resolution is not as good as in the case when using cosmic muons crossing the cathode or pointing directly the laser on the cathode. This is due primarily to the time resolution, at $7.8 \frac{cm}{\mu s}$ produces a spatial resolution of $\approx 1mm$, while I am moving the laser by $500\mu m$ steps.

I then asked myself if it was possible to perform the same analysis but with a vertical scan, in order to determine the electric field deformation induced by the vertical component on the field which would slow down or accelerate the electrons.

This analysis has not been successful because the time resolution is too low to match my linear model in the *space – time* plot, to obtain the velocity. All the results yield a drift velocity compatible to zero.

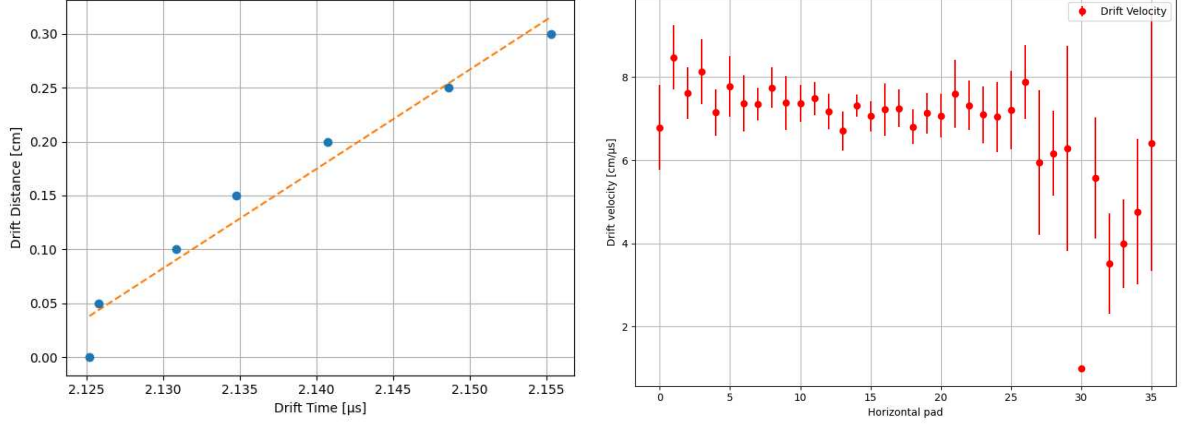


Figure 5.3: On the left an example of linear fit, while on the right the drift velocity plot as a function of the pad number, the right part is compromised by the α source.

5.3 Drift velocity near the mirror

I wanted to determine the effect of the mirror on the drift velocity. As is obvious, the metallic reflective base of the mirror will generate an additional electric field that in the end can deform my tracks. To characterize this effect, I only used the drift time.

I collected data for different mirror angles. So the laser enters from the small quartz window and hit the mirror.

Similarly to what I did before calculating the drift time for the primary pads, for each data set I am able to reconstruct an "average time path" as plotted in figure 5.4. The points are determined by taking the Gaussian fit of the histogram of the parameter t_0 from the fit with my analytical formula $y(t) = \text{scale} \times \text{step}(t - t_0, \tau_r) \times \text{env}(t - t_0, \tau_d) \times \cos(2\pi f(t - t_0) + \phi)$, (that will be explained in the next chapter).

From a visual analysis, there looks to be small deformations. I tried to zoom in on the region where the mirror is and obtain a tighter color plot, but this did not help understand the effect.

From the μ and σ from the Gaussian fit I tried to estimate the effect. I selected the primary pad for all the angular data sets and used the first laser beam, so not the one reflected. The resulting profile of selected mean values is fitted with a parabola of the form

$$\mu(x) = a(x - x_0)^2 + b,$$

where x_0 is the reference vertex of the parabola. The parabola has center $x_0 = 17.5\text{cm}$ and accounts for the TPC electric field disuniformity; they must be symmetric around the center. The residual difference between the measured μ values and the fitted parabola is calculated to evaluate the quality of the fit and identify any systematic deviations.

In figure 5.5 it is possible to see the one-dimensional profile of selected μ values along the horizontal direction (the error bar is the value of σ and not the error in μ , I want to show that the data are outside the 1σ range near the mirror). In the top there is the parabolic fit while on the bottom the residuals, running this program for different data sets the result is similar. It looks like the mirror is inducing a maximum deviation of 200ns (left points are nearer the mirror). For different data sets the delay is $\approx 100/150/200\text{ns}$, depending on the angle, as I am hitting a different position in the mirror.

If I assume an initial velocity of $v = 7.8\text{ cm}/\mu\text{s}$ with a delay $\Delta t = 100\text{ ns}$, for a fixed distance d , the relationship between velocity, distance, and time is $v = \frac{d}{t} \Rightarrow t = \frac{d}{v}$ and after

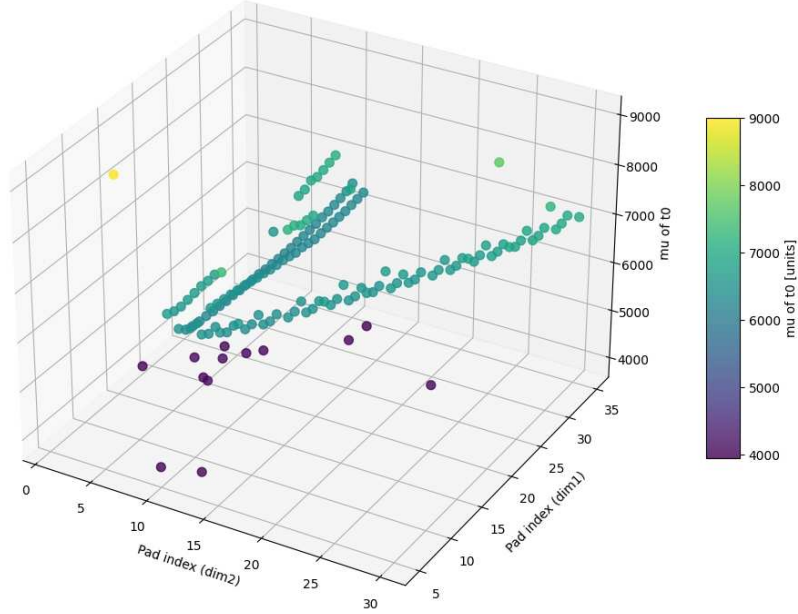


Figure 5.4: Average time track in 3D, in the plot the laser is entering from the top, going to the left, hitting the mirror and moving diagonally.

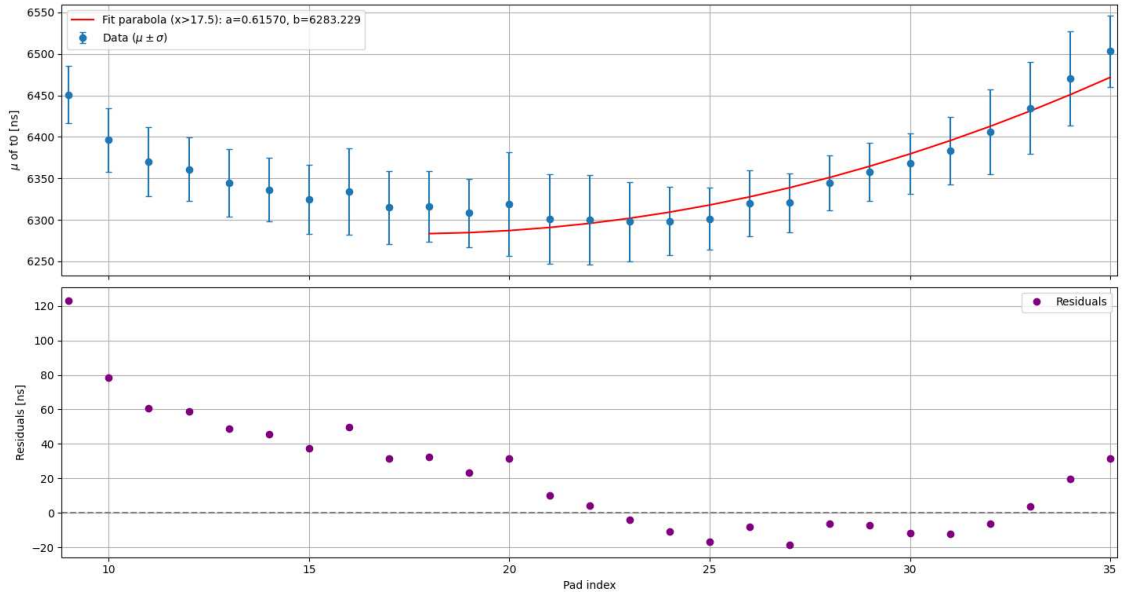


Figure 5.5: Plot of the drift time as a function of the number of the horizontal pad

introducing the delay Δt , the new travel time becomes $t' = t + \Delta t = \frac{d}{v} + \Delta t$, the new velocity is therefore $v' = \frac{d}{t'} = \frac{d}{\frac{d}{v} + \Delta t} = \frac{v}{1 + \frac{v\Delta t}{d}}$, the change in velocity $\Delta v = v' - v$ is $\Delta v = v \left(\frac{1}{1 + \frac{v\Delta t}{d}} - 1 \right) = -\frac{v^2\Delta t}{d + v\Delta t} \approx -\frac{v^2\Delta t}{d}$. For $d = 25\text{cm}$ it yields a factor of $\Delta v \approx 0.05 \frac{\text{cm}}{\mu\text{s}}$.

At the 1σ this effect is limited to a maximum of $3/4\text{cm}$ from the mirror position in the ERAM, but it extends linearly for more pads. All data showed the same trend.

5.4 Effects of added resistance

The aim of this preliminary study was to observe the distortion effects on particle tracks caused by modifying the electric field. This modification was achieved by varying the potential difference between the cathode and the last strip by a known value.

I collected two data sets with the laser pointed nearly to the center of the cathode. The laser was entering the chamber through the small quartz window and reflecting in the mirror to hit the cathode. I worked at $4kV$, so deformation can be more relevant. By adding or removing the external resistance divider, I should notice a change in the drift time of the cathode spot. In my analysis, I selected all the pads and calculated the arrival time for each event. The time is then inserted in a histogram and I performed a Gaussian fit as shown in figure 5.6, only for the cathode pad. In the case without the resistance I get a drift time of $7750.0 \pm 0.7ns$ while with it I get $7832.2 \pm 0.8ns$.

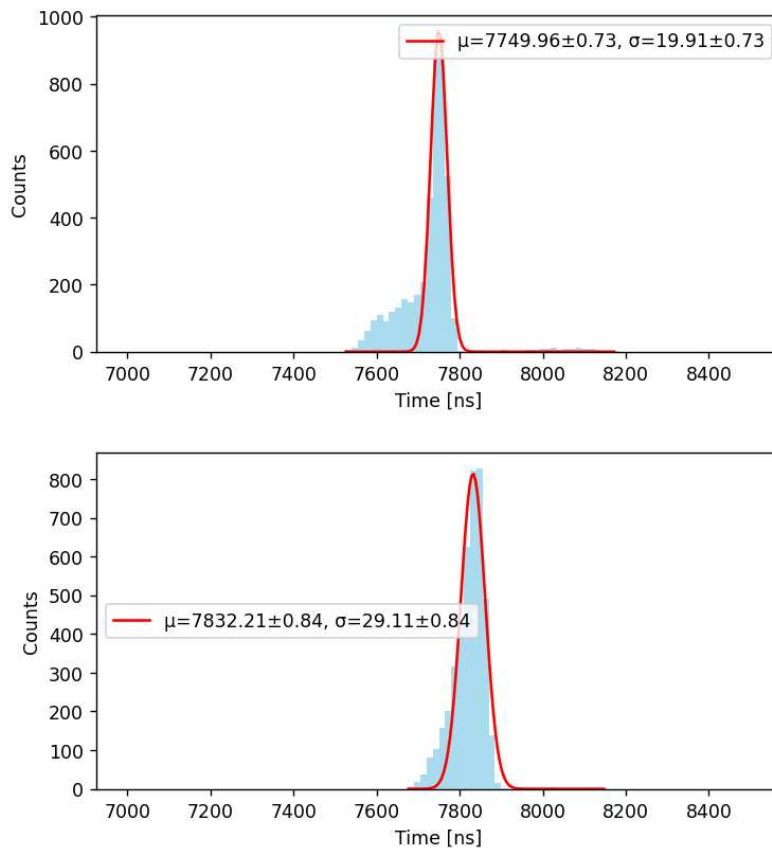


Figure 5.6: Gaussian fit for the case with and without the resistance.

Thinking about what I expected, it is the exact contrary. With the resistance, I should have that the electrons near the cathode drift faster because the field between the first strip and the cathode is increased. At the center of the mTPC, the situation can be intuitively understood by thinking that without the resistance, the HV potential is a plane parallel to the cathode but nearer to the first strip, while with the resistance it is nearer to the cathode. In this way, the simple electric field value given by $E = \frac{V}{d}$ decreases with the resistance because d increases. This is true for the electric field between the first strip and the last one; regarding the electric field between the cathode and the first strip, it is increasing by inserting the resistive bridge,

but the time-shifting effect is mixed with the other one.

To understand if I was committing an error, I plotted the colormap of the difference between with and without the resistance. In figure 5.7 for each pad, the parameter $\Delta\mu = Time_{without\ resistance} - Time_{with\ resistance}$ from the time Gaussian fit is plotted in a colormap. As it is possible to see on the right, the deformations due to the TPC walls produce a higher $\Delta\mu$. But the cathode spot has around the same $\Delta\mu$ compared to the center points. This indicates a total electric field shift that provides a time difference of around $100ns$ at $4kV$.

I can also assert that deformations depend on the applied cathode voltage. This was a debated point about possible deformations in the HATPC. By observing the plot in figure 5.7, on the right part, where the laser is entering, the $\Delta\mu$ is changing by moving to the wall.

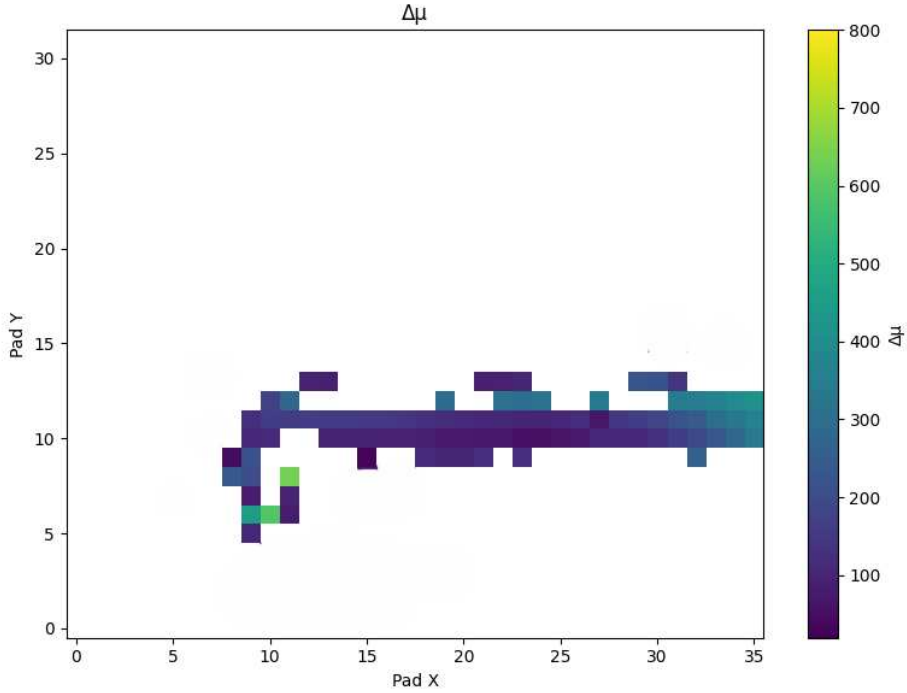


Figure 5.7: $\Delta\mu$ colormap.

5.5 Laser pointing to the ERAM

I also directed the laser directly at the ERAM surface, perpendicular to its plane. The aim of this preliminary study was to observe the tracks generated under a specific condition: when long segments of the track pile up within the same pad.

Initially, I used the lowest possible laser intensity to avoid potential damage to the DLC from prolonged exposure. The laser intensity was gradually increased when no signal was detected. The resulting event in the ERAM appears as a dot-like spot, as shown in figure 5.8, with visible charge spreading to the surrounding pads.

I first observed the waveforms and noticed one peculiar effect. The time at which my waveform crosses the baseline is too early for the secondary pads. To show this, I plot in figure 5.9 all the 9 waveforms. The secondary pads start rising after 1 or 2 bins, so after $40 - 80ns$.

This, in fact, is strange because I should have a constant zero-crossing time of around $105 - 110$, due to the time necessary to the charge to arrive to the pad.

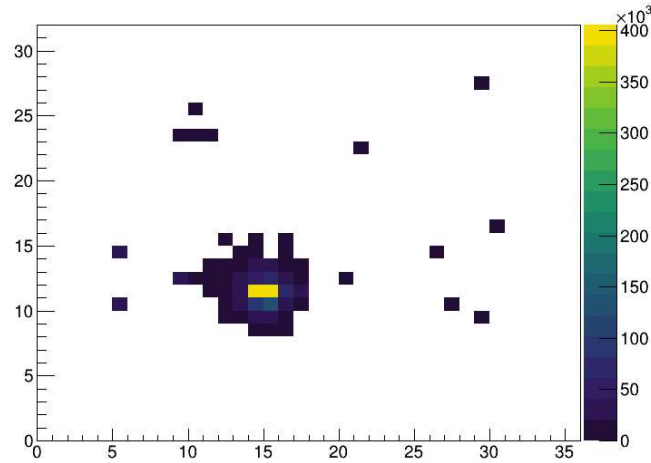


Figure 5.8: Beam spot in the ERAM plane.

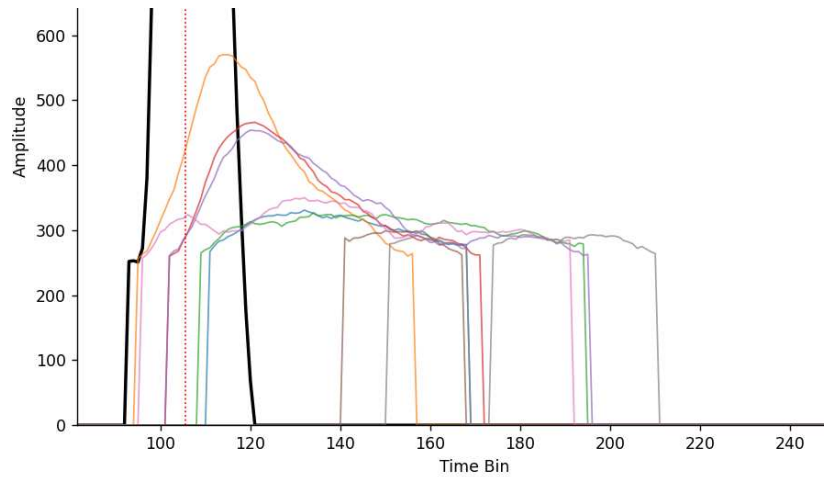


Figure 5.9: The waveforms for all the 9 pads in 3×3 block, the black one is the center one. It is possible to see that the orange and pink start much earlier than expected.

I started thinking about what could be the cause and collected a data set with only the collimator of $500\mu m$ in diameter. In this case, the map color for all the events is plotted in figure 5.10, showing two beam spots. These are both at the $100bins$, indicating they both hit the mesh at the same time. This is due to the laser hitting the cathode and reflecting, thus it generates two beams. One hit the ERAM in the original point while the other lower.

This can be the cause but using the $150\mu m + expander$ and moving vertically or horizontally I still get the anomaly. This can't be due to the cathode because I am changing the position, and sometimes I hit it while others not (the mesh cathode has holes of around $2mm$ and I was moving by $0.5mm$). In addition while for the second case the spot was always present for all the events in the same quantity, the anomalous time shift and peak changes event per event, perhaps due to the intensity of the beam.

To identify the problem, I collected data sets in different conditions.

- changing the frequency of the laser $1Hz, 4Hz, 7Hz, 10Hz, 15Hz$
- manually changing the laser intensity $\approx 25\%, 50\%, 75\%$

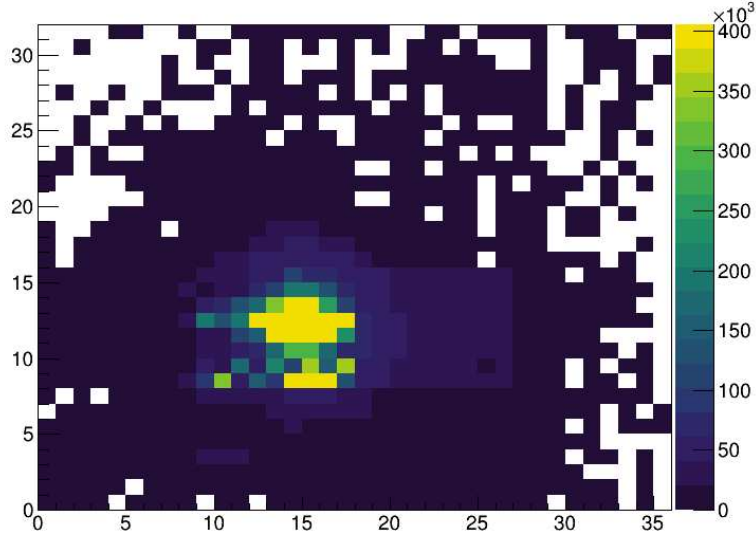


Figure 5.10: The beam spot with the $500\mu m$ collimator.

- changing the DLC voltage $350V, 360V, 370V, 380V$
- turning on and off the laser every $\approx 10s$

In all the data listed the effect was present. I decided then to pass through an analysis process, I calculated the three parameters ($Amplitude_{max}, time_0, time_{peak}$) and analyzed them, especially their 2D histograms.

For example, I show in figure 5.11 the 9 two-dimensional histograms of *charge vs time₀*. The primary pad is positioned at the center while the other eight are the neighboring ones. The region I am interested in is the one near $3700ns$ (ERAM time). In the left and right cases, it is possible to see that all the pads register the anomalous $time_0$. The left one was collected with a DLC voltage of $350V$ while on the right $380V$. It is clear, confronting all the 8 pads, that the two-dimensional peak is moving toward $3700ns$ increasing the DLC voltage. This confrontation has been performed also for all the data sets.

What I noticed is that the peak is moving in the $2D$ plane from higher $time_0$ and lower $Amplitude_{max}$ to lower $time_0$ and higher $Amplitude_{max}$. This movement is visible by increasing the DLC voltage and increasing the beam intensity. I can affirm that the effect has a higher probability of occurring if I increase the laser intensity or the DLC voltage.

My hypothesis was that between the mesh and the DLC, additional charge is behaving in an anomalous way. With this I mean that the charge is not behaving like a normal avalanche but that there is an additional current. Another hypothesis more related to the laser intensity can be that the mesh or DLC are heating up and generating additional photoelectrons.

The main problem behind identifying the physical effect is that it is present in the pads that are $\approx 1cm$ from the beam spot. The reader must consider that the mesh is at a distance of $128\mu m$ from the DLC and so any possible explanation crushes under the effective angle seen from the avalanche, so $\arctan \frac{1cm}{128\mu m}$.

One assumption can be the possibility of crosstalk. In particular, the estimated effect from the AFTER chip is $\approx 1\%$ of the leading pad ADC. In my case, for example, if I saturate the primary pad, the neighboring pads should have a peak around $40ADC$. I calculated this ratio of the primary and secondary pad, this has been challenging as sometimes the peak is mixed in

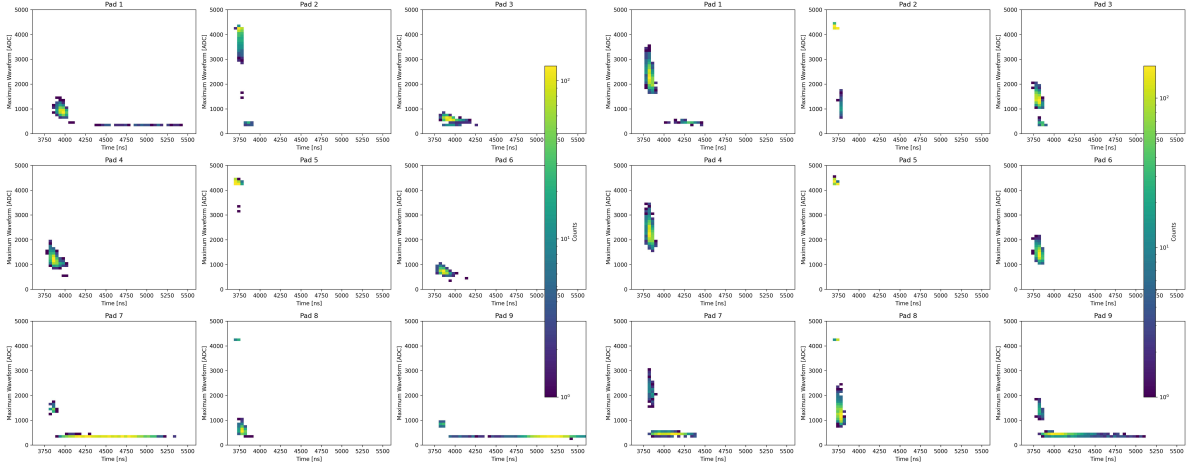


Figure 5.11: On the left the 2D in the case of $DLC = 350V$ while on the right for $DLC = 380V$, it is visible the change of the spot position, especially in the top right pad.

the signal and not clear to extrapolate. I selected the pad with the highest crosstalk. In figure 5.12 I report the histogram, with a simple Gaussian fit, the effect is around 4%. I should need to add the effect of other parasitic capacitance.

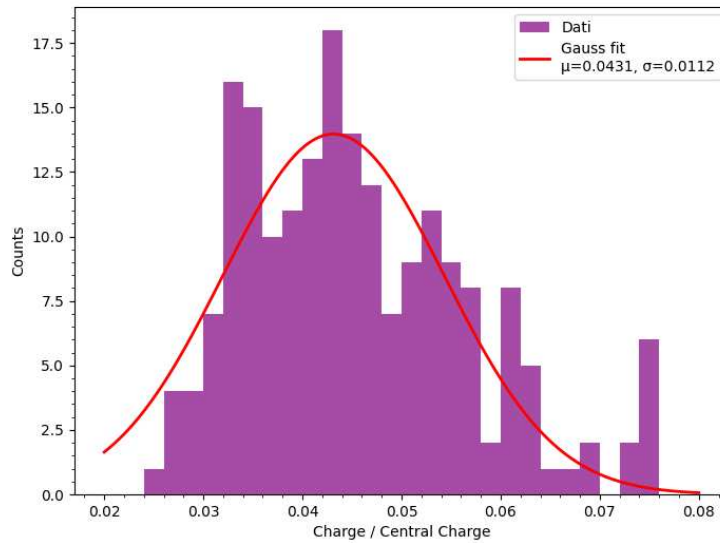


Figure 5.12: The ratio between the peak of the above pad with the central one for the data set at lowest intensity, with an approximated Gaussian fit to evaluate μ and σ .

I then asked myself, if it is crosstalk it should be present also in cosmic muon events, if I find this effect then it is not related to the laser. I found such an event in figure 5.13. I selected only one event because it is necessary to have a higher charge deposition and muons can emit δ rays. I can confirm that this is probably a crosstalk effect.

I started communicating my data with the Paris-Saclay T2K group and results; they are strongly interested in pointing the laser perpendicularly. With this method, the point generated is well localized, triggered, and constant in time. They are conducting specific studies on parasitic

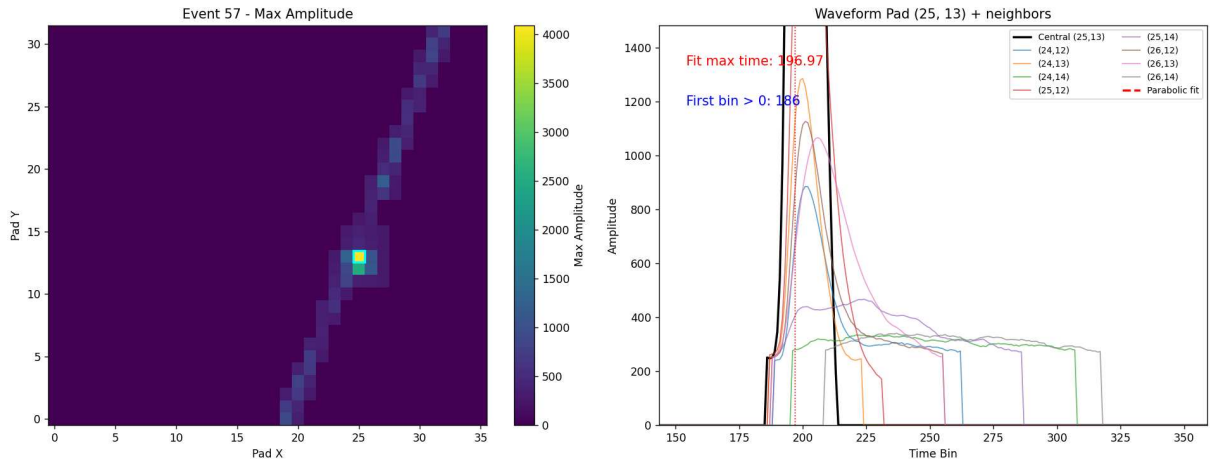


Figure 5.13: A selected event showing the crosstalk effect, the squared pad is the black one on the right, pad (25, 13) present a double peak, compatible in time with my anomalous effect.

capacitance, and this setup can help them in understanding better the effect.

Increasing the intensity further, I generated a perpendicular track in the TPC active volume, and not only in the ERAM gap. Using the $500\mu\text{m}$ collimator, I collected a data run. As shown in the example in figure 5.14, the waveforms appear deformed compared to the usual case of the track being parallel to the ERAM. This is due to the charge arriving at the anode in the same pad within a time window of $\approx 3\mu\text{s}$. The usual asymmetry, evident, for example, while performing the skewed gaussian fit, is no longer present. In addition, the zero-crossing time, which should be around $1\mu\text{s}$, is well beyond this value.

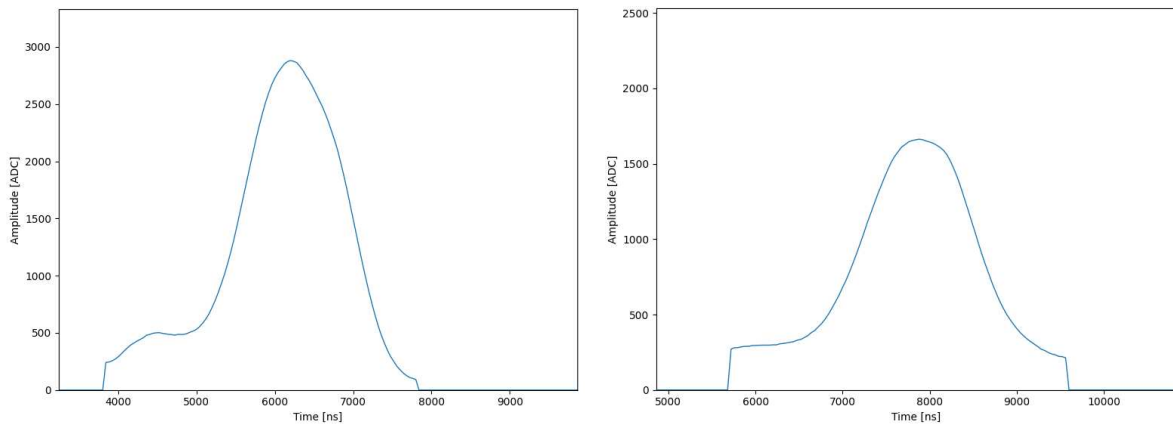


Figure 5.14: Examples of deformed waveforms while pointing the laser perpendicularly to the ERAM.

Chapter 6

A New Track Reconstruction Algorithm

This section describes the numerical model and fitting procedure developed to analyze the detector waveforms. The feasibility of this approach was not initially guaranteed, given the significant computational complexity involved. The analysis began by implementing a complete waveform convolution, with the methodology being progressively refined throughout the study. The ultimate aim of this work is to propose a new, improved algorithm for track reconstruction.

6.1 Pad Response and Gaussian Diffusion Model

First, I performed a mathematical simulation to study the response of a multi-pad detector in 2D to spatially distributed charge. The main goal was to compute the induced waveforms and analyze the shape and amplitude of the signal as a function of geometry and resistive-capacitive RC diffusion.

The full model waveform is

$$S(t) = (Q * E')(t) + \text{baseline},$$

where $*$ denotes convolution, and the baseline is an additive offset parameter, different for each pad.

The time response of the electronics is modeled by the function $E(t)$ [6]

$$E(t) = \left(\frac{t}{t_p}\right)^3 e^{-3t/t_p} \sin\left(\frac{t}{t_p}\right)$$

where t_p is the peaking time of the electronics. A more precise function was reported before as

$$f(t; \omega_s, Q) = e^{-\omega_s t} + e^{-\frac{\omega_s t}{2Q}} \left[\sqrt{\frac{2Q-1}{2Q+1}} \sin\left(\frac{\omega_s t}{2} \sqrt{4 - \frac{1}{Q^2}}\right) - \cos\left(\frac{\omega_s t}{2} \sqrt{4 - \frac{1}{Q^2}}\right) \right]$$

but Q and ω depend on the pad chosen and this was my first approximation.

The time derivative $\frac{dE}{dt}$ was used to convolve it with charge distribution for waveform generation. $E'(t)$ is defined by

$$E'(t; t_p) = \frac{e^{-3t/t_p}}{t_p} \left(3 \left(\frac{t}{t_p}\right)^2 \left(1 - \frac{t}{t_p}\right) \sin\left(\frac{t}{t_p}\right) + \left(\frac{t}{t_p}\right)^3 \cos\left(\frac{t}{t_p}\right) \right)$$

The induced charge $Q(t)$ on a given pad depends on the charge distribution and the geometry of the pad. I modeled the pad as a rectangular region defined by its center coordinates (x_0, y_0) and dimensions w (width) and h (height). The charge distribution along the coordinate s was parameterized by the slope m and intercept q of a linear trajectory in the pad plane. I will not consider the temporal direction of my detector for the moment, the line generated is parallel to the ERAM.

A charge deposited at (x_0, y_0) spreads via a Gaussian diffusion process. The fraction of charge collected on a rectangular pad is given by [6]:

$$Q(t) = \frac{1}{4} \left[\operatorname{erf} \left(\frac{x_{\max} - x_0}{\sqrt{2}\sigma(t)} \right) - \operatorname{erf} \left(\frac{x_{\min} - x_0}{\sqrt{2}\sigma(t)} \right) \right] \left[\operatorname{erf} \left(\frac{y_{\max} - y_0}{\sqrt{2}\sigma(t)} \right) - \operatorname{erf} \left(\frac{y_{\min} - y_0}{\sqrt{2}\sigma(t)} \right) \right]$$

with the maximum and minimum $x_{\min}, x_{\max}, y_{\min}, y_{\max}$ being the pad edges.

Given the time-dependent diffusion parameter $\sigma(t)$,

$$\sigma(t) = \sqrt{\frac{2t}{RC} + \omega^2},$$

where RC and ω are model parameters, the induced charge at time t is computed by integrating over the spatial coordinate s ,

$$Q(t) = \frac{\lambda}{L} \int_{-L/2}^{L/2} \frac{1}{4} \left[\operatorname{erf} \left(\frac{x_0 + \frac{w}{2} - x'(s)}{\sqrt{2}\sigma(t)} \right) - \operatorname{erf} \left(\frac{x_0 - \frac{w}{2} - x'(s)}{\sqrt{2}\sigma(t)} \right) \right] \\ \times \left[\operatorname{erf} \left(\frac{y_0 + \frac{h}{2} - y'(s)}{\sqrt{2}\sigma(t)} \right) - \operatorname{erf} \left(\frac{y_0 - \frac{h}{2} - y'(s)}{\sqrt{2}\sigma(t)} \right) \right] ds$$

where the rotated coordinates are

$$x'(s) = s \cos \theta, \quad y'(s) = s \sin \theta + q,$$

with $\theta = \arctan(m)$ and λ the overall charge amplitude parameter.

This integral was numerically evaluated over a finely spaced vector $s \in [-L/2, L/2]$. The line was defined beforehand as uniform in charge along its direction.

I report in figure 6.1 an example of line generated with relative waveform. I use the parametrization: m is the slope of the line, while q is the distance along the vertical axis from the center of the pad.

6.2 LogQ method

This subsection explains the fundamental principles of the current tracking algorithm used in the HATPCs. The goal is to identify its critical aspects and potential areas for improvement. The analysis is based on the mathematical function describing the waveform.

Three vertically stacked pads were defined, Pad_1 top, Pad_2 center and Pad_3 bottom. A horizontal line of charge points across the center of Pad_2 was simulated. For each point, the waveform on each pad was computed, with a chosen initial $RC = 100 \frac{ns}{mm^2}$. The plot of the waveforms is reported in figure 6.2.

In the implemented tracking algorithm for the HATPC, the $\log Q$ method is used [30]. It works with the ratio $\log(\text{Peak}_{\text{Pad}1}/\text{Peak}_{\text{Pad}3})$. To understand its working, for different horizontal lines of charges the waveform was computed to study the effect of diffusion distance on the amplitude of the signal. The ratio curve is fitted using a two-term exponential decay model:

$$f(y) = a_1 e^{-by} + a_3 e^{-by^3} + c$$

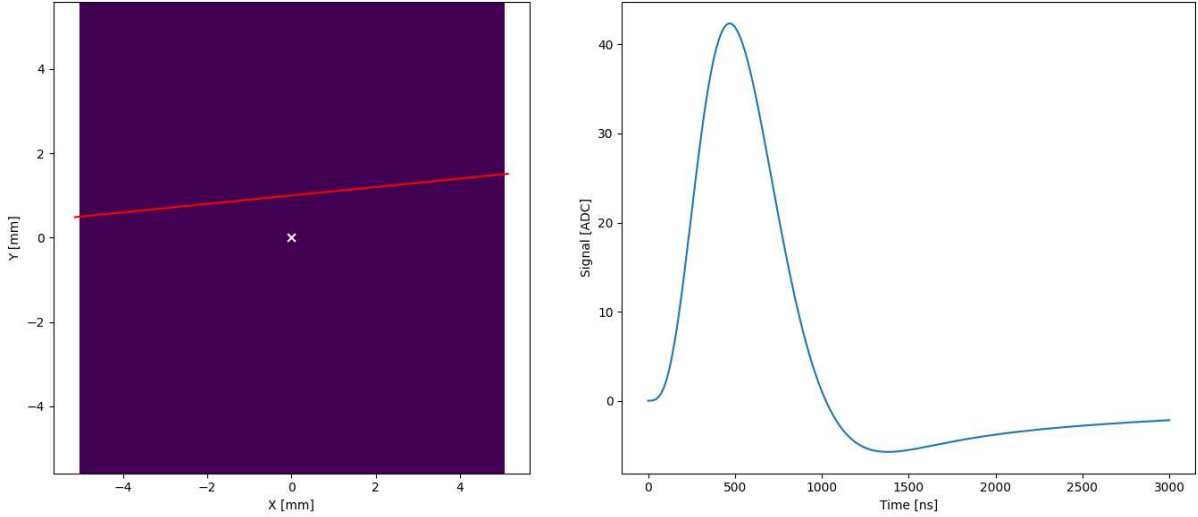


Figure 6.1: On the left the pad with the track while on the right the induced signal.

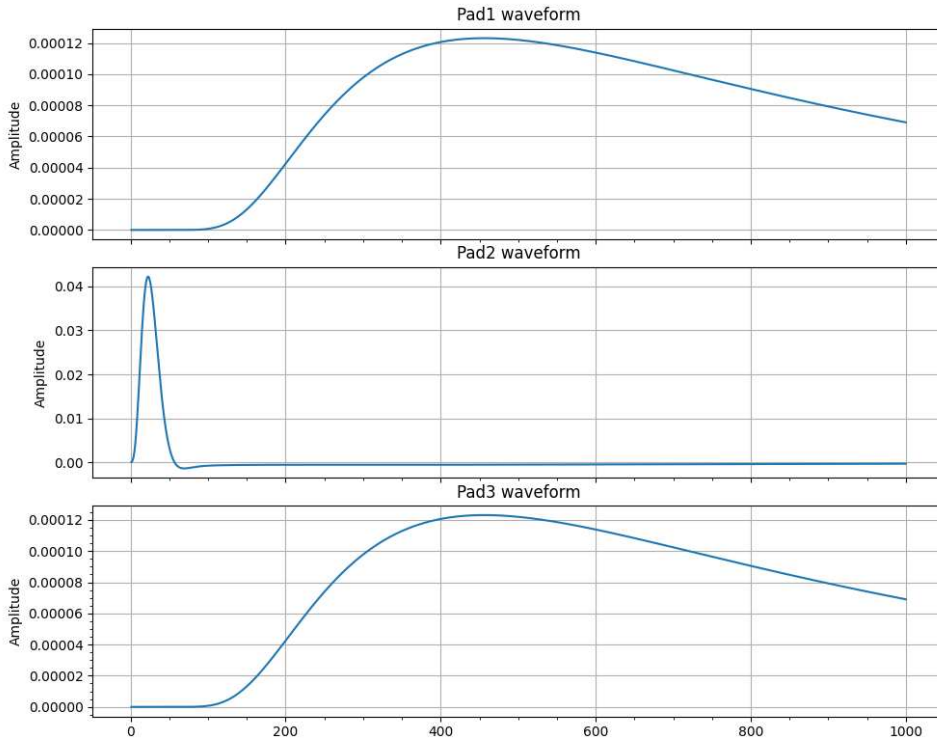


Figure 6.2: Example of waveforms for Pad_1 , Pad_2 , and Pad_3 .

The analysis was repeated for different RC values: 5, 10, 20, 50, 100 ns/mm². For each RC value, a fit was performed and overlaid on the plot. In figure 6.3 it is possible to see the value of the ratio as a function of the vertical distance from the center pad.

As is possible to see, it is only an empirical method and in this section I wanted to improve it, especially considering that it is limited by the clustering choice. In addition, considering the uniformity of the laser track both in direction and charge deposited, compared to muon events, it is the perfect test field. Clustering means that I have to select the bottom and top pad, but

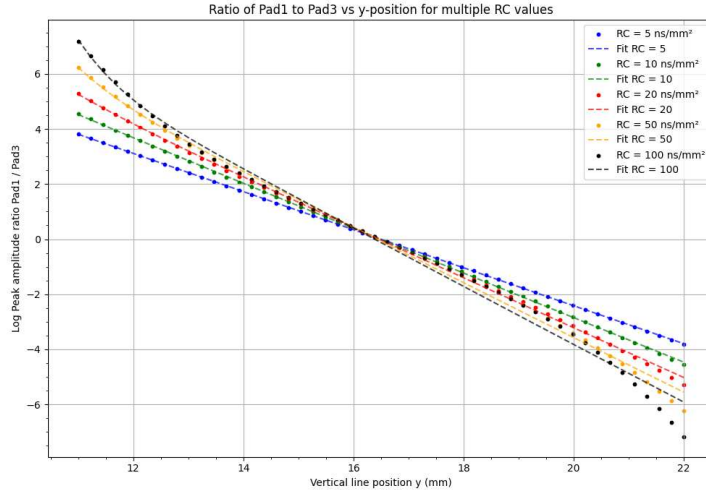


Figure 6.3: Peak amplitude ratio curves and fits for various RC values.

in some cases they are not unequivocally defined. In particular, the clustering process is choice-based, creating a bias on the determination of which secondary pad is part of which cluster; this is physically not true, as the charge spreads all over the resistive layer without distinction.

Now I want to show another problem by changing the angle of the line. A line of charge was generated for points passing for the horizontal middle of the center pad and rotated at different angles in a system of pad 3×3 (with Pad_5 the center one); the waveform response was analyzed for selected pad pairs. The ratio $\log(\text{Peak}_A/\text{Peak}_B)$ is visualized as a function of the line angle and the vertical position in the middle. This log-ratio is plotted in figure 6.4 as a function of track angle and vertical position to evaluate how sensitive pad pairs are to angular variations and position. So the figure shows

$$R(\theta, y) = \log \left(\frac{\max \text{WF}_A(t)}{\max \text{WF}_B(t)} \right)$$

The fitting model used in the figure is a general polynomial fit

$$f(y, \theta) = a_0 + a_1y + a_2y^2 + b_1\theta + b_2\theta^2 + c_1y \cdot \theta$$

In this way, I can observe the contour plot with an analytical formula.

From this I could use the fit results or the single map values. To determine the position and angle it was then necessary to calculate the ratio Pad_2/Pad_5 and Pad_5/Pad_8 : these results provided a 2D curve in the map (θ, y) with the intersection being the corresponding θ and y values.

The problem now was that if I had 3 pads I could perfectly determine the angle based on this ratio, but it changed drastically as a function of RC . The assumption that RC is constant, as the model is today, generates a bias for each pad. In addition, if only two pads are active, the left or right plots must be used and the position bias is up to 4mm , which is half the pad.

Then I wanted to perform a new analysis, eliminating the concept of clusterization and using the complete waveform or the time instead of the amplitude. In addition, a more robust parameter could be used that changes less as a function of RC .

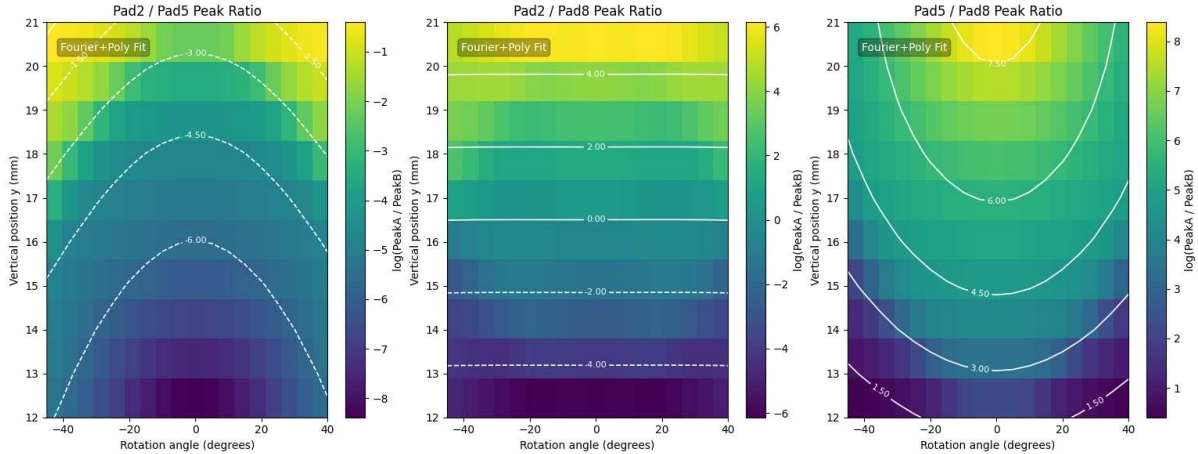


Figure 6.4: Peak amplitude ratio 2D plots and fits.

6.3 Waveform Fit Based on the Gaussian Diffusion Model

The analysis was initially performed using a single data set featuring a horizontal laser track created with the $500\mu\text{m}$ collimator. This specific configuration served as a simplified test case. However, the analysis program was designed to be generalizable, first to tracks at any angle, and subsequently to muon events.

I first considered a uniform RC and $gain$ for a pad, so that the parameter vector to be estimated for a single pad was

$$\mathbf{p} = \left(\underbrace{m, q}_{\text{line parameters}} \quad \underbrace{RC, \lambda, \omega}_{\text{Micromegas and gas parameters}} \quad \underbrace{t_p, \text{baseline}, t_{\text{shift}}}_{\text{electronics parameters}} \right)$$

where t_{shift} accounts for a horizontal shift in time to align the model with the data, m and q are the line parameters, t_p the peaking time of the electronics response, ω the initial line width from the formula of $\sigma(t)$ and λ the charge amplitude. Using only a single waveform, I normalized to 1 the curve to eliminate the λ parameter, and eliminated the baseline by using the first waveform value, as for the t_{shift} . In this way, the fit was aided in the convergence.

The fitting was performed by minimizing the least squares difference between the measured waveform and the model and the convolution was performed using the FFT-based method for computational efficiency.

$$\min_{\mathbf{p}} \sum_i [S_{\text{data}}(t_i) - S(t_i; \mathbf{p})]^2.$$

Figure 6.5 illustrates an example of fit to a single waveform, showing the data and the model overlay. For all data, the fit result is well performed and overlaps accordingly.

The χ^2 space phase as a function of the parameters is too flat, and thus the errors on each parameter were too large, to be used. The parameter errors for the results were not sufficient to determine the track angle and distance from the center.

This effect was observed also by numerically calculating the waveforms for different m, q, RC . All waveforms presented similar stretching by changing these parameters as reported in figure 6.6. The fit did not converge to a minimum because there was not simply one but a multidimensional space of possible values. As can be seen in the figure, the waveform depends on too many parameters, and so stretching it or squeezing could be performed by different combinations of the parameters.

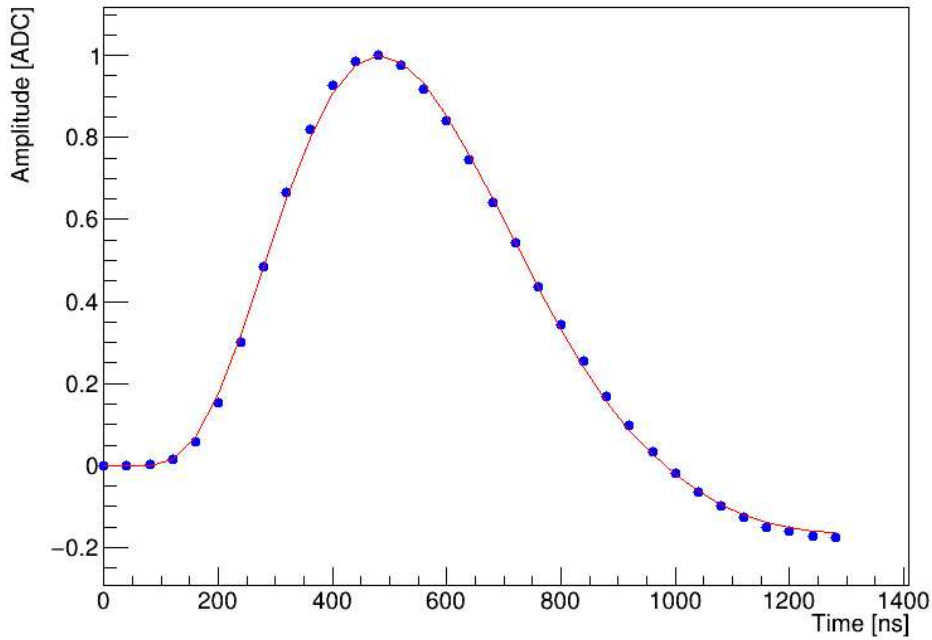


Figure 6.5: Example fit of the model waveform to the data for a single pad in one event.

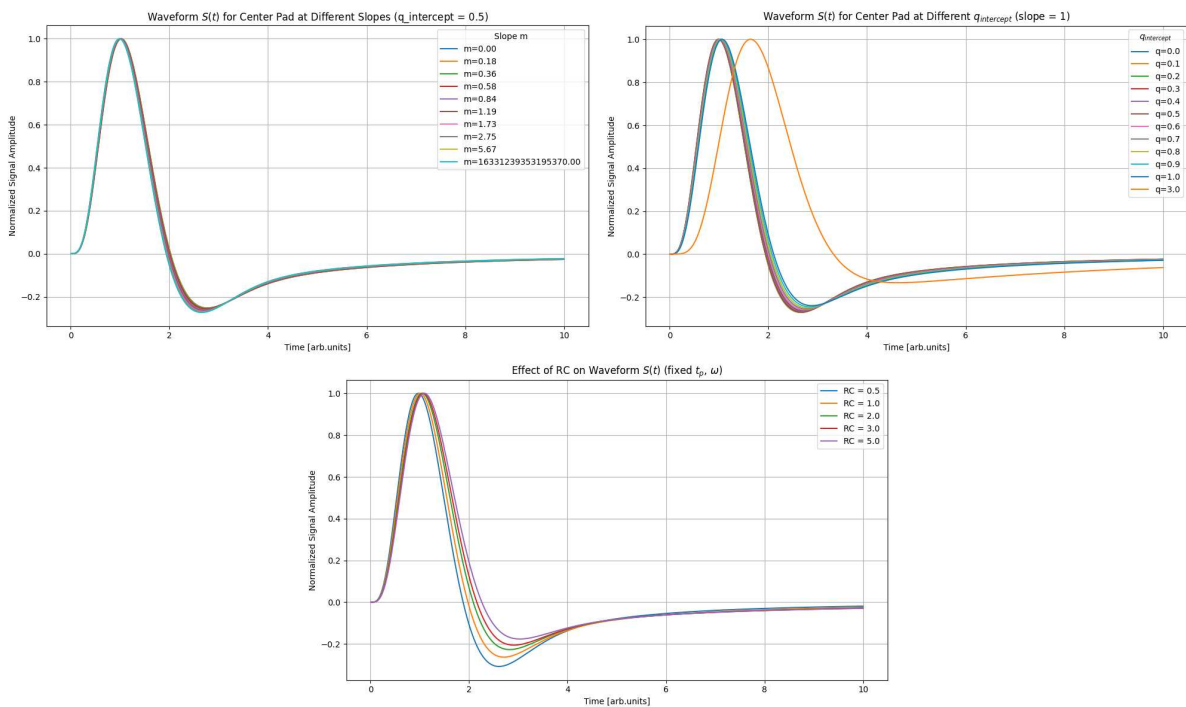


Figure 6.6: Example of different waveforms changing the parameters. On the top left changing m , on the top right q , and on the bottom RC .

It is important to note that the difference between the curves is increased in the region of the minimum. I could then create a model using this point, but for high waveforms the minimum is below $0ADC$ and not available. The points of interest that could be analyzed are, for example, the zero-crossing and the peak.

6.4 Multiple pad fit

Now, the fit for a single pad did not return the important values (m, q) for track reconstruction, but if I fit at the same time the same charge line for multiple pads I could reduce the fit freedom.

Then I proceeded to create an algorithm that did the exact same fit as before, without the normalization. The fit performed a χ^2 minimization at the same time for the central pad, the upper pad and the bottom pad, maintaining the same m, q, t_{shift} and RC . The data set I used had parallel tracks, so there was no ambiguity that the central pad was the primary one. I first wanted to test it before implementing it in general.

The fit performed in such a way returns an example as in figure 6.7.

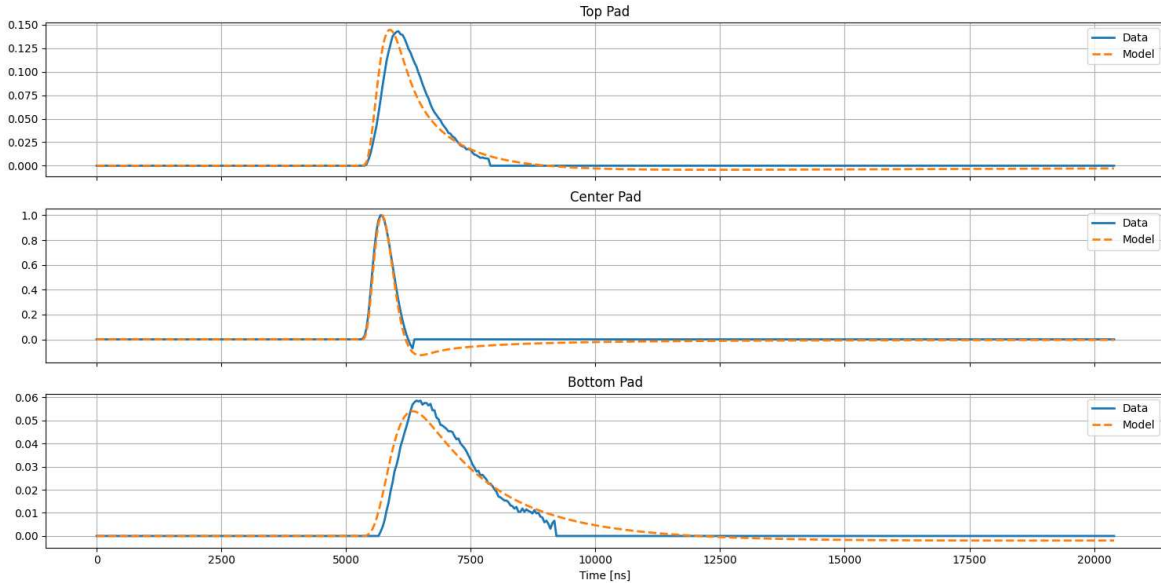


Figure 6.7: Example fit of the model waveform to the data for three pads in one event.

It is possible to notice how the bottom and upper pads present a shift in the peaking time. This effect can be due only to one factor, an anomalous RC value. To clarify this, let's observe the central pad, which is well fitted: this means that the RC value is correct. Now, if I assumed that the shift was due to the different RC per pads, I should have observed a positive and negative shift, but this was not the case. This means that a pad has a different RC if measured while it is primary than while it is secondary. This effect will be explained later in full details in section *Problematic of the model*.

Even in this case, the fit errors were multiple times higher than the parameters and the convergence was not well defined. I could impose different RC for each pad, but it is obvious that it would be computationally costly and that by increasing the number of parameters I would decrease the convergence efficiency.

I then decided to initially analyze only one point of the complete waveform, the zero-crossing point. This approach was later changed to a general parameter, doing feature extraction.

6.5 Empirical Waveform Fit and Feature extraction

As previously noted, the waveform shape depends on the parameters m, q , and RC . Different combinations of these parameters can produce similar curves, creating degeneracy. Therefore,

the first step was to understand how the zero-crossing times within pad groups vary with track position and RC constant.

Experimentally, the zero-crossing time for a typical waveform is approximately $1\mu s$, with a sampling rate of $40ns$. The differences in zero-crossing times between pads has sufficient resolution for track determination. However, potential issues included degraded resolution for secondary pads and the influence of local RC variations on this parameter.

To address this, I initially attempted to compute the zero-crossing point using the complete mathematical waveform model. However, the C++ implementation proved too computationally intensive for practical use, as it required FFT-based convolution. Even with multi-threading, the numerical complexity remained challenging.

An intuitive solution was to employ an empirical analytic function that closely approximates the waveform. This approach serves as an effective noise reduction technique, which later proved fundamental for noise filtration. Additionally, since the zero-crossing time is not directly measurable for secondary pads, it must be extracted through this fitting procedure.

The waveform is empirically modeled as follows:

$$y(t) = \text{scale} \times \text{step}(t - t_0, \tau_r) \times \text{env}(t - t_0, \tau_d) \times \cos(2\pi f(t - t_0) + \phi)$$

with

- **step** the error function for rise time:

$$\text{step}(t, \tau_r) = \frac{1}{2} \left(1 + \text{erf} \left(\frac{t}{\tau_r} \right) \right)$$

- **env** an exponential decay:

$$\text{env}(t, \tau_d) = e^{-t/\tau_d} \quad \text{for } t > 0$$

- **osc** the oscillatory part:

$$\cos(2\pi f(t - t_0) + \phi)$$

Figure 6.8 shows that the fitted model closely matches the waveform. This agreement is also evident for the secondary pads, which exhibit a longer decay time and do not cross the zero line within the observed time interval.

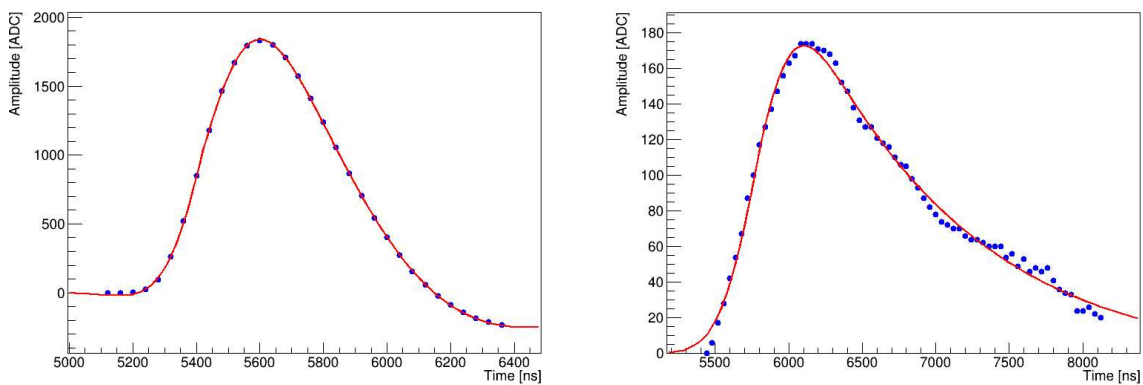


Figure 6.8: Example fit using the empirical function.

The parameters were saved in a ROOT file for subsequent analysis. These parameters include the scale A , the time offset t_0 , the rise time τ_r , the decay time τ_d , the frequency f , and the phase ϕ .

For each event, the parameters were organized into a $36 \times 32 \times 6$ matrix. Elements were set to zero if the fit failed or no waveform was detected. This matrix fully captures the essential information from all the waveforms.

A natural question is why this function was chosen over the skewed Gaussian used in the standard HATPC analysis. The key advantage is that this function can model waveforms that cross zero, which is not possible with the skewed Gaussian.

Several features or observables can be extracted from the measured waveforms. The zero-crossing time, for instance, provided a useful starting point for the analysis. This section examines the most common parameters used in waveform analysis, which are divided into four categories:

- **Time:** the time width determines how the charge moves over the pad
- **Intensity:** related to the peak, determines how much charge was deposited
- **Integral:** always considered from one point to another
- **Derivative:** determines how the waveform change and can be related to the current

I first started with the easiest ones.

Zero-Crossing Time. The zero-crossing time is defined as the first time after the signal peak at which the waveform crosses zero:

$$t_{\text{zc}} = \min \left\{ t \mid S(t) > 0, S(t + \Delta t) \leq 0 \right\}.$$

Peaking Time. The peaking time is the time at which the signal reaches its maximum amplitude:

$$t_{\text{peak}} = \arg \max_t S(t).$$

Area. The waveform is integrated before and after the peak (up to the zero-crossing) to compute:

$$A = \int_{t_0}^{t_{\text{zc}}} S(t) dt.$$

The analysis was performed in two steps, starting by generating the waveforms according to the Gaussian Diffusion Model:

- I calculated heatmaps across a 3×3 pad array, showing the spatial distribution of the parameter, as shown in an example in figure 6.9 for the value of the zero-crossing time.
- I created parametric plots of the observables as a function of the shaping constant RC for selected pads in the 3×3 system, similar to figure 6.10.

These results allow me to study how the parameters change with (m, q) and how the shaping constant RC affects the observables. Although the effect of RC can be considered secondary, it combines with other effects, such as the charge spreading time (as will be discussed for the ion current). Stability with respect to RC indicates robustness over a wider range of non-uniformities. Additionally, I aimed for the parameters to be highly sensitive in distinguishing between different pairs of (m, q) .

Beyond zero-crossing, peaking, and area-based observables, I extracted a broader set of waveform parameters to characterize the signal shape. This provides a more comprehensive description of the detector response and its dependence on the shaping time constant RC .

From each shaped signal $S(t)$, the following parameters were extracted:

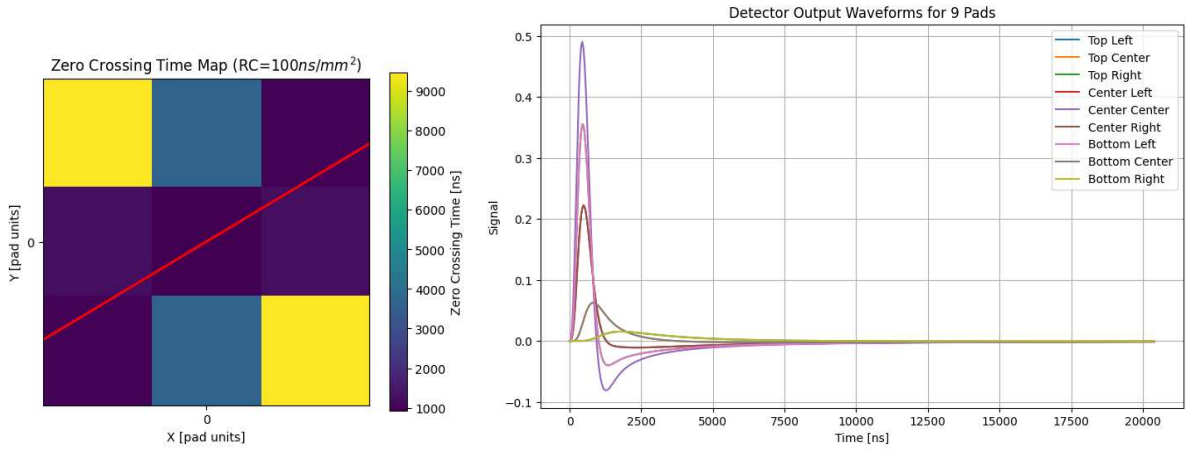


Figure 6.9: Example of heatmap on the left, while on the right of all the waveforms.

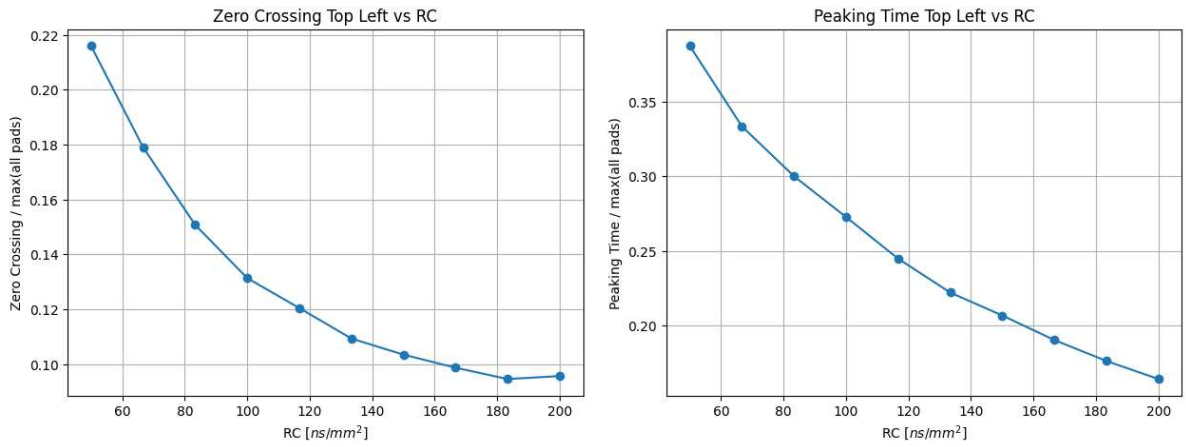


Figure 6.10: Example of RC dependence of the parameter.

- **Skewness (Skew):** The difference between the peaking time t_{peak} and the centroid time t_{centroid} of the waveform, quantifying asymmetry:

$$\text{Skew} = t_{\text{peak}} - t_{\text{centroid}}.$$

- **Base-to-Output Strength (BOS):** The ratio between the signal amplitude and its mean value:

$$\text{BOS} = \frac{S_{\text{max}} - S_{\text{min}}}{\langle S \rangle}.$$

- **Base Occupancy Time (BOT):** The temporal width of the signal at half maximum (time between 50% rising and falling crossings).
- **Rising Rate:** The slope between 10% and 90% of the rising edge:

$$\text{Rising rate} = \frac{0.8 \cdot A}{t_{90} - t_{10}},$$

where $A = S_{\text{max}} - S_{\text{min}}$.

- **Falling Rate:** Defined analogously on the falling edge:

$$\text{Falling rate} = \frac{0.8 \cdot A}{t_{10}^{\text{fall}} - t_{90}^{\text{fall}}}.$$

- **Fast Amplitude Indicator (FAI):** Maximum derivative of the waveform over a small time window:

$$\text{FAI} = \max \left(\frac{dS}{dt} \right).$$

- **Amplitude-Time Index (ATI):** The normalized peaking time relative to the total duration:

$$\text{ATI} = \frac{t_{\text{peak}}}{t_{\text{total}}}.$$

- **Rise Index (RI):** The ratio of amplitude to maximum signal value:

$$\text{RI} = \frac{A}{S_{\text{max}}}.$$

- **Steepness at half maximum:** on the rising edge, the slope is approximated as

$$\left. \frac{dS}{dt} \right|_{S=\frac{1}{2} \max(S)} \approx \frac{S(t_2) - S(t_1)}{t_2 - t_1},$$

where t_1, t_2 are time samples just before and after the half-maximum crossing.

- **Slope of the signal at half of its maximum amplitude, but on the falling edge**

$$\text{slope}_{\text{fall}} = \frac{S(t_2) - S(t_1)}{t_2 - t_1}, \quad t_1, t_2 \text{ just after half-max.}$$

As before, I produced a color map of the value for a set of 3×3 pads and for a single pad as a function of RC . In the RC plot I used the top left pad or the center pad, normalized for the maximum cell value. More clearly, I calculated the parameters for the matrix 3×3 , I calculated the maximum and divided all of them by it. This is because, in order to create a meaningful comparison, I have to analyze the fractional difference (or percentage).

Certain parameters for the top-left pad remain stable at a normalized value of 1, as this pad consistently registers the maximum signal in the system. In this case, I instead selected the center pad as the reference pad. This is particularly relevant for parameters like the zero-crossing time, which is consistently longer in secondary pads compared to primary ones.

This extended analysis enables a multidimensional characterization of the signals. I systematically selected parameters based on their dependence on RC , prioritizing those with more gradual variation. For the track parameters (m, q) , I systematically evaluated their colormaps, requiring the presence of a discernible and consistent variation.

Based on this comprehensive study, the most effective parameter identified was the integrated area from zero to the zero-crossing time. This parameter demonstrates minimal sensitivity to RC variations while exhibiting a substantial dynamic range in response to changes in (m, q) . Consequently, I focused further on this parameter.

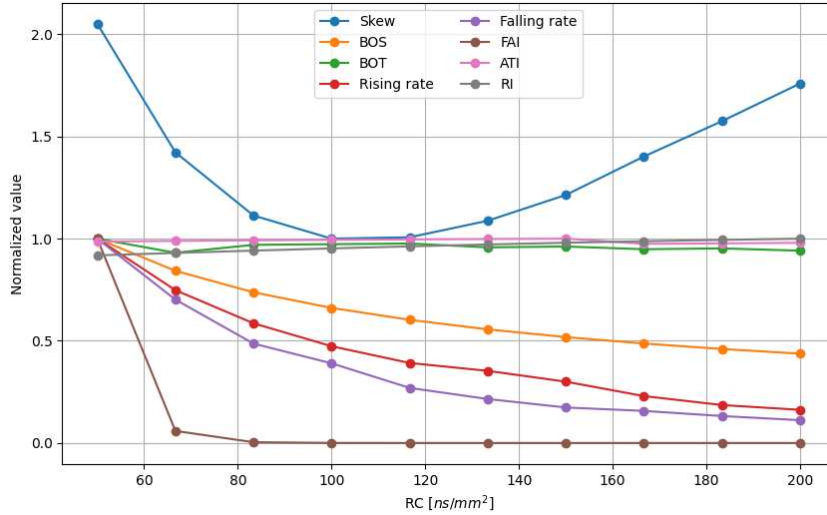


Figure 6.11: Example of the dependence of the parameter as a function of RC . Where the value is constant at 1, it means the top left pad is the pad with the maximum parameter value, for all nine.

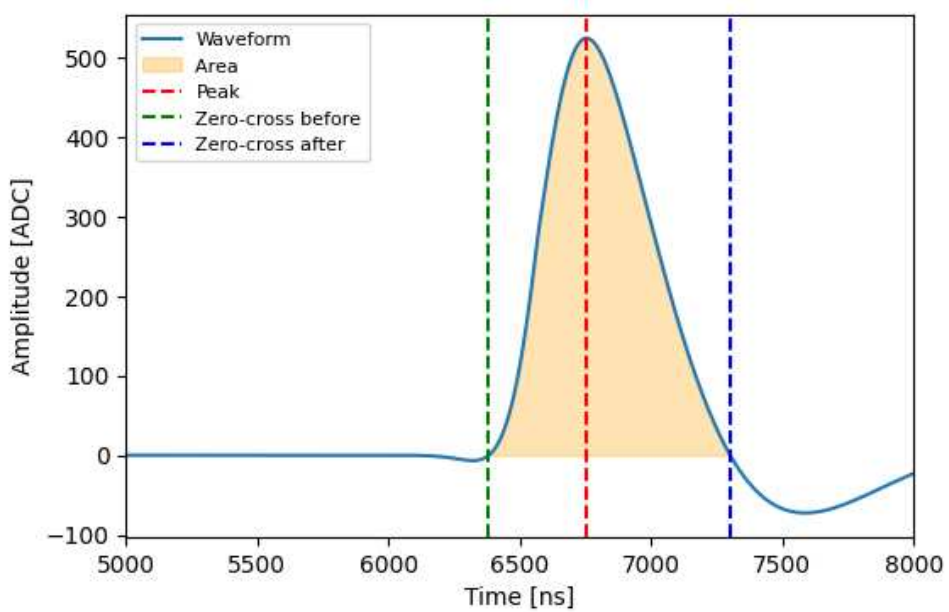


Figure 6.12: Example of area extraction from a waveform from zero-crossing time before and after the peak. The waveform is calculated using the parameters.

6.6 Extraction of Signal Areas

For each pad, the signal area is calculated by integrating up to the first zero-crossing:

$$A = \int_0^{t_{zC}} S(t)dt.$$

I recall that my parameter space is composed by the vector

$$\mathbf{p} = (\underbrace{m, q}_{\text{line parameters}} \quad \underbrace{RC, \lambda, \omega}_{\text{Micromegas and gas parameters}} \quad \underbrace{t_p, \text{baseline}, t_{\text{shift}}}_{\text{electronics parameters}})$$

I want then to show how a subclass of parameters can be disregarded:

1. **Baseline and t_{shift} :** they are eliminated from the waveform analysis by a simple subtraction.
2. **Dependence on peaking time t_p :** with the geometry of the track fixed, the variation of the Top Left pad area as a function of t_p is calculated.
3. **Dependence on ω :** similarly, the effect of the initial spread ω on the Top Left pad signal area is studied.
4. **Dependence on gain or λ :** the main problem of the area is that it retains the gain dependence per pad of the MICROMEAS and the track disuniformity that I tried to avoid. To solve this problem the area is normalized by the signal maximum

$$A_{\text{norm}} = \frac{A}{\max(S)}.$$

I report the two plots for ω and t_p , showing that the dependence for the first one is negligible, while for the second one it is linear.

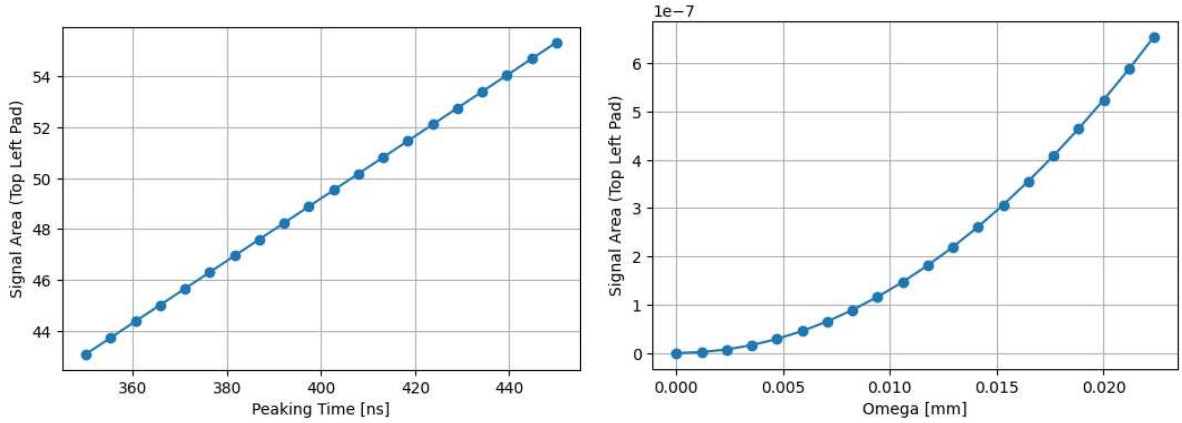


Figure 6.13: On the left the area as a function of the peaking time, while on the right the value $(\text{area}(\omega) - \text{area}(0))$, to clearly show how the change in area due to ω is of order of 10^{-7} .

The time integral of a convolution can be expressed as the product of the integrals of the two individual functions, under certain conditions. For the convolution $S(t) = (Q * E')(t)$, integrating over all time gives:

$$\int_{-\infty}^{\infty} (I * E')(t) dt,$$

then by swapping the order of integration (Fubini's theorem), I have

$$\int_{-\infty}^{\infty} \int_{-\infty}^{\infty} I(\tau) E'(t - \tau) d\tau dt = \int_{-\infty}^{\infty} I(\tau) \left(\int_{-\infty}^{\infty} E'(t - \tau) dt \right) d\tau = \int_{-\infty}^{\infty} I(\tau) d\tau \cdot \int_{-\infty}^{\infty} E'(t) dt.$$

Over the full time domain, the integral of a convolution equals the product of the integrals of the two individual functions. However, when integrating over a finite interval, such as from 0 to T , this property holds only approximately. In my case, the double integral $\int_{-\infty}^{\infty} \int_{-\infty}^{\infty} I(\tau)E'(t-\tau)d\tau dt$ equals zero because $\int_{-\infty}^{\infty} E'(t)dt = 0$. By integrating only up to the zero-crossing time, I introduce an approximation error. Nevertheless, since the area depends linearly on the peaking time t_p , this error does not affect the subsequent reasoning.

Given that the peaking time t_p has a linear effect and is constant across at least nine adjacent pads, the electronic influence can be approximated as a constant multiplicative factor. This effect is eliminated by normalizing the area values, so dividing each area by the maximum area among the nine pads.

As a result, the normalized area in my simulations depends on the parameters (m, q, RC) . The choice of a parameter with low sensitivity to RC means that the normalized area now depends primarily on (m, q) .

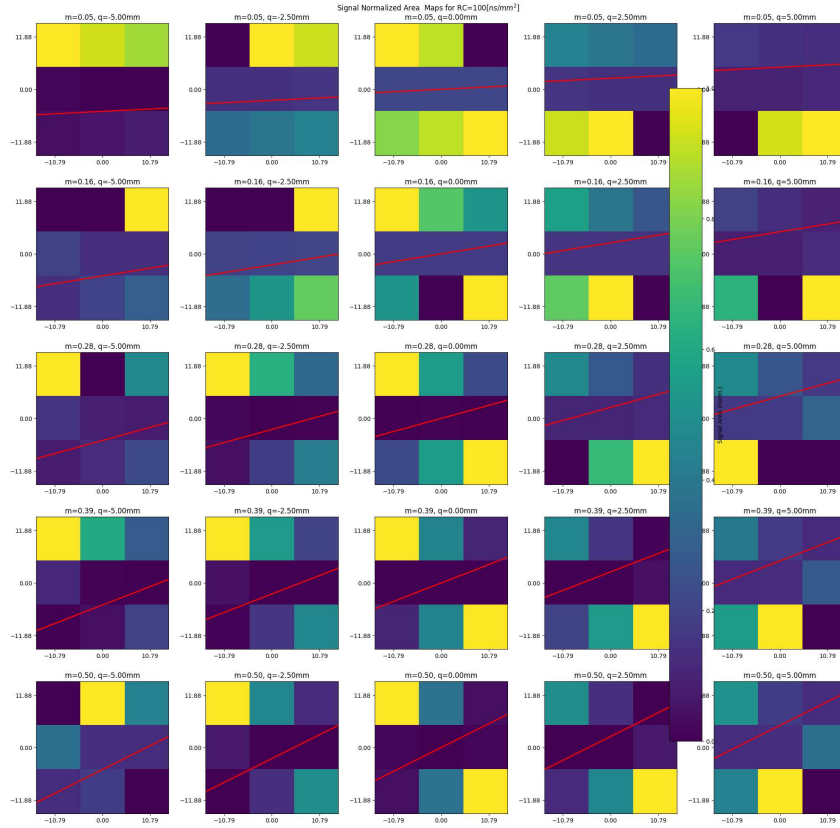


Figure 6.14: The colormaps for different (m, q) for the ratio $\frac{area}{maximum}$.

The normalized area can be interpreted as the base of a triangle. This approximation arises because the area under the curve from time zero to the zero-crossing time can be simplified as $A = \frac{1}{2} \times (\text{zero-crossing time}) \times \text{maximum amplitude}$. After dividing by the maximum amplitude, the result is approximately half the zero-crossing time.

It is reasonable to question why this parameter is better than simply using the zero-crossing time directly. The key issue is that for secondary pads, the exact zero-crossing time often cannot be measured directly because it falls outside the data acquisition window. Extracting it from an incomplete waveform would introduce large errors, whereas the area-based method relies on extrapolation that is more robust. Specifically, the area between the end of the recorded waveform and the actual zero-crossing point is a small fraction of the total area, while the zero-

crossing time itself can be as long as 15–25 μs for secondary pads—well beyond the duration of the data window.

The normalized area has units of nanoseconds (ns) and is approximately equal to $\frac{1}{2} \times$ zero-crossing time.

6.7 Incorporating the effect of ions

This section addresses two limitations not considered in the previous model: the effect of ions and the track inclination with respect of the drift (or temporal) direction. These effects were initially omitted to avoid complicating the analysis.

Since long time, the HATPC group observed that the measured RC value, determined using a ^{55}Fe source, was approximately 2.7 times higher than expected in the primary pad [6]. This discrepancy was attributed to ion effects, which generate an additional current through the Ramo theorem mechanism [28]. The ions create their own electric field that contributes to the Ramo equation $i(t) = q\vec{v}(t) \cdot \vec{E}_w(\vec{r}(t))$. A corrected parametrization for σ accounts for this effect:

$$\sigma(t) = \begin{cases} \sqrt{\frac{2t}{3RC}}, & 0 < t \leq T, \\ \sqrt{\frac{2}{3RC} \left(2t + \sqrt{t(t-T)} - T\right)}, & t > T, \end{cases}$$

where T represents the ion drift time.

The main challenge in implementing this correction lies in accurately modeling the ion mobility. Preliminary estimates suggested an ion mobility of approximately $2.7 \text{ cm}^2/(\text{V}\cdot\text{s})$, corresponding to $T \approx 0.16 \mu\text{s}$. However, achieving agreement with my data would require a much larger T value, which is physically unrealistic. I attempted to recalculate the effect using a step-induced current approach but found that an additional amplitude factor was necessary.

As a practical solution, I introduced a simplified parametrization where RC is multiplied by a factor XRC applied only to primary pads, giving an effective $RC_{\text{effective}} = XRC \cdot RC$.

The second limitation concerns temporal inclination in the simulation. Implementing this required stretching the step time Δt by a constant factor, which substantially altered the numerical calculations. Given the complexity and the expected minor impact—especially considering the maximum physical inclination of approximately 30° for particles like muons crossing the mTPC chamber—I decided to omit this effect from the current model.

6.8 Parameter Distributions and Relative Errors

I asked myself if the extracted normalized area from the data could be used in the analysis; perhaps the error was too large and the fit was insensible to (m, q) . As can be seen from the image of the 3×3 colormap, I expected this to not be my case, but it was considered.

For each parameter p_i in my set of parameters, the distribution of its values and the relative error are analyzed. In figure 6.15 the left side histogram shows the distribution of p_i , the right side histogram shows the relative error in percentage for the parameter p_i . I recall that I am using the previous model

$$y(t) = A \frac{1}{2} \left(1 + \operatorname{erf} \left(\frac{t}{\tau_r} \right) \right) e^{-(t-t_0)/\tau_d} \cos(2\pi f(t-t_0) + \phi),$$

where A is the amplitude, t_0 is the onset time, τ_r and τ_d are the rise and decay times, f is the oscillation frequency and ϕ is the phase.

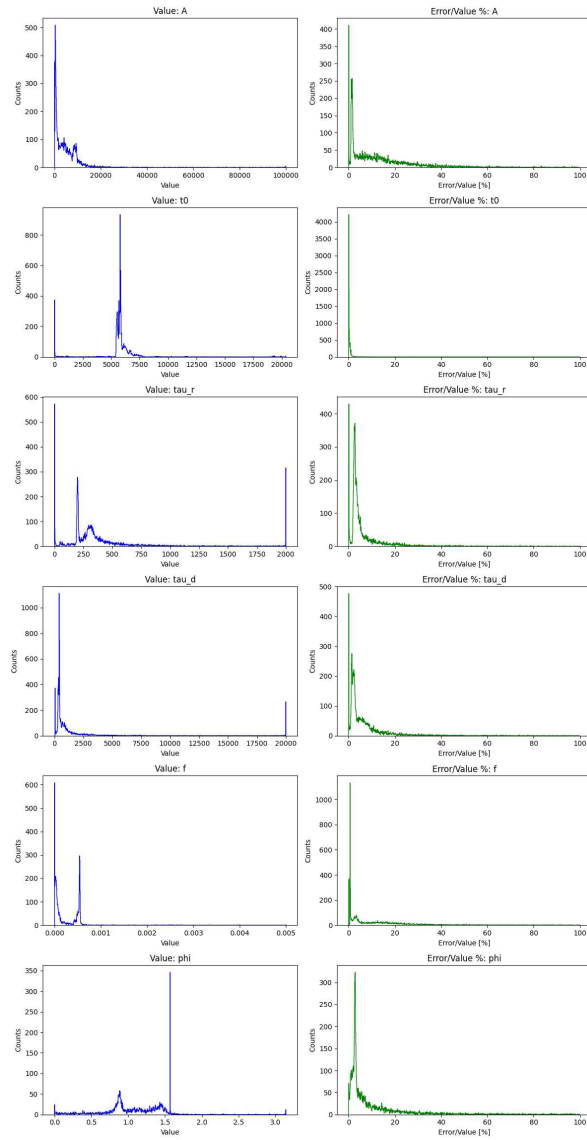


Figure 6.15: On the left the parameters, while on the right their percentage errors.

These plots allow me to visually inspect both the spread of the parameter values and the precision of their estimates: all are well within the expected values.

I analyzed the key waveform characteristics derived from the parametric model. I computed

- **Signal Area:**

$$\text{Area} = \int_{t_0}^{t_{zc}} y(t) dt$$

- **Peaking Time:** time from t_0 to the waveform maximum

$$t_{\text{peak}} = t_{\text{max}} - t_0$$

- **Zero-Crossing Time:** first zero-crossing relative to t_0

$$t_{\text{cross}} = \frac{-\phi + \pi/2}{2\pi f}, \quad t_{\text{cross}} > 0$$

I propagated the parameter uncertainties σ_p using finite differences:

$$\sigma_Q = \sqrt{\sum_i \left(\frac{Q(p_i + \delta p_i) - Q(p_i - \delta p_i)}{2\delta p_i} \sigma_{p_i} \right)^2},$$

where Q represents area, peaking time, or zero-crossing time. I report in figure 6.16 on the left the parameter, while on the right the percentage error.

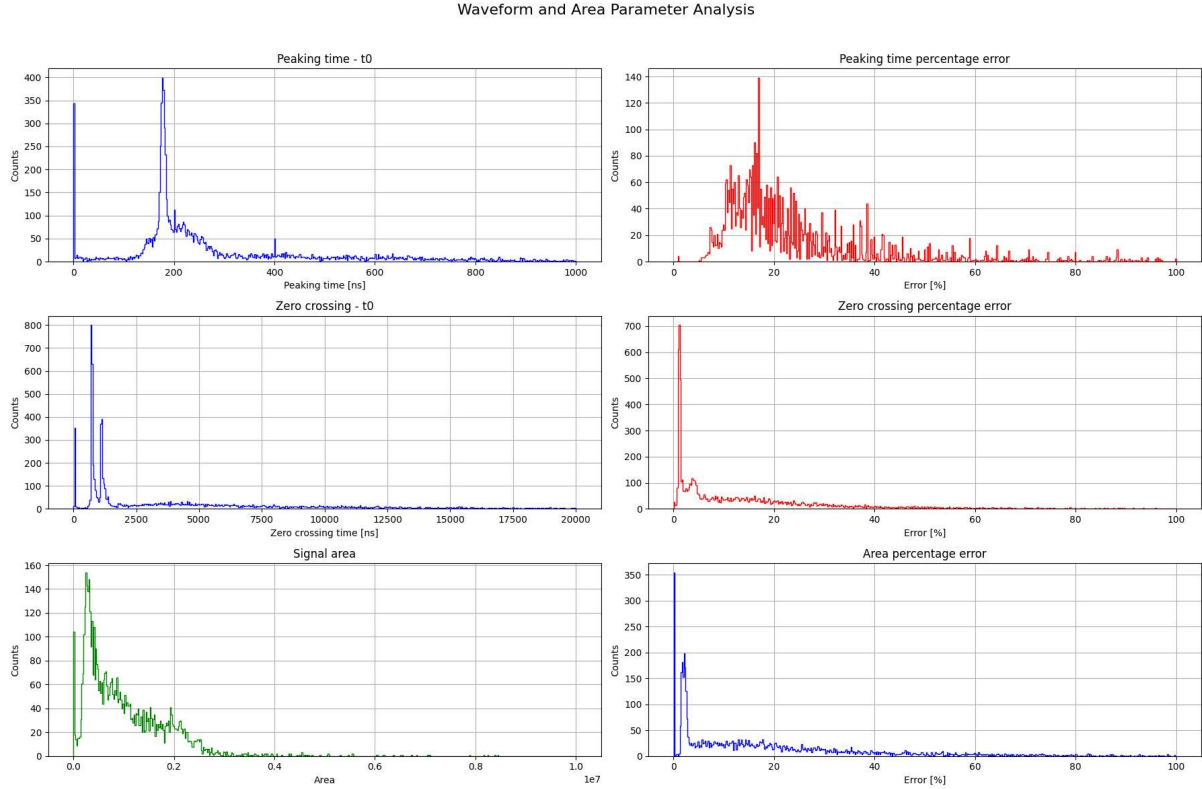


Figure 6.16: On the left the parameters area, peaking time and zero-crossing time, while on the right their percentage errors.

The percentage error for the area is primarily below 20%. Based on the colormaps, I expected to be able to clearly distinguish between different (m, q) parameter sets at this stage of the analysis, and therefore proceeded with the analysis.

6.9 Pad simulation

Having established the normalized area as a viable analysis parameter, the next step was to determine how to extract the specific values of (m, q) . The most direct approach is to use numerical calculations of the area as a function of these parameters. For this purpose, I developed a numerical model for a 3×3 pad system that generates corresponding colormaps as output.

The analysis workflow involves comparing these simulation results with the collected experimental data to identify the specific (m, q) values that best match the observations.

This section explains the mathematical and algorithmic structure of the C++ program. The program performs a 4D parameter scan over (m, q, RC, XRC) . For each parameter combination, it simulates the pad signals generated by a linear charge deposition and calculates, for each of the

3×3 pads, the finite-time area of the pad response up to the first zero-crossing of the convolved signal. Additionally, the program extracts the zero-crossing time and signal amplitude for each pad.

Each simulation call executes the function

`DetectorSimulationParallel(RC_matrix, Gain_matrix, m, q, XRC, tp = 412ns, $\omega = 0\mu\text{m}$)`

which:

1. builds discrete time and space sampling grids, for the time of the waveform and the line of charge, that has units *mm* and *ns*
2. precomputes a temporal response kernel K and a table of time-dependent spreads $\sigma(t)$
3. computes (for each pad and each sample time) the induced charge $Q(t)$ by integrating the deposition along the track using erf expressions
4. convolves $Q(t)$ with the detector kernel K (discrete convolution)

I added the possibility to select the specific RC and gain map. In this way, from the effective values estimated from the ^{55}Fe scan campaign [6], it is possible to improve it and do a simulation "pad per pad".

After filling `conv[k]`, my waveform, the code finds:

- the maximum value $\max_k \text{conv}[k]$ and the time of maximum,
- the first zero-crossing time t^* detected by checking a sign change between consecutive samples:

$$\text{if } \text{conv}[k-1] \cdot \text{conv}[k] < 0 \text{ then } t^* \leftarrow t_k.$$

If no sign change is detected, the fallback sets $t^* = t_{\text{end}} = t_{N_t-1}$.

The finite-time area is computed with a rectangular (Riemann) rule $A \approx \sum_{k=0}^{k^*} \text{conv}[k] \Delta t$, where k^* is the integer index corresponding to t^* . In the code the index is computed as `idx_zero = int($\frac{\text{zero_cross}}{\Delta t}$)` and clamped to the valid range.

The computation across the 9 pads is parallelized with OpenMP:

```
#pragma omp parallel for default(none) shared(...) firstprivate(i_vals, conv, num_points)
for (int idx_pad=0; idx_pad < 9; ++idx_pad) { ... }
```

This allows for a fast processing and optimization, allowing for a smaller scan step.

The `sim()` function builds the parameter grid

$$N_m = 70, \quad N_q = 240, \quad N_{RC} = 15, \quad N_{XRC} = 15$$

and loops over all combinations in the ranges

$$m = [0 : 45^\circ], \quad q = [-12\text{mm} : 12\text{mm}] \quad RC = [50 \frac{\text{ns}}{\text{mm}^2} : 150 \frac{\text{ns}}{\text{mm}^2}] \quad XRC = [1.2 : 6]$$

For each parameter combination, the program calls `DetectorSimulationParallel`, stores the resulting 3×3 matrix of normalized areas in a `Row` structure, and writes all rows to a `ROOT` file. The total number of simulations in this configuration is $N_{\text{total}} = N_m \cdot N_q \cdot N_{RC} \cdot N_{XRC} = 3.78$ million.

Several numerical considerations should be noted:

- **Time offset:** The time vector begins at $t = 0.01$ rather than $t = 0$ to avoid numerical divergences.
- **Quadrature and accuracy:** Spatial integration along the track uses a Riemann sum over s , while temporal convolution is computed by direct summation.
- **Zero-crossing detection:** The zero-crossing time is determined through linear interpolation between consecutive samples where a sign change occurs, providing $\mathcal{O}(\Delta t)$ resolution.
- **Convolution cost:** Direct time-domain convolution scales as $O(N_t^2)$ per pad. For large N_t , FFT-based convolution reduces this to $O(N_t \log N_t)$, but requires the kernel to be causal.

6.10 Reconstruction Algorithm

The next step was to develop a program that connects the simulation results with the experimental data. The analysis was simplified by the fact that all laser events were confined to angles between -45° and $+45^\circ$ relative to the horizontal plane. Additionally, in the horizontal direction (comprising 36 pads), at least one pad was always activated.

The analysis macro processes two ROOT trees:

- A *data* tree containing the fit parameters for each detector pad, organized as a $36 \times 32 \times 6$ matrix derived from the analytical function.
- A *simulation* tree containing precomputed 3×3 pad summaries (area, peak value, zero-crossing times) for a library of simulated events.

For each data event, the analysis macro performs the following steps:

1. Identifies a 3×3 pad neighborhood centered on the pad with maximum charge within each vertical strip (thereby fixing the horizontal coordinate).
2. Computes waveform features (integrated area, maximum amplitude, zero-crossing times) for each pad using the fitted function: $y(t) = \text{scale} \times \text{step}(t - t_0, \tau_r) \times \text{env}(t - t_0, \tau_d) \times \cos(2\pi f(t - t_0) + \phi)$
3. Compares the data from each pad against the entire simulation library using a least-squares minimization method.
4. Records the index of the best-matching simulation for each selected pad in a new ROOT tree.

The candidate pad selection proceeds as follows: for each vertical column i in the 36×32 grid, the program identifies the pad with the highest peak amplitude. This pixel (y, x) becomes a candidate center only if its 3×3 neighborhood lies completely within the detector boundaries (excluding edge pads). The candidate is accepted only if it has a minimum of 3 non-zero neighbors, this serves as a simple clustering filter to reject isolated noise hits.

To compare a data pad with a simulated pad, the macro computes the squared difference:

$$\chi_P^2 = \sum_{i=1}^9 (P_i^{(\text{data})} - P_i^{(\text{sim})})^2,$$

where each term is computed after a *normalization* with the maximum element in the 3×3 system. Concretely, each set (*area, max, zero...*) is normalized by the maximum absolute value

present in that 3×3 block. This is done in general because the units between my data (*ADC* and *ns*) are not the same as my calculation (*Amplitude* and *ns*). The final distance is simply the sum of all the parameter contribution

$$\chi_{\text{total}}^2 = \chi_{\text{area}}^2 + \chi_{\text{max}}^2 + \chi_{\text{zero}}^2 + \dots$$

The simulation index that minimizes this metric is considered the best match for that pad.

After matching, the macro writes an output ROOT file containing a tree of tuples (*event*, *y*, *x*, *best_sim*) for every pad that had a match.

Now the computational complexity is important because this procedure was done to reduce it. Let N_{evt} be the number of data events, N_{sim} the number of simulations, $P = \text{DIM1} \times \text{DIM2}$ the number of pads, and S the number of sample points used to evaluate a waveform and calculate the area of the data. The total asymptotic cost is $\approx O(N_{\text{evt}}(P \cdot S + \text{DIM1} \cdot N_{\text{sim}}))$.

A short pseudo code that summarizes the program is the following

```
load data tree (par, par_err)
load simulation tree (area,max,zero) into memory

for each data event:
  compute per-pixel features by sampling waveform_model:
    area, peak, zero_before, zero_after
  select candidate (y,x) pads using row-wise maxima + neighbor mask
  for each selected pad:
    rotate and flatten pad to 9-element vectors
    for each simulation in bank:
      compute chi2_total = normalized_sqdiff(area)+... (max,zero)
    pick simulation with minimal chi2 and store its index

write best matches into an output ROOT tree
```

while in figure 6.17 I draw a simple flowchart to clarify all the steps.

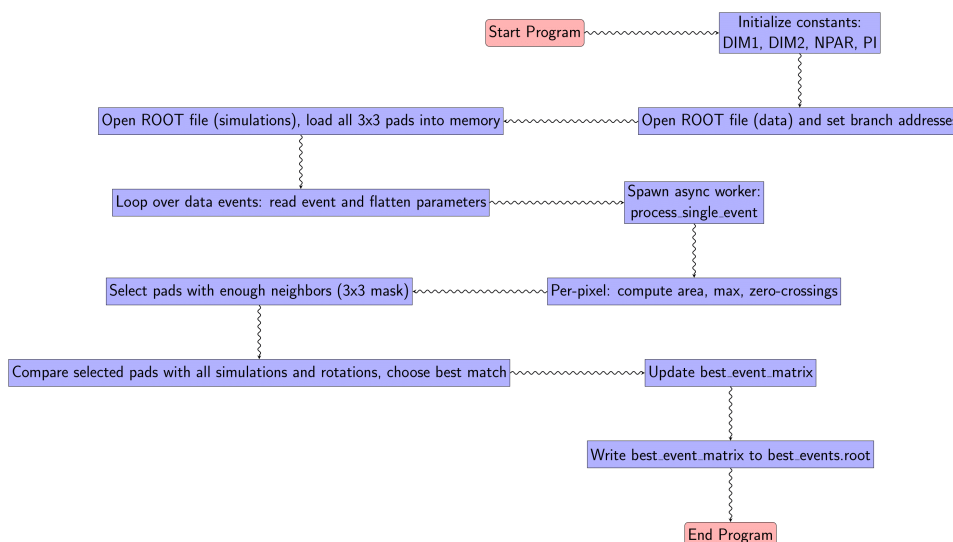


Figure 6.17: Flowchart of my local track reconstruction algorithm.

6.11 Example of fit

At this point I wanted to test my code, and to see the resulting resolution. I tested it in the previous data set with the collimator of $500\mu m$ and still with the α source. This helped me to create the entire work-flow and implement the necessary considerations.

I chose to use a horizontal line such that it simplifies my analysis. In this case, the primary pad is clearly defined as the pad with the highest peak in the waveform. In addition, not all the pads are considered, but I implemented a neighboring filter that eliminates the noise. The code does not perform my analysis on the secondary pads but only on the primary ones; otherwise, I would be reconstructing the track twice.

With my best matches output file I could reconstruct how the tracks looked like and this required some consideration. From the simulation, I generated a straight track long L with a sampling of S , so I had to plot my final line $m \cdot x + q$ as single dots with a distance from each other of $\frac{L}{S}$. These dots would not cover the complete length of L , as it was fixed at $10cm$, a single pad is unable to determine the entire track outside its region. The extended length of L was used to consider also charge spreading in the line direction, and not only in the transverse one.

I then drew my physical points as a merged reconstructed dot like track: in this way I had $dim_1 = 36$ different dot-line segments. This, for example, in my case $L = 10cm, S = 200$ produced $0.5mm/point$, and so each event had $20points \rightarrow 20 \cdot 36 = 720points$ in my ERAM physical plane.

I then proceeded to map the points in their respective positions in my physical ERAM detector plane. I fitted then the ≈ 720 points with a line for each event. The HATPC T2K group defined the resolution as the $RMS = \sqrt{\sigma^2 + \mu^2}$ for a Gaussian fit of the residuals (I decided to maintain free μ instead of fixing it at $\mu = 0$, to observe any bias). So the residuals were calculated for all the events, defined as the distance $y_{fit} - y_{data}$.

In figure 6.18, I provide a clear drawing of how the points are positioned inside the pad and in the ERAM plane, and with the fitted line.

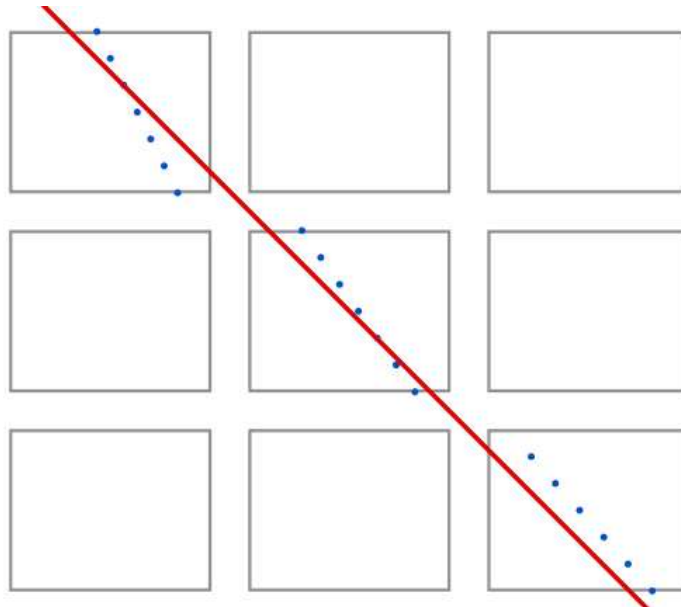


Figure 6.18: A simple drawing (not data) of how the line perform the fit and how the points are positioned in the ERAM plane, starting from different (m_{local}, q_{local}) for each pad. The different points are reconstructed from the values of each pad, while the red line is the fit performed.

A comprehensive flowchart of the event reconstruction is drawn in figure 6.19.

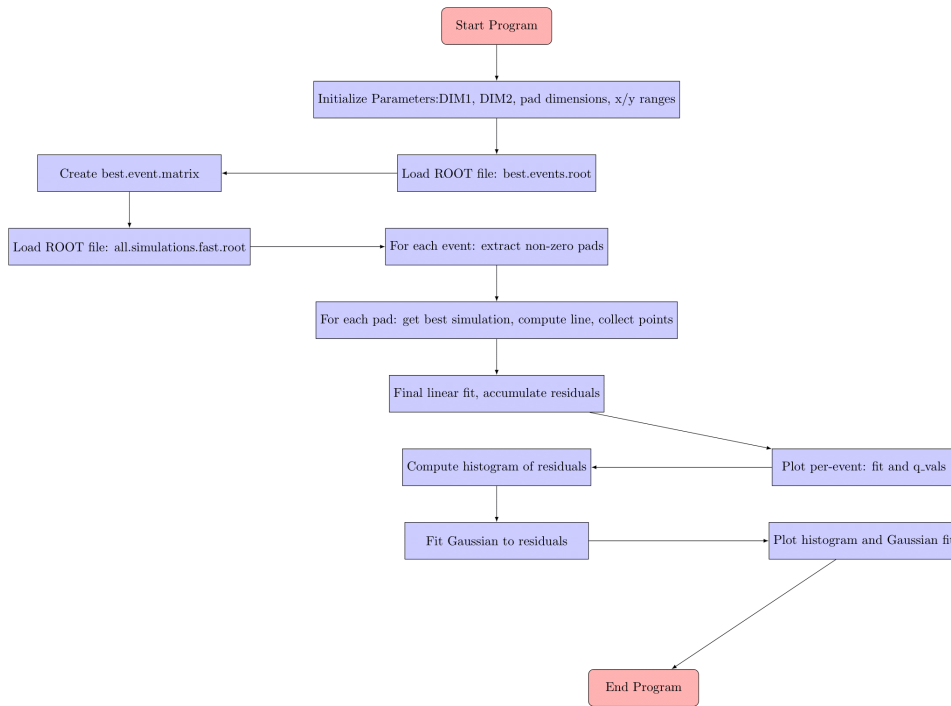


Figure 6.19: Flowchart of my event reconstruction and resolution program.

As shown in figure 6.20, the achieved resolution is approximately $130\mu m$. This represents an improvement by a factor of 3 compared to the expected resolution of $400\text{-}500\mu m$ for the HATPC.

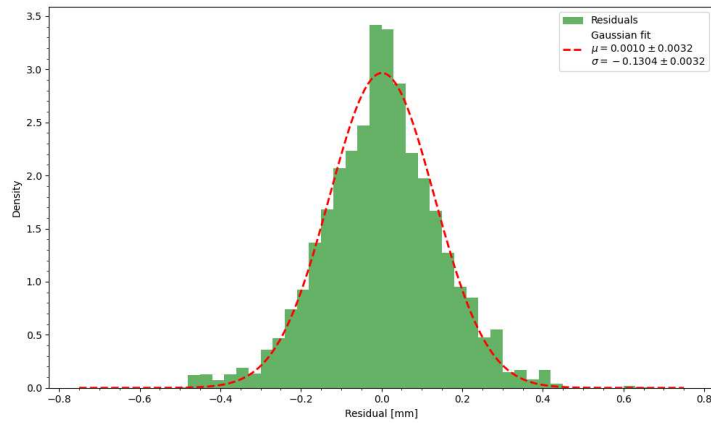


Figure 6.20: Residuals histogram with relative Gaussian fit.

This resolution was calculated using a χ^2 minimization that considered only the normalized area. I tested several alternative configurations, incorporating parameters such as the zero-crossing time, the absolute area, and the maximum amplitude. However, all of these alternatives resulted in a higher σ , particularly within the expected resolution range of $300\text{--}500\mu m$. Consequently, they did not enhance the tracking resolution beyond that achieved by the *LogQ* method used as a benchmark.

6.12 Final considerations about this part of my work

Considering a beam width of $\sigma_{BEAM} \approx 75\mu m$, the initial assumption that the beam width would not affect the resolution is no longer valid. The quadrature sum $\sigma = \sqrt{\sigma_{ERAM}^2 + \sigma_{BEAM}^2}$ yields an intrinsic detector resolution of $\sigma_{ERAM} \approx 100\mu m$, indicating that the laser spot size contributes significantly to the measured resolution.

In summary, this work has achieved the following:

- Improved the tracking algorithm resolution
- Reduced biases from variations in RC and gain values
- Eliminated the clustering procedure, thereby simplifying calculations
- Streamlined the fitting process and established direct connections between physical quantities and waveform signals

Additional tests were performed to validate the workflow. The first test involved collecting data sets using the mirror at various inclination angles to study tracks with different orientations. Theoretically, the resolution should remain constant regardless of the track angle. I initially used the $150\mu m$ collimator with a $3\times$ expander, but the deposited charge was too low for reliable analysis with my program, which requires signals in more than 6 pads over the 3×3 system. This limitation is not expected with muon data, where typically 8 neighboring pads are active.

For the data sets collected at different angles, my reconstruction method shows a higher σ even at zero degrees, similar to previous observations. This confirms that the number of active pads significantly influences the RMS. Nevertheless, I was able to evaluate the relative resolution as a function of angle, as shown in figure 6.21. The results demonstrate a relatively flat angular dependence, which aligns with the expected behavior of my method. In comparison, the LogQ method exhibits a relative resolution change of up to 100% at 45° , while my method remains within approximately 10% variation. The observed fluctuations are likely due to variations in the number of active neighboring pads and their positions.

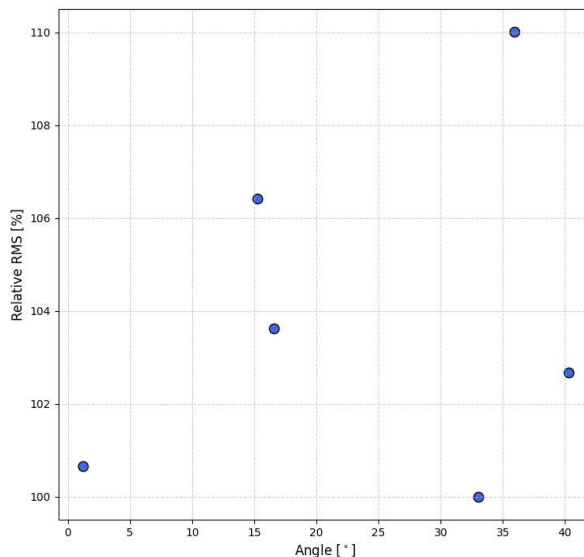


Figure 6.21: Percentage change of the RMS as a function of the angle.

These are only preliminary plots and calculations; further tests are necessary. The initial step is to measure the resolution for different particles and angles, which can be done at a test beam facility. Additionally, the temporal angle should be incorporated into the model. The model must also be tested for more complex scenarios, such as curving particles in a magnetic field.

This concludes the presentation of the proposed analysis framework developed in this work.

Chapter 7

Scintillation light by the T2K gas mixture

The last part of my thesis work involved testing the observation of scintillation light from the TPC gas to be used as a trigger signal. The concept was to install a PMT beneath the ERAM; since light travels instantaneously, its signal could replace the external trigger for the TPC electronics. To date, the T2K gas mixture has not been tested for scintillation properties, as it is unique to the T2K collaboration and was not developed for optically read out TPCs. Furthermore, no literature exists on studies involving the isobutane component in different mixtures. Currently, modeling resistive micromegas is challenging, as their behavior depends strongly on the gas composition. Scintillation light measurements could provide valuable insights and help design appropriate experimental setups to test and refine the models.

7.1 CF_4 scintillation

The scintillation properties of the T2K gas mixture are particularly relevant for minimum ionizing particle (MIP) energy deposits from muons, which are the primary particles detected in ND280. I used cosmic muon tracks to search for time-correlated signals and additionally employed an α source to test for scintillation. The α particles were more likely to produce a detectable signal in the PMT due to their higher energy loss in the medium.

The T2K gas mixture consists of argon, CF_4 , and isobutane. While several studies have investigated the scintillation light of CF_4 in argon mixtures, to my knowledge, no studies exist for mixtures similar to T2K's, particularly those containing a quencher. Quenchers absorb UV photons, thereby reducing avalanches in the MICROMEAS. This is crucial for mitigating high-energy avalanches and improving detector longevity.

The UV and visible emission bands of CF_4 originate from various molecules produced by direct excitation or fragmentation. The visible emission band centered around 630 nm comes from excited CF_3^* , while UV emission between 200 nm and 450 nm is attributed to excited states of the CF_4^+ ion. Recombination effects neutralizing CF_4^+ and CF_3^+ ions can produce additional visible emission from CF_3^* . figure 7.1 shows the spectrum of CF_4 mixtures in argon, where the primary scintillation appears on the left and secondary light on the right. These spectra were experimentally obtained at 1 atm pressure, providing valuable reference for understanding the expected emission characteristics.

An important observation is the strong absorption coefficient I measured for the UV laser at 266 nm. This suggests that the gas may reabsorb scintillation light emitted in the UV range. As previously noted, UV absorption is primarily due to the butane family contaminants, making

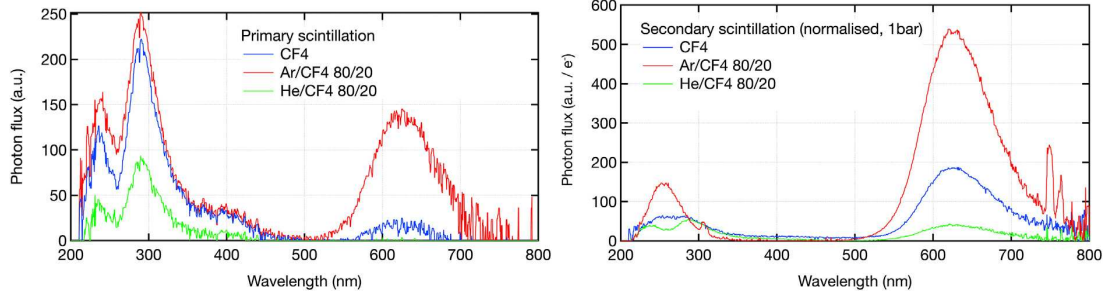


Figure 7.1: Spectrum of CF_4 [9]

it necessary to focus on the visible spectrum where reabsorption might be reduced and the scintillation yield potentially higher.

In fact, CF_4 acts as a wavelength shifter, converting argon’s UV emission into visible light, with the effect depending on its concentration. Increasing the CF_4 proportion enhances the peak around 630 nm. In this visible range, the butane family exhibits lower absorption. The key questions were how much light could be detected and what other factors might limit it.

Ultimately, I expected to observe the peak at approximately 630 nm and use it to trigger the electronics.

It should be noted that for the initial setup, I used the T2K gas mixture with isobutane. In a subsequent setup, I used the same mixture but with n-butane, which is a less effective quencher and might facilitate light detection.

7.2 Experimental setup

The PMT used was a Hamamatsu R7400P-04 HV [19]. The R7400P-04 HV PMT features a compact, small, and robust design with the specifications reported in table 7.1. In figure 7.2 I report the cathode radiant sensitivity as a function of the wavelength, so the parameter κ such that the current and the intensity of light are related via $i = \kappa \cdot I$. As can be seen, the PMT is sensible to the visible spectrum of interest.

| Parameter | Value |
|----------------------------|---------------------|
| Photocathode Type | Bialkali |
| Effective Diameter | 8 mm |
| Number of Dynodes | 10 |
| Operating Voltage | 800 V |
| Gain | $\sim 10^6$ |
| Quantum Efficiency | Up to 25% at 400 nm |
| Dark Current | < 1 nA |
| Transit Time Spread (FWHM) | 300 ps |
| Rise Time | 1.5 ns |
| Spectral Range | 300–650 nm |

Table 7.1: Key characteristics of the R7400P-04 HV PMT.

Two different setups were used, one positioning the PMT in front of the small quartz window and one inserting it inside the chamber. From a practical point of view, the PMT was tested first with the first configuration and later with the second, to check if the fact that I was unable to visualize any coincidence was due to the small angular acceptance. The first part of this

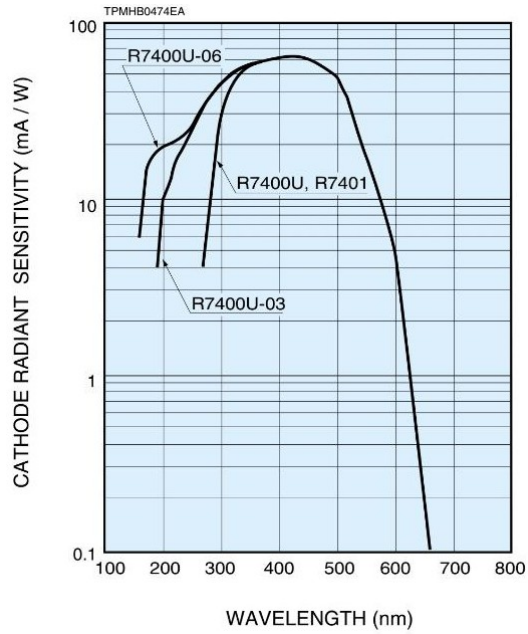


Figure 7.2: Cathode radiant sensitivity as a function of the wavelength.

activity was performed before the internal modifications to the chamber, as explained in section *Final configuration and data taking*, and so still with the α source present.



Figure 7.3: The PMT.

For the analysis of the time correlation the filtering with the skewed Gaussian was not performed as I was mainly interested in reconstructing possible tracks of the α particles (as will be discussed, no muons were observed for the first setup). I was not at first interested in high-precision measurements. A parabolic fit was the optimal one to determine the peak position in time.

The first part was to check if the scintillation light was visible with the PMT attached to the quartz window. To do so, a trigger was created using a discriminator and a NIM module with the PMT signal, and a data set was acquired. The gas flow was set at around $10L/h$, the DLC voltage at $340V$ with a current of $173nA$ and the cathode voltage at $5kV$.

7.3 Analysis of the Quartz Window Data Set

I expected the α source to produce the majority of the light, given its proximity to the quartz window and its high energy deposition. This is particularly valuable because most radioactive sources do not provide time-correlated signals that can be used as triggers. Such a trigger could be useful for calibration studies. Although cosmic muons could also produce light, no muon-like events were observed in the data, as these would be distinguishable in the event plots. Therefore, the analysis focused exclusively on α particles.

Figure 7.4 shows a 3D plot of all events in the data set. A noise plane is visible at approximately 4000 ns (100 bins), where the PMT registers background triggers.

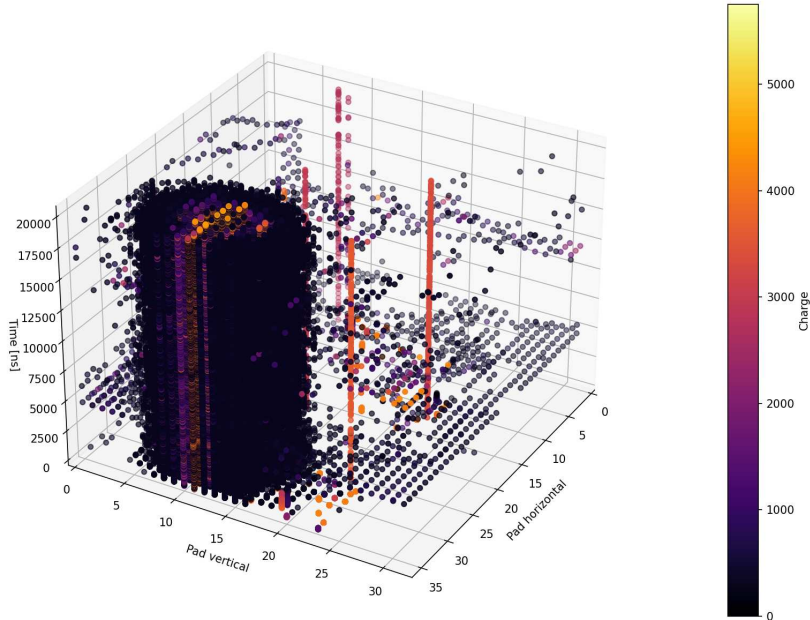


Figure 7.4: Complete data set plot in 3D.

I first analyzed the histogram of the time of maximum signal for all pads. If a time correlation existed due to the α particle, the signal should appear primarily between 100 and 200 bins, corresponding to the TPC's sensitive time window. Although a random background component was expected, I initially assumed it would be small. As shown in figure 7.5, no clear signal matching the expected pattern was observed; however, a peak appeared around bin 100. This position corresponds to the anode time set by the electronics, suggesting that detectable light emission occurs primarily during the avalanche process, where photon production is enhanced.

I fitted the time histogram with a Gaussian function plus a constant background: $f(x) = A \exp\left(-\frac{(x-\mu)^2}{2\sigma^2}\right) + C$. The results, presented in table 7.2, show that the peak amplitude is significantly above background fluctuations, with a signal-to-background ratio of $\frac{A}{C} \approx 4.8$.

To test the hypothesis that the observed signal was scintillation light from electron avalanches, I analyzed the 2D charge-time histogram. If the time correlation originated from avalanches,

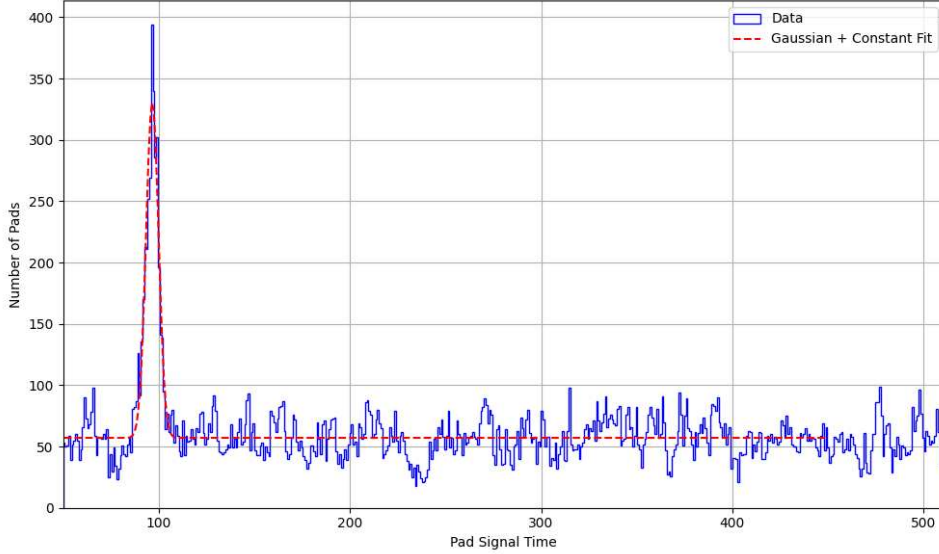


Figure 7.5: Time histogram of the α data set.

| Parameter | Value |
|-----------|----------------------|
| A | 273.7 ± 7.7 |
| μ | $(96.7 \pm 0.1)bins$ |
| σ | $(3.3 \pm 0.1)bins$ |
| C | 57.1 ± 0.8 |

Table 7.2: Fit results.

then higher charge signals should correlate with higher PMT detection probability. As shown in figure 7.6, a distinct peak is visible in this distribution. This provides strong evidence that the PMT was detecting genuine time-correlated signals above background noise, likely triggered by the high-energy deposition of α tracks which produce more extensive avalanches compared to muons.

7.4 α tracking

The main question arising from this analysis was whether the time information could be used for α particle tracking. Before proceeding, it is important to consider several potential challenges:

- The high charge of α particles could distort tracks through self-interaction effects
- The short track length in the ERAM plane might require excluding many data sets, particularly tracks perpendicular to the ERAM that can't be reconstructed
- Tracks should only appear after the trigger, with the highest charge deposition occurring at the Bragg peak, which is furthest from the source (and thus closer to the anode)

For pattern recognition, I employed the HDBSCAN (Hierarchical Density-Based Spatial Clustering of Applications with Noise) algorithm from the scikit-learn Python toolkit. This machine learning approach groups data points into clusters based on relative distances and minimum cluster size requirements. HDBSCAN is particularly effective for identifying irregular structures with variable density, automatically determining the number of clusters while labeling

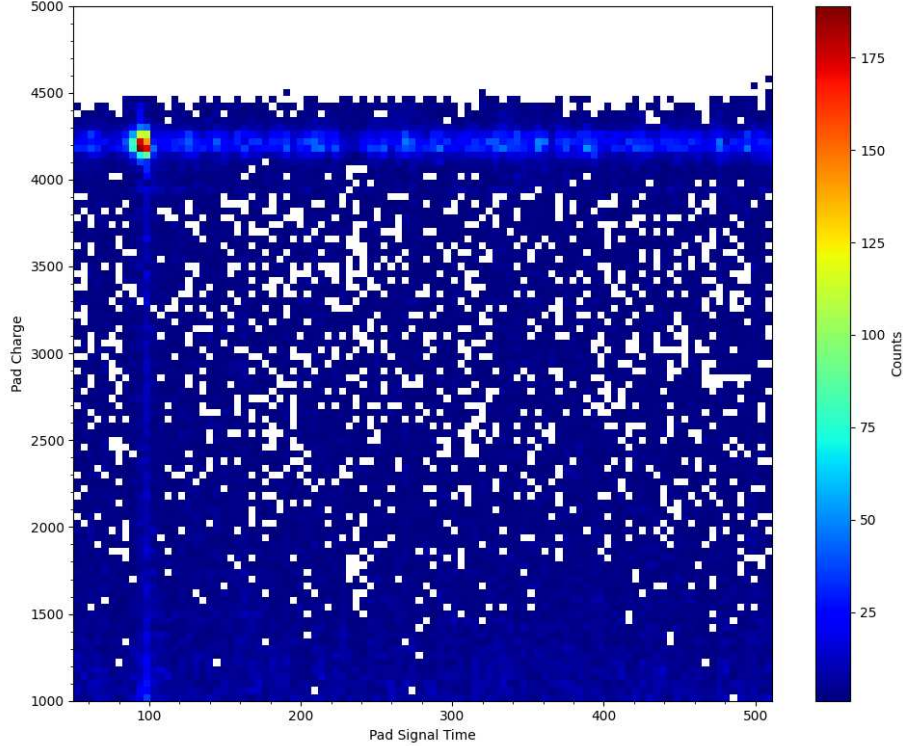


Figure 7.6: 2D histogram of the charge ($[ADC]$) and the time ($[bin]$).

noise points. The clustering was performed in a 3D space comprising pad coordinates and signal peaking time.

To verify that the identified clusters represented physical particle tracks, each cluster was validated against the following criteria:

- **Time Window:** At least one hit in the cluster must have fallen within a predefined signal time window (85 to 105 units).
- **Shape and Elongation:** Principal Component Analysis (PCA) was applied in the ERAM plane to measure the aspect ratio and length of the cluster.
- **Connectivity:** A custom 2D connectivity check ensured that all pads in the cluster formed a single connected component.

Clusters that failed to meet these criteria were classified as noise and excluded; in total, only $\frac{17}{6106} \approx 0.27\%$ events were considered valid. One point of limitation in the signal to noise ratio, is that I was not limiting the noise from the very source. Specifically, this is what a possible next experimental setup should have, as shown in figure 7.7:

- **Frontal block:** from the DLC power supply I was able to measure the current produced by the α source. So the main source of noise is the center of the source, in the cathode plane. By positioning a small metal disk, with 3/4 legs, the source can be covered to the anode, but α particles could escape laterally, reducing the noise from the DLC current and eliminating the perpendicular events.
- **Double PMT:** near the α source, it would be interesting to position two PMTs to check the trigger coincidence, looking toward the anode mesh.

- **Movements system:** a movement system in the gas chamber could move the α and the two PMTs in a way that could be used to map the ERAM resistivity and gain, similarly to what was done with the ^{55}Fe source.

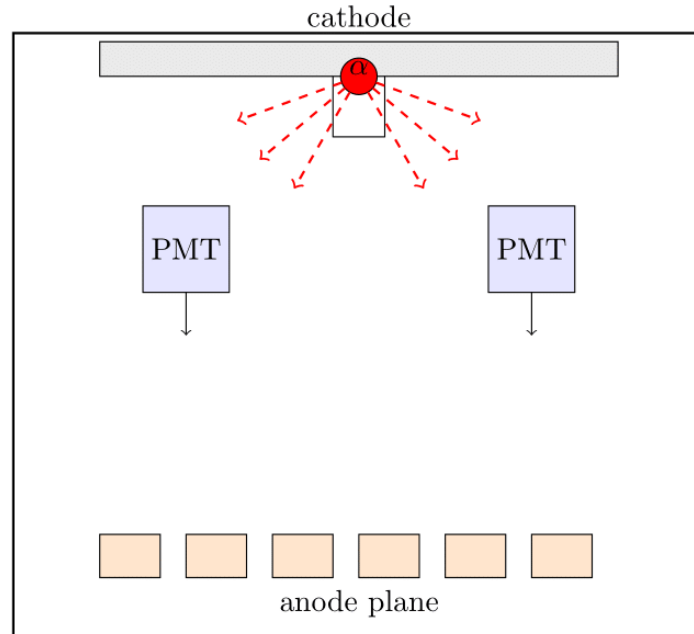


Figure 7.7: Example of a possible α testing setup, some α can escape laterally and be visualized from the anode detector.

The inability to detect scintillation light from cosmic ray primary ionization could be attributed to several factors, which motivated the development of a more efficient configuration:

- The limited angular acceptance of the light collection aperture
- Potential inefficiencies in the PMT coupling, despite the quartz window's transparency in the relevant wavelength range
- The intrinsically low light yield of the gas mixture for minimum ionizing particles like muons, which may be below the detection threshold

7.5 Monte Carlo Simulation of Muon Tracks and Photon Detection

Before installing the PMT in the chamber, I performed calculations to estimate the expected signal, knowing I observed scintillation from high-energy α -induced avalanches.

To evaluate the photon collection efficiency, I developed a simple Monte Carlo simulation of muon trajectories through a 3D volume. In this model, each muon generates light emission along its path, with photons undergoing exponential attenuation. Detection occurs only when photons pass through a small circular aperture and reach the sensitive area of the detector.

The simulation volume is a box with dimensions $25\text{ cm} \times 50\text{ cm} \times 50\text{ cm}$. A cylindrical detector of radius 0.4 cm is positioned outside one wall, simulating the initial side-mounted PMT configuration. The following parameters were defined (focusing primarily on angular acceptance):

- Light yield per unit track length: LIGHT_YIELD = 4000 photons/cm
- Photon attenuation coefficient: $\alpha = 0.1 \text{ cm}^{-1}$

Each simulated muon track originates at a random position on the top surface and propagates in a randomly sampled direction. The direction vector \vec{v} is constructed by sampling the polar angle θ and azimuthal angle ϕ , with the unit vector expressed as:

$$\vec{v} = \begin{bmatrix} \sin \theta \cos \phi \\ \sin \theta \sin \phi \\ -\cos \theta \end{bmatrix}$$

Each muon track was propagated through the box until it exited. At each step along the muon path, the code evaluated whether the photons produced at that location could reach the detector:

- The vector from the emission point to the detector $\vec{r}_{\text{detector}} - \vec{r}_{\text{emission}}$ was computed.
- This vector was checked to see if it intersected the hole and aligned with the detector's facing normal.
- If both conditions were met, the number of photons arriving at the detector was calculated using the exponential attenuation law:

$$N_{\gamma} = N_0 \exp(-\alpha d)$$

where d is the distance to the detector, multiplied by a random uniform distribution in 3D.

In figure 7.8 I draw an example of what the code does in the simulation.

To study the effect of hole size on photon collection, the simulation was repeated for multiple hole radii. For each radius, the total number of detected photons was recorded. A sample result is plotted in figure 7.9. The ratio between the case with $D_{\text{hole}} = 2\text{mm}$ and the maximum $D_{\text{hole}} = 50\text{mm}$ is ≈ 170 . So I can assert that the hole dimension limit the efficiency by that factor

To calculate the number of photons emitted in the avalanche of an α particle with an amplification gain of 1000 in the mesh, I assumed a light yield per avalanche electron of $\sim 0.05 - 0.1 \text{ photons/electron}$ for the T2K gas.

Then I estimates for an α event

$$\begin{aligned} N_{\text{primary electrons}} &= \frac{E_{\alpha}}{W} = \frac{5.5 \times 10^6 \text{ eV}}{26 \text{ eV}} \approx 2.12 \times 10^5 \text{ electrons} \\ N_{\text{avalanche electrons}} &= N_{\text{primary}} \times G = 2.12 \times 10^5 \times 1000 = 2.12 \times 10^8 \\ N_{\text{photons}} &= 0.05 \times 2.12 \times 10^8 \approx \boxed{1.06 \times 10^7 \text{ photons}} \end{aligned}$$

Then I wanted to estimate the light emission for a single muon and α particle, with an approximate light yield of 2000 photons/MeV (from gas mixtures without isobutane [9])

- α s deposited all its energy in a very short range so I assumed $L_{\alpha} = 2000 \text{ ph/MeV} \times 5.5 \text{ MeV} = \boxed{11,000 \text{ photons}}$
- muons in T2K gas lose energy around $\left(\frac{dE}{dx}\right)_{\mu} \approx 2 \text{ MeV/cm}$, over 50cm then $E_{\mu} = 2 \times 50 = 100 \text{ MeV}$ and so $L_{\mu} = 2000 \text{ ph/MeV} \times 100 \text{ MeV} = \boxed{200,000 \text{ photons}}$

Now it is clear that if I inserts the PMT in the gas the efficiency would increase by $\approx 173\times$, and if every event $\approx 3.46 \cdot 10^7$ photons are emitted I would reach the already observed limit of 1.06×10^7 photons. Then it seemed logical to proceed to insert the PMT inside the chamber.

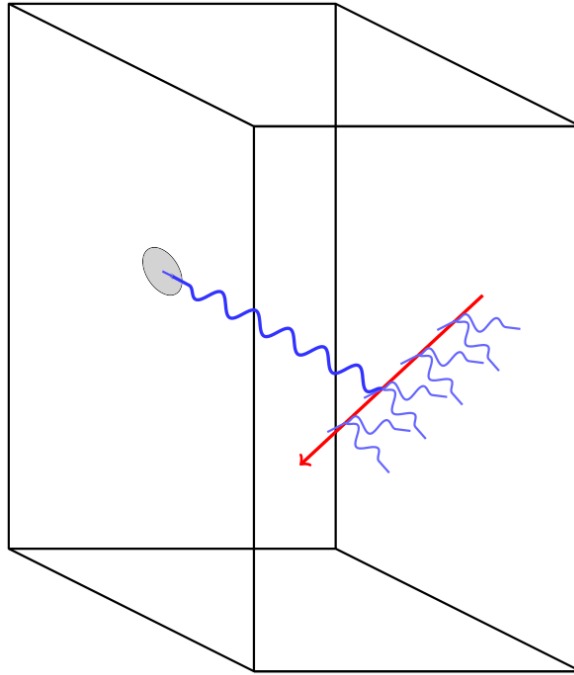


Figure 7.8: A plot to show how the simulation works, for each point a certain number of photons are produced, then only the ones entering the detector are selected.

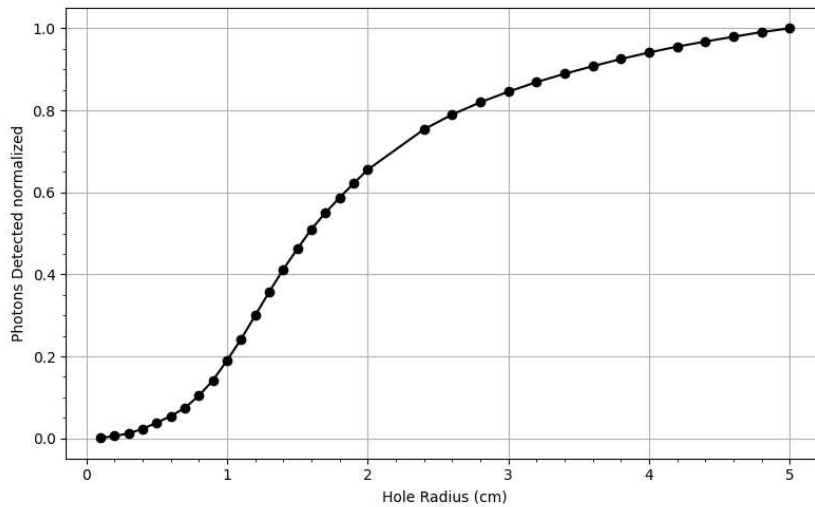


Figure 7.9: Photons detected normalized to the value at $D_{hole} = 50mm$.

7.6 PMT Installation into the Active Volume

To install the PMT, a flange located beneath the ERAM detector was removed, it was drilled a hole in it, and used an O-ring to secure the PMT while maintaining gas containment. The high-voltage and signal cables passed through the flange, requiring additional sealing paste alongside the O-ring. However, when operating at the nominal voltage of 800 V, I heard metallic discharge noises. This occurred because argon gas infiltrated the interface between the voltage divider pins and the photocathode connections, where the 1-2 mm pin spacing allowed discharges to form.

This issue necessitated a redesign of the setup.

I modified the flange by attaching a glass cylinder to its interior-facing side and sealing the open end with a magnesium fluoride lens. This configuration allowed the PMT to be housed in air while maintaining gas containment in the chamber. The modified flange design is shown in figure 7.10. The PMT can be inserted into the glass cylinder from outside the chamber, effectively positioning it within the chamber volume while remaining in atmospheric conditions.



Figure 7.10: Modified flange.

The problem now arising was the fact that the PMT HV dynode can be in contact with a dielectric material (the lens), which can cause some discharge effects. Some tests have been conducted first in air and then in pure argon. Also, I did not know in advance the effect of the electric field produced by the TPC to the PMT. I checked if everything was working properly first by testing the PMT with the chamber filled with air and with the HV on; no problem was present. Then I filled it with argon and redid the whole process, still finding no problem. I did not position the PMT directly in contact with the lens to avoid possible discharges, and also because it would be an unnecessary risk. I noticed, using an oscilloscope, that increasing the cathode HV the PMT signals were statistically increasing. This is because the electric field between the anode and cathode of the PMT was increasing, due to the TPC additive term.

By inserting the PMT in the chamber, I should have been able to visualize the tracks twice, one due to the primary scintillation and the second when the charge arrived to the MICROMEAS. In the second case the TPC should be in busy mode, as I already have the previous trigger. In addition, I will be able to register the events from the other side of the chamber, because the cathode is transparent. I will be able to detect the events but not to observe it in the ERAM, this introduces a minimum signal-to-noise ratio of 1/2.

During these operations, the TPC was completely covered to prevent external light from entering the chamber. Crucially, by also covering the G10 components that were not already shielded by the aluminum layer, I significantly reduced the electronic noise.

7.7 Analysis of Data with the PMT facing the Active Volume

First, I plotted all the events in the data set. However, with the PMT installed in the flange configuration, no time correlation was observed.

To investigate this lack of signal, I positioned the PMT to directly view the large quartz window, expecting to detect scintillation light from electron avalanches as previously. Despite this adjustment, no time correlation was observed. This could be due to the lower signal intensity compared to α particles or insufficient gas purity.

I then increased the DLC voltage, reasoning that larger avalanches might produce sufficient light for triggering. However, no scintillation light was detected even at 400V. Higher voltages were avoided to prevent potential sparking.

Finally, I attempted to improve gas purity, as scintillation may require oxygen and water contamination below certain ppm levels. The chamber was flushed with approximately five additional gas volumes at maximum flow rate.

I proceeded to use a plastic scintillator. The plastic scintillator, readout by a PMT, was positioned under the ERAM and I collected a data set. As it was clear I was able to see cosmic muons. From this I understood that the trigger electronics was working and there was no delay that could cause the missing coincidence. I used an oscilloscope with the input signals from the small PMT in the chamber and the plastic scintillator, to visualize the two in-coincidence signals. But that was not the case, as triggering on the second one I had no signal from the first.

I collected a data set of one hour using the small PMT, only few events are present, while the expected number is $\approx 75k$. In figure 7.11 I report all the events for the dataset with the scintillator (for 30 seconds data taking) and with the PMT.

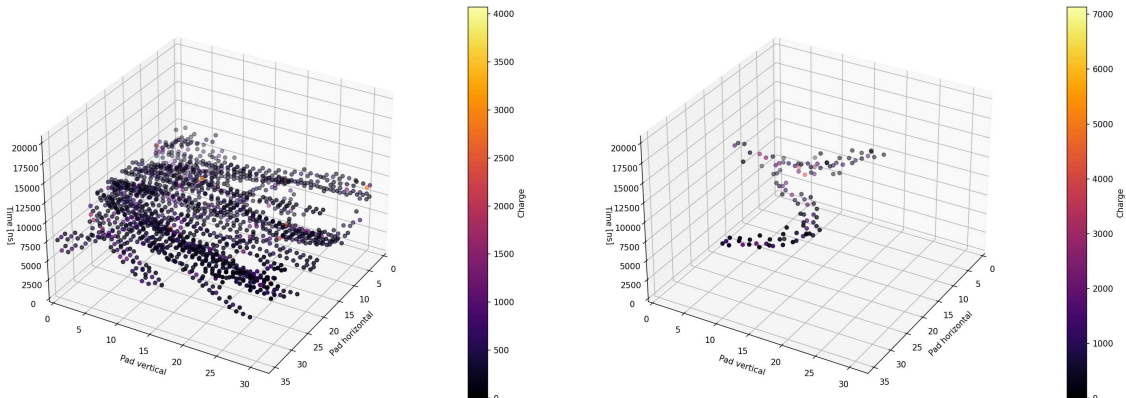


Figure 7.11: All the events with the scintillator positioned on the bottom on the left, while with the PMT in the flange on the right.

In summary, the PMT was unable to detect primary scintillation light from muons. This could still be due to the limited angular acceptance, but the flange size restricted the use of a larger PMT, which would also be incompatible with systems like FC0. Additionally, as a single-photon detector, the PMT did not register even one photon per event in most cases. Scintillation light was only usable for triggering in the case of α -induced avalanches, and even then, the signal-to-noise ratio was lower than anticipated. The higher efficiency of this method, for cosmic muons detection, was the original motivation for this analysis.

My theory for the absence of scintillation light is that n-butane absorbs the UV photons emitted by argon before CF_4 can wavelength-shift them. The number of detectable photons can

be modeled as:

$$N = \text{LightYield} \cdot \frac{dE}{dx} \cdot \text{Length} \cdot e^{-\alpha_{\text{butane}} \cdot d} \cdot P_{\text{shifting}}(d)$$

where α_{butane} is the absorption coefficient of butane and $P_{\text{shifting}}(d)$ is the probability of CF_4 shifting the wavelength over distance d . In this setup, there is a competition between absorption by butane and shifting by CF_4 , which drastically reduces the photon count, resulting in $N \approx 0$. I expect this model that the product $e^{-\alpha_{\text{butane}} \cdot d} \cdot P_{\text{shifting}}(d)$ approaches zero over distances of a few millimeters.

Conclusions

Following an introduction to neutrino physics and the HATPC detector in ND280, this thesis work focused on several key developments.

First, I established a functional laser calibration system using a TPC prototype, analyzing its operation and addressing issues such as beam spot size and divergence. I then implemented a basic tracking algorithm to validate the setup and assess its suitability for resolution studies.

I subsequently modified and tested new components for future data-taking campaigns. These modifications revealed various challenges, including mirror-induced deformations and enhanced crosstalk effects, demonstrating the laser's utility for precise cross-talk characterization.

Building on physical first principles, I developed a new track reconstruction algorithm. The development process involved testing complete waveform convolution and identifying robust observables. Using the most promising parameter—the normalized area—I created a computational simulation to compare expected and measured values. Testing on experimental data showed improved resolution compared to the current HATPC tracking method, providing a foundation for future algorithm development.

Finally, using the prototype, I demonstrated the detection of scintillation light from α -induced avalanches, but with a low signal-to-noise ratio. Attempts to observe cosmic muon scintillation were unsuccessful, likely because the quencher absorption length is shorter than the characteristic distance for CF_4 wavelength shifting.

Bibliography

- [1] N. Abgrall et al., *Time projection chambers for the T2K near detectors*, Nucl. Instrum. Meth. A 637, 25–46 (2011), <https://www.sciencedirect.com/science/article/pii/S0168900211003421>.
- [2] K. Abe et al., *The T2K experiment*, Nucl. Instrum. Meth. A 659, 106–135 (2011), <https://www.sciencedirect.com/science/article/pii/S0168900211011910>.
- [3] K. Abe et al., *T2K ND280 Upgrade – Technical Design Report*, 2020, <https://arxiv.org/abs/1901.03750>.
- [4] B. Abi et al., *Deep Underground Neutrino Experiment (DUNE), Far Detector Technical Design Report, Volume I: Introduction to DUNE*, 2020, <https://arxiv.org/abs/2002.02967>.
- [5] M. Aker et al., *KATRIN: status and prospects for the neutrino mass and beyond*, J. Phys. G: Nucl. Part. Phys. 49, 100501 (2022), <http://dx.doi.org/10.1088/1361-6471/ac834e>.
- [6] L. Ambrosi et al., *Characterization of charge spreading and gain of encapsulated resistive Micromegas detectors for the upgrade of the T2K Near Detector Time Projection Chambers*, Nucl. Instrum. Meth. A 1056, 168534 (2023), <https://doi.org/10.1016/j.nima.2023.168534>.
- [7] D. Attiè et al., *Analysis of test beam data taken with a prototype of TPC with resistive Micromegas for the T2K Near Detector upgrade*, Nucl. Instrum. Meth. A (2023), Preprint submitted May 17, 2023.
- [8] S. F. Biagi, *Magboltz 11*, <http://magboltz.web.cern.ch/magboltz/>.
- [9] F. M. Brunbauer et al., *Primary and secondary scintillation of CF₄-based mixtures in low-pressure gaseous detectors*, Front. Detector Sci. Technol. 3, 1561739 (2025), <https://doi.org/10.3389/fdest.2025.1561739>.
- [10] Y. Cai et al., *Investigation of UV laser ionisation in argon-based gas mixtures with a triple-GEM detector*, J. Instrum. 15(02) T02001 (2020), <https://doi.org/10.1088/1748-0221/15/02/T02001>.
- [11] CAEN S.p.A., *N93B – Dual Timer*, 2025, <https://www.caen.it/products/n93b/>.
- [12] CAEN S.p.A., *CAEN N96 Leading Edge Discriminator Manual*, 2006, <https://wwwusers.ts.infn.it/~rui/univ/AcquisizioneDati/Manuals/CAEN%20N96.pdf>.
- [13] Edmund Optics Inc., *Edmund Optics Technical Resource Guide*, 2023, <https://www.edmundoptics.com/resources/>.

- [14] S. Fukuda et al., *The Super-Kamiokande detector*, Nucl. Instrum. Meth. A 501, 418–462 (2003), <https://www.sciencedirect.com/science/article/pii/S016890020300425X>.
- [15] C. Forza, *Characterization and commissioning of two large volume gaseous Time Projection Chambers at CERN and JPARC laboratories*, Master’s thesis, Università degli Studi di Padova, 2024.
- [16] M. C. Gonzalez-Garcia and M. Yokoyama, *Neutrino Masses, Mixing, and Oscillations*, Phys. Rev. D 110, 030001 (2024), Particle Data Group, <https://pdg.lbl.gov/2024/reviews/rpp2024-rev-neutrino-mixing.pdf>.
- [17] H. Schindler, *Garfield++: Simulation of Tracking Detectors*, 2023, <https://garfieldpp.web.cern.ch/>.
- [18] CERN, *Garfield++: Simulation of Gaseous Detectors*, 2025, <https://garfieldpp.web.cern.ch/garfieldpp/>.
- [19] Hamamatsu Photonics K.K., *Photomultiplier Tubes and Assemblies — Handbook / Technical Datasheet*, 2020, https://www.hamamatsu.com/content/dam/hamamatsu-photonics/sites/documents/99_SALES_LIBRARY/etd/PMT_handbook_v4E.pdf.
- [20] H. J. Hilke, *Detector Calibration With Lasers - a Review*, Nucl. Instrum. Meth. A 252, 169–179 (1986), [https://doi.org/10.1016/0168-9002\(86\)91088-0](https://doi.org/10.1016/0168-9002(86)91088-0).
- [21] B. J. P. Jones, *The Physics of Neutrinoless Double Beta Decay: A Primer*, 2022, <https://arxiv.org/abs/2108.09364>.
- [22] LeCroy Corporation, *Model 688AL Level Adapter: 8 Channel NIM-to-TTL and TTL-to-NIM Conversion*, 2025, <https://mobydick.mib.infn.it/brofferio/didattica/datasheet/LeCroy%20688.pdf>.
- [23] F. van Goor et al., *LightPipes for Python: Optical Toolbox Documentation*, Delft University of Technology, 2023, <https://opticspy.github.io/lightpipes/>.
- [24] D. Marchesini, G. Brambilla, *ADVANCED-LABORATORY*, 2024, <https://github.com/DaiveMarchesini/ADVANCED-LABORATORY>.
- [25] Photonics Solutions, *Minilite Nd:YAG Laser: Online Datasheet*, <https://www.photonicsolutions.co.uk/upfiles/DatasheetforMiniliteIandIILG07Dec17.pdf>.
- [26] Super-Kamiokande Collaboration (Y. Fukuda et al.), *Evidence for Oscillation of Atmospheric Neutrinos*, Phys. Rev. Lett. 81, 1562–1567 (1998), <https://link.aps.org/doi/10.1103/PhysRevLett.81.1562>.
- [27] T. Radermacher, *Measurements and Simulation of Drift Gas Properties for the Time Projection Chambers of the T2K Experiment and for Future Neutrino Experiments*, Ph.D. dissertation, RWTH Aachen University (2019).
- [28] L. Scomparin, *Signal Formation in the new Time Projection Chambers of the T2K Upgraded Experiment*, Master’s thesis, Università degli Studi di Padova (2022), https://thesis.unipd.it/retrieve/81e65a33-b1d2-4f8e-8b72-e0488b5ecbcc/Tesi_Scomparin_Luca.pdf.

- [29] Y. Takeuchi, *Recent results and future prospects of Super-Kamiokande*, Nucl. Instrum. Meth. A 952, 161634 (2020), 10th International Workshop on Ring Imaging Cherenkov Detectors (RICH 2018), <https://www.sciencedirect.com/science/article/pii/S0168900218317200>.
- [30] U. Virginet et al., *The ERAM technology: The logQ method*, Poster, T2K / neutrino instrumentation workshop (2024), https://agenda.infn.it/event/37867/contributions/228223/attachments/121084/176471/PosterNeutrino2024_UlysseVirginet_ID247.pdf.
- [31] Wolfram Demonstrations Project, *Neutrino Oscillations*, Accessed 2025, <https://demonstrations.wolfram.com/NeutrinoOscillations/>.
- [32] K. Abe et al., *Constraint on the matter–antimatter symmetry-violating phase in neutrino oscillations*, Nature 580, 339–344 (2020), <http://dx.doi.org/10.1038/s41586-020-2177-0>.
- [33] *Constraint on neutrino properties*, Prog. Part. Nucl. Phys. 123, 103927 (2022), <http://dx.doi.org/10.1016/j.pnpnp.2021.103927>.
- [34] A. Longhin and F. Terranova, *Enhanced NeUtrino BEams from kaon Tagging (ENUBET)*, 2022, <https://arxiv.org/abs/2203.08319>.
- [35] KNF Neuberger, *Operating Manual: Diaphragm Gas Pump N 938*, 2025, <https://knf.com/en/us/solutions/pumps/series/diaphragm-gas-pump-n-938>.
- [36] O. M. Company, *HVC Series - High Voltage Resistors*, 2025, <https://www.ohmite.com/hvc-series/>.